Biopolymer Nanostructures at interfaces:

Influence of Physicochemical Surface Properties on IAPP Adsorption, Aggregation, and Fibrillization

Dissertation

Zur Erlangung des akademischen Grades eines Doktors der Naturwissenschaften

(Dr. rer. nat.) der Fakultät für Naturwissenschaften der Universität Paderborn

vorgelegt von Roozbeh Hajiraissi (M.Sc.)

aus dem Iran

1. **Examiner 1: Dr. Adrian Keller**
2. **Examiner 2: Professor Yixin Zhang**
3. **Examiner 3: Professor Guido Grundmeier**

Oral examination date: 12.09 (September).2018

Abstract

Misfolding and subsequent assembly of proteins and peptides into insoluble amyloid structures play important roles in the development of numerous diseases. The dynamics of self-assembly and the morphology of the resulting aggregates critically depend on various environmental factors and especially on the presence of interfaces. Here, we show in detail how the presence of surfaces with different physicochemical properties influences the assembly dynamics and adsorptions of human islet amyloid polypeptide (hIAPP) which is involved in development of type 2 diabetes mellitus (T2DM). The surfaces used in this work can be categorized into two groups: inorganic (mica as hydrophilic substrate and hydrophobic hydrocarbon-coated mica) and self-assembled monolayers with molecularly defined functional groups (hydrophobic, hydrophilic, negative, and positive charge SAMs). Time-lapse atomic force microscopy (AFM) is employed to study the morphology of the resulting aggregates in bulk solution as well as at various molecularly defined surfaces ex-situ. Dynamics of IAPP adsorption at various SAMs is studied in situ using quartz crystal microbalance with dissipation monitoring (QCM-D). Native hIAPP(20-29) as the core region of amyloid fibrillization, native hIAPP(1-37), and hIAPP(20-29) with modified termini (acetylated and amidated) were employed to analyze the influence of the physicochemical surface properties on aggregation and self-assembly at various surfaces. After incubation of the native IAPP(20-29) on mica surface it was found that fibrillar self-assembly promoted and three fibrillar species (straight, coiled and ribbon-like) were formed on the mica, whereas in test tube only straight and coiled fibrils with different dimensions were observed. After incubation on hydrophobic hydrocarbon surfaces it was observed that fibrillization was retarded. Fibrillization of hIAPP(1-37) as full-length

peptide was evaluated on SAMs and it was observed that upon exposure to negatively charged SAM, the fibrillization expedited and a three-dimensional network of interwoven fibrils were formed. When a CH_3-terminated SAM was employed, hydrophobic interactions at the interface tended to retard the fibrillization. By using OH- and NH_2-terminated SAMs, it was assumed that the fibrillization is governed by hydrogen bonding. After injection of terminally modified IAPP(20-29) onto various SAMs, the peptides showed varying extents of polymorphisms. By terminal modifications of the hIAPP(20-29), the peptide became neutral, positive and negative. On the contrary to full length IAPP, the fragments formed ribbons on hydrophobic CH_3-terminated SAM, and other surfaces represented high amounts of adsorption instead of forming any well-defined structures. Based on the extracted QCM-D data and AFM images, it seemed that hydrophobic interactions and hydrogen bonding at the interface dominated the interactions of and upon terminal modifications, electrostatic interactions play a minor role in driving the interactions at the interface.

Publications derived from some parts of this work

1 **Roozbeh Hajiraissi, Ignacio Giner, Guido Grundmeier, and Adrian Keller, *Self-Assembly, Dynamics, and Polymorphism of hIAPP(20-29) Aggregates at Solid-Liquid Interfaces*, Langmuir, 2017, 33 (1), pp 372–381, DOI: 10.1021/acs.langmuir.6b03288)**

2 **Roozbeh Hajiraissi, Marcel Hanke, Yu Yang, Belma Duderija, Alejandro Gonzalez Orive, Guido Grundmeier, and Adrian Keller, *Adsorption and Fibrillization of Islet Amyloid Polypeptide at Different Self-assembled Monolayers Studied by QCM-D, AFM, and PM-IRRAS* (Langmuir, DOI: 10.1021/acs.langmuir.7b03626)**

Table of Contents

To the memory of my grandma and grandpa who made my childhood beautiful

Fatima Hajialifini and Farajollah Farahani

Dedicated to my beloved parents and sister who are not only my family, but also my friends and support and encourage me

Fariba, Iraj, and Rashno

And to Dr. Adrian Keller

who not only gave me my dreams, but also showed me that impossible is impossible

Also dedicated to

our hard-working boss Professor Guido Grundmeier

who trusted on me and let me follow my education in his internationally famous interface group.

The only way which I found to show him my appreciation was publishing the works

I appreciate Dr. Christoph Ebbert and Dr. Mike Bobert from my heart who helped and supported me during my work.

I thank Professor Yousef Jahani who gave me self-confidence in working independently.

I am also thankful to Charlotte Kielar who helped me to read and translate in German.

Last, but certainly not the least, I appreciate Saminathan Ramakrishnan, Dr., Pramod Vincent Menezes, Dr. Ignacio Giner, Ms. Annette Lefarth, , Dr. Teresa de los Arcos de Pedro, Mr. Ralf Hamann, Mr. Markus Voigt, Dr. Markus Wiesener, Nelli Gurin, Yu Yang, Marcel Hanke, Shuping Song, Chen-Ni Liu, Bastian Mesonbach, Christian Hoppe, Richard Grothe, Stefan Waschke, Julia Weiß, Rabea Schreckenberg, Martin Wiesing, Dr. Alejandro Gonzalez Orive, Ms. Claudia Altmiks, Ms. Gisela Jünnemann-Held, Ms. Marlies Daniels, and Mr. Thomas Arens, people who helped/taught me.

Roozbeh

Chapter 1

Introduction

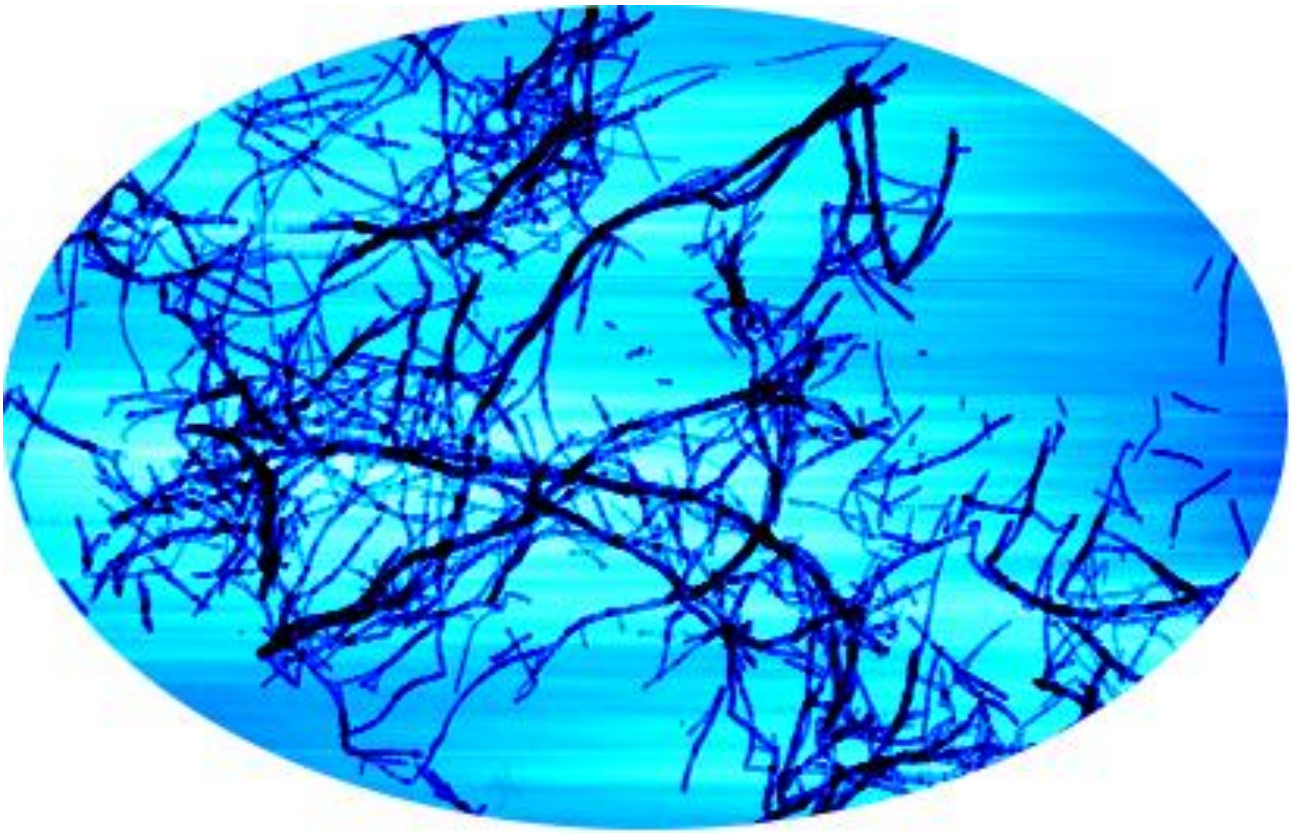

Self-assembly is a process in which various components form an organized, well-defined structures with one- to three-dimensional arrangements (Huie 2003). In this process, degree of perfection is relatively high which derives from energy balance and various mechanisms such as electrostatic and surface forces, chemical interactions, hydrophobic and hydrophilic interactions (Lee 2011). In spite of the fact that self-assembly in nature is considered as an advantage since it leads to formation of precisely formed structures, in vivo the self-assembly of bio macromolecules initiates the first steps of misfolded diseases such as Alzheimer, Parkinson, and Type2 Diabetes Mellitus (T2DM). The aforementioned diseases are accompanied by presence of intra/extra cellular deposits so-called amyloid plaques. The main constituents of the observed plaques are *fibrillar* entities (Dobson 2001) which compose of orthogonally aligned β-strand along the *fibril* and are stabilized by hydrogen bonds (Goldsbury et al. 2011). Although it was revealed that fibrillization mechanism shares a similar pathway in all amyloidgenic peptides/proteins, varying polymorphism among the fibrils not only from different sources, but also from a same family drew the attention of researchers to analyze the controlling parameters in fibrillization process (Goldsbury et al. 1997).

The peptide/protein chooses many conformational states in order to reach to native state with lowest level of energy. In case of not forming the native state, many interactions lead to misfolded structures, one of which is appeared as *fibrillar* morphology which contributes to the misfolded diseases (Stefani 2008).

Fibrillogenic peptides/proteins represent different morphological structures, and increasing evidence shows that many factors affect the fibrillar structure (Goldsbury et al. 1997; Chiti and Dobson 2006). The fibrillar structure represents the structural morphology with diameter of 6-12

nm and length of several microns (Westermark et al. 2005; Stefani 2008). The studies are designed to involve effects of mutation, bulk condition, surface *etc*. on aggregation and fibrillization to deeply understand the parameters controlling the fibrillization.

Biophysical studies choose various conditions in order to study the conformational states and conversion of amyloidogenic peptides/proteins into different morphologies such as oligomer, protofibril, and fibril to mechanistically establish governing roles. As fibrillization occurs in a complex environment and many biological surfaces are in close contact with the peptides/proteins, the presence of surface may give rise to many conformational states which spark the intermolecular interactions and favor the fibrillar self-assembly. The fibrillization mechanism in bulk is basically controlled by bulk condition such as pH, and temperature, however, at contact with surfaces physicochemical properties and topography of the surface influence the morphology and kinetics of fibrillization (Arosio et al. 2015). To mimic the biological surfaces such as cell membranes, different surfaces with varying surface chemistry and topographical features such as lipid bilayers (Knight et al. 2006), polymeric surfaces (Jeworrek et al. 2009), and inorganic substrates (Hajiraissi et al. 2017) are employed to analyze and extract interfacial phenomena undergoing at biointerface. It should be pointed out that the fibril self-assembly is not only dependent on the surface characteristics, but also is related to the chemical characteristics of the peptidic monomer which determines the way it interacts with surfaces via hydrophobic or electrostatic interactions. As was observed and reported, exposure of amyloidogenic peptide amylin to hydrophobic surfaces enhances the amount of adsorption (Jeworrek et al. 2009) and the rate of fibrillization is under control of surface chemistry whose rate becomes retarded and

increases upon contact with hydrophobic (Keller et al. 2011a) and negatively charged surfaces (Hajiraissi et al. 2017) respectively.

In the course of type2 diabetes mellitus (T2DM), the observed fibrillar entities are the consequence of polymerized amylin (islet amyloid polypeptide (IAPP)), a 37 residue hormone which is synthesized in pancreatic β-cells of Langerhans and consecrated with insulin (Westermark et al. 2011). Increasing the ratio of IAPP to insulin leads to formation of various states of IAPP aggregates such as oligomers, protofibrils, and fibrils whose accumulations lead to β-cell apoptosis which is observed in diabetic patients (Engel et al. 2008). Various mechanisms have been proposed to be responsible for β-cell apoptosis and each mechanism ascribes the dysfunction of β-cell to the presence of specific species such as oligomer or proto/fibril (Chiti and Dobson 2006). Based on reported works, it seems that in β-cell failure, the process of fibrillization, in which oligomers are transferred into mature fibrils, rather than a specific species contributes to the β-cell burst (Pillay and Govender 2013). In this regard, many experimental conditions and the IAPP monomer with different mutations are used to appraise the effect of intermediates on β-cell disintegrity and fibrillization mechanism. It is not also far from expectation that model surfaces can serve to involve different parts of the polypeptides in order to understand the roles of different parameters on aggregation and fibrillization.

In addition, classified as nano biomaterials, peptides/proteins with capability to self-assembly in the range of nanometer have drawn the attentions from disease point of view to application development. From technological point of view, the self-assembly ability of the proteinaceous materials is used to tailor functional nano biomaterials (Knowles and Mezzenga 2016) such as functional coatings (Mostaert et al. 2006), bio sensors (Hauser et al. 2014), and nanowires (Reches

and Gazit 2003). Consequently, it would be of interest to employ different nano biomaterials and choose various experimental conditions to find out the fibrillar self-assemby from technological point of view.

Chapter 2

Fundamentals

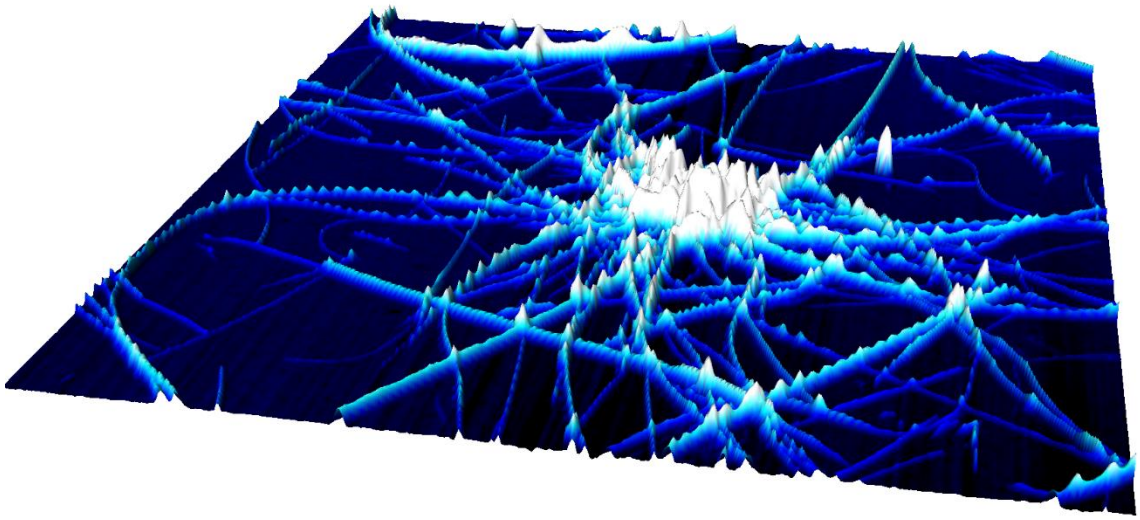

2.1 Proteins

Proteins which are products of living organisms contain monomeric units bonded covalently to form macromolecular structures. The discernible difference between biopolymers and synthetic polymers lies in their structures. Biopolymers often encompass well-defined structure with narrow molecular weight distribution, whereas synthetic polymers show broad molecular weight distribution.

Amino acids are the primary monomeric units of proteins which are linked covalently to form peptide bonds. Upon polymerization, amino acids, the position of which is referred as *residue*, release either a hydrogen ion from the amine end or a hydroxyl ion from the carboxyl end, or both, as a water molecule released during formation of each amide bond. All peptides contain N-terminus and C-terminus residues at two ends of their chains (Bohinski 1987). The side chains as *R* groups are determinant agents which functionalize amino acids. Amino acids are classified into two main categories, according to potential of *R* group to interact with water at pH 7: *i)* hydrophobic amino acids which do not have propensity to water and are nonpolar, *ii)* hydrophilic or polar amino acids which are able to bind water molecules through hydrogen bond and/or according to their ionization state can carry positive or negative charges on their *R* groups. If the side chain functions as the Brönsted base, the R group carries positive charge, and in case of functioning as acid the side chain is negatively charged amino acid. Otherwise, carrying no charge leads to formation of neutral amino acids functioning as hydrophobic and hydrophilic amino acids (Bohinski 1987; Blackstock 1989).

Proteins have been divided into four levels of structures: primary, secondary, tertiary, and quaternary structures (Bohinski 1987; Blackstock 1989).

i) *Primary structure* consists of linear sequence of amino acids and peptide bond is the main chemical binding which keeps the amino acids in the peptide chain.

ii) *Secondary structure* is defined as the conformational arrangement of protein backbone in space. Pauling in 1951 introduced two types of secondary conformations as (α-helix and β-sheet) and it was proposed that hydrogen bonds among the peptide bond atoms lead to special orientation of peptide chains in space (Pauling et al. 1951). α-helix structure is arisen from the interaction of C=O and N-H groups which promote helical coil. The so-called β-sheet represents a sheet-like structure and stabilization is the consequence of hydrogen bonds between the adjacent chains. This type of conformation is distinguished by parallel or antiparallel conformations of the peptidic chains.

iii) Third structure of polypeptides referring to the adaptation of peptide chain as global structure in space is defined as the tertiary structure. In peptides representing, global structure, hydrophobic interactions, hydrogen bonds, and intramolecular bonds (disulfide bond) among the amino acids contribute to formation a 3D structure.

iv) *Quaternary structure* which is classified as association of two or more polypeptides in space. In this structure, the aforementioned interactions in the tertiary structure except the disulfide bind keep the structure stable.

2.2 Protein folding & aggregation

When polypeptide is synthesized by ribosome, it passes many interactions and changes its primary random coil structure to reach to its final folded three dimensional state so-called *Native State* (Alberts 2002; Jahn and Radford 2008). During the conformational transition from unfolded state to native state (as the extremes), folding energy which is the consequence of hydrophobic interactions, hydrogen bonds, and van der Waals forces varies (Saunders and Deane 2010). By analyzing the theoretical and experimental results, Joseph Bryngelson and Peter Wolynes introduced *Energy Landscape* (see **figure 2-1**) (Bryngelson et al. 1995). The Landscape diagram illustrates the energy and the entropy levels in which the polypeptide chain frustrates and adapts respectively, to achieve the final native state (Wolynes et al. 1995; Dill and Chan 1997). Theoretically, the landscape energy diagram depicts the possible conformational states which the peptide chain adapts and frustrates the energy which is the consequence of forming of non-native conformations until the peptide chain obtains its minimal state of energy. Moreover, the diagram helps to predicts the various states such as oligomer state, aggregation and fibrillar self-assembly of peptidic chain (Jahn and Radford 2005; Vendruscolo and Dobson 2005). The way of energy frustration during the conformational transitions envisions a funnel-like diagram whose top represents the highest energy level on which unfolded conformations lie and during the finding the minimal energy state, the energy level decreases to the bottom of the diagram (Jahn and Radford 2008; Fabian and Naumann 2012). Small proteins due to their limited conformational changes, form a smooth and even funnel (Watters et al. 2007). However, large proteins because of forming many intermediates with various energy levels, replace the smooth diagram of the energy landscape with rugged diagram whose depth and width of the ruggedness are representative of

energy well and entropy states respectively (Vendruscolo et al. 2003; Brockwell and Radford 2007).

Despite obtaining the native state, peptidic chains are metastable and they are still able to form other intermediates. As a consequence of intra-, intermolecular interactions many proteinaceous structures such as oligomers, protofibrils, and fibrils appear. It is assumed that formed fibrils have the lowest energy level and narrow width which are reflective of the structural constraint and stability of the fibrillar structure (Wetzel 2006).

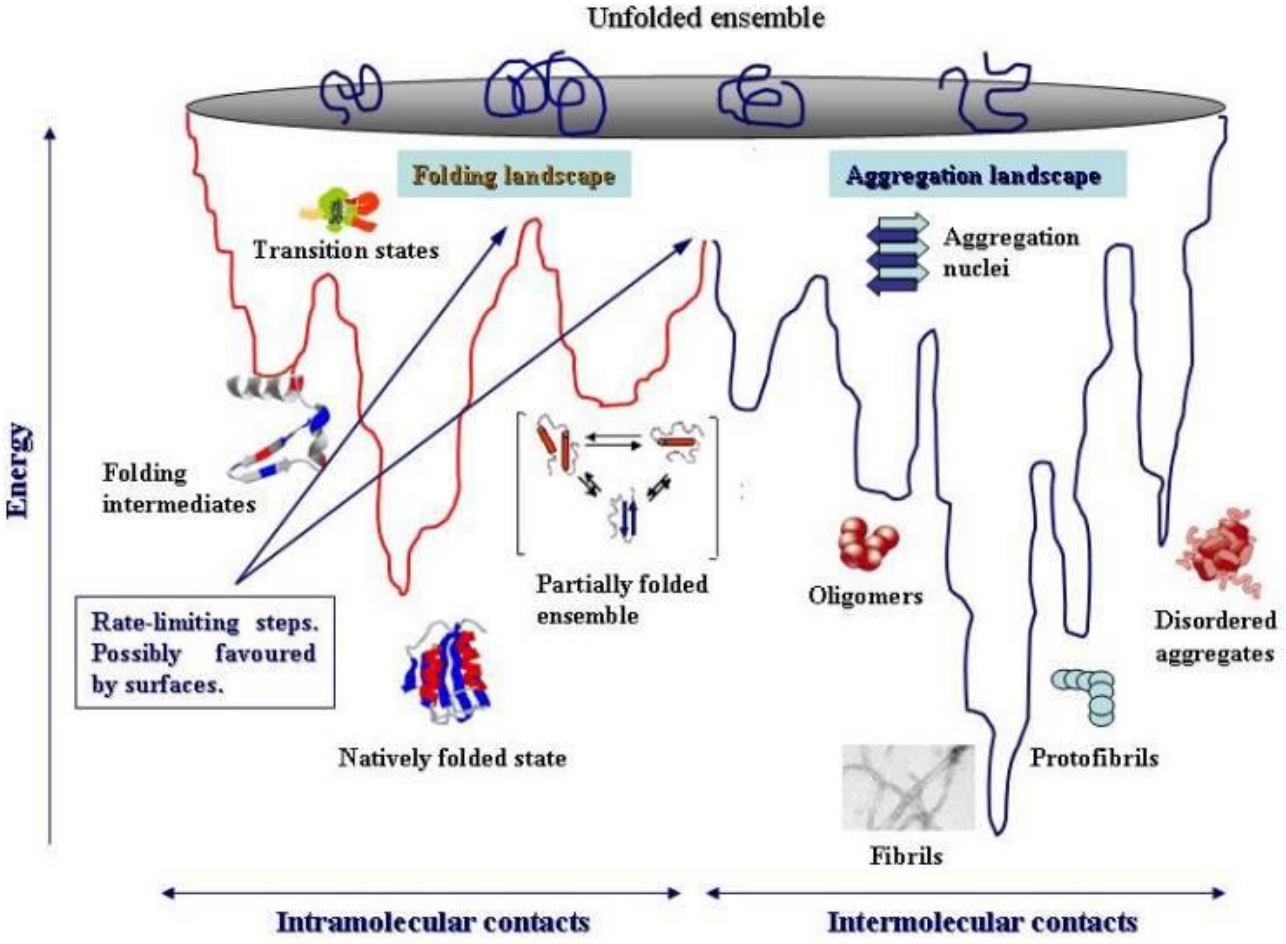

Figure 2-1 Landscapes of various stages of protein folding (Stefani 2008)

Kinetics of amyloid fibrillization which is commonly followed by specific binding of the fluorescent molecule Thioflavin T (ThT) (Biancalana and Koide 2010) is mirrored as a sigmoidal curve in which three different phases are observed (see **figure 2-2**); *i) lag phase* as an initial plateau in which thermodynamically prolonged nucleus formation converts unfolded monomeric peptide into a nucleus template as seed, *ii) elongation phase* as an exponential growth which is indicative of abrupt accretion and consumption of peptidic monomer to aforementioned template leading to fibrillar structures and formed/forming nuclei grow to form mature fibrils, and *iii) stationary phase* as a final plateau at which fibril growth becomes imbued and the system is at equilibrium state (Bhak et al. 2009; Arosio et al. 2015; Abedini et al. 2016).

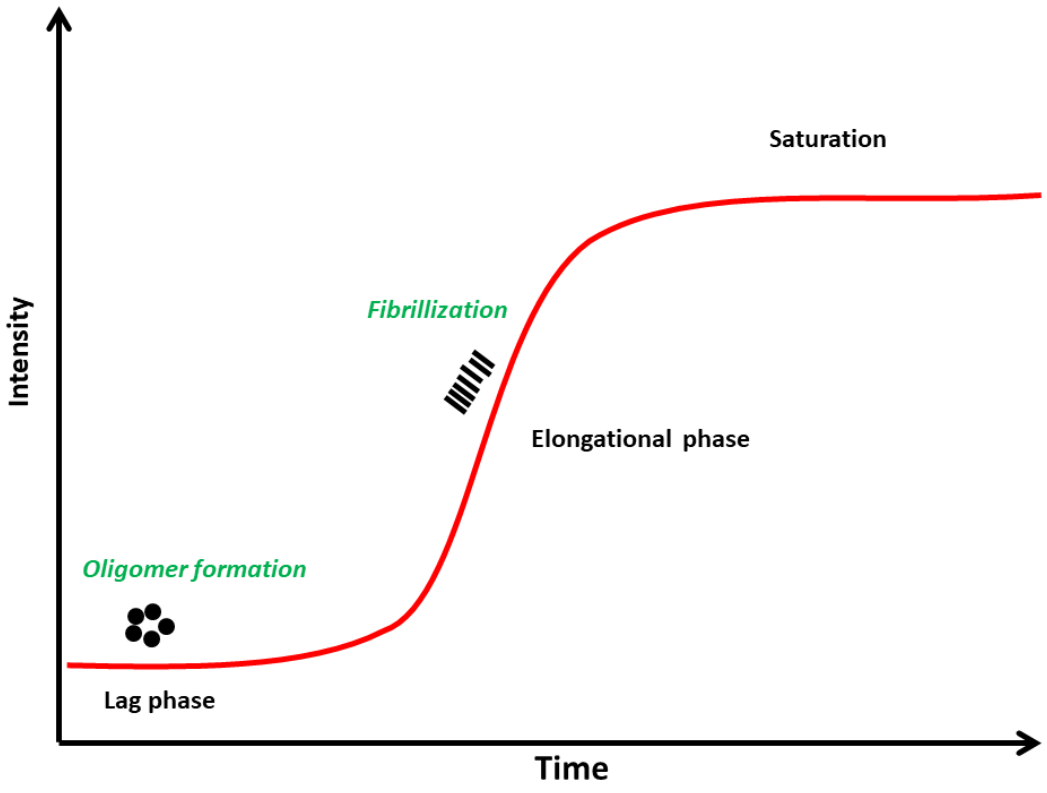

Figure 2-2 *Schematic fluorescence curve of amyloid aggregation*

The length of the lag phase is under control of many factors which determine the kinetics and speed of fibrillization. In general, the controlling parameters affecting the lag phase can be classified as pH, temperature, ionic strength, and peptide mutation which are described in the following:

pH*:* at isoelectric point (pI) the peptide/protein possesses zero net charge. Because of various side chains and amino acid sequence in peptide chain, proteins/peptides show varying charge states at different pHs. As a consequence of pH variation, charge state of peptide/protein changes which leads to different interactions at contact with surface or in bulk state (Rabe et al. 2011). pH lower than the pI makes the peptide susceptible to manifest positive charge state, whereas at pH higher than pI the peptide has potential to have negative charge state. Consequently, it can be expected that at pH lower or higher than pI, peptide/protein shows positive/negative charge states which leads to enhancement in peptide/protein adsorption at contact with surfaces with opposite charges as a result of electrostatic interactions between opposite charge states of the peptide and the surface (Hook et al. 1998; Bremer et al. 2004; Demanèche et al. 2009). To exemplify, human islet amyloid polypeptide (hIAPP) as a hormone synthesized in pancreatic islands of Langerhans has the pI point at pH 10 (BACHEM) and in physiological condition (pH 7.5) has three positive amino acids (Lys1, Arg11, His18) in addition to its N-terminal charge which cause the peptide chain to show a net charge of +4 (Cao et al. 2012). It is interesting to note that, based on neutral charge state at pI, peptides/proteins experience the least electrostatic peptide-peptide repulsion. Therefore, at contact with surface, packing density at pI is maximized (Rabe et al. 2011).

Temperature: physiological environment in healthy condition, in human, is naturally set at 37°C. Consequently, directing the peptide/protein interactions either in bulk state or at contact with

various surfaces would be straightforward to correlate the obtained data to in vivo observations. However, there are many experiments which have been conducted at room temperature in order to better analyze peptide/protein's behavior in detail (Nakanishi et al. 2001). Temperature as one of the main parameters affecting the adsorption, makes the peptide to change the conformation. The increase of temperature is in direct relation with increase in protein adsorption. From thermodynamic point of view, transition in peptide conformation, at high temperatures, is the consequence of obtaining highest level of conformational entropy (Nakanishi et al. 2001; Rabe et al. 2011). Sabaté *et al*. used the temperature as a variable. They reported that IAPP fibrillization was affected by varying temperature, since increasing the temperature causes the kinetics to speed and lag phase shifts to shorter times (Sabaté et al. 2010).

Ionic strength: presence of salt in solution influences the nature of protein interactions by either shielding the electrostatic interactions (Debye–Hückel effects) or changing the protein-solvent characteristics (Hofmeister effects) (Marek et al. 2012). In Debye–Hückel effects, Debye length determines that to what extent the electrostatic interactions extend. It was found that upon strengthening the ionic content of the solution, Debye length increases and electrostatic interactions lose their capability (Israelachvili 2011). Effect of the type of ion was reported first by *Franz Hofmeister* (Hofmeister 1888). He observed that salt ions have ability to change the behaviors of proteins in such ways that proteins can precipitate (so-called *salting out*) or dissolve in the solution (so-called *salting in*). In this regard, ions were classified into two groups: kosmotropes which promotes the protein precipitation (SO_4^{2-}, F^-, Mg^{2+} and Ca^{2+}), and chaotropes which enhance the protein solubility (ClO^{4-}, SCN^- and NH^{4+}) (Collins and Washabaugh 1985; Rabe et al. 2011). Marek *et al.* used different solutions with varying pH, various types of ions, and

different ion concentration (Marek et al. 2012). It was found that increasing the salt content affects the kinetics of amyloid fibril formation with various extents. It was mentioned that at both low and high values of pH, regardless of the type of salt, increasing the ionic strength leads to a reduction in lag phase and fibrillization proceeds faster. Despite manifesting similar sigmoidal fluorescent curves at low and high pHs, lag phase increased which is indicative of retarded fibrillization mechanism.

Peptide mutation: In the process of amyloid fibrillization, various amino acids participate in fibrillization and upon mutation/truncation, not only fibrillization kinetics, but also polymorphism of formed amyloid fibrils vary to varying extents. Goldsbury *et al.* employed wild type and truncated hIAPPs (1-37), (8-37) (Goldsbury et al. 2000). Interestingly, it was observed that structural characteristics of formed fibrils changed with respect to variation in monomeric structure. The variation in polymorphism was mirrored by changes in fluorescence intensity and lag phase of truncated hIAPP showed a shortened lag phase along with a slow exponential growth. On the other hand, wild type was represented by longer period of lag phase and steeper exponential growth (Goldsbury et al. 2000).

2.3 Human islet amyloid polypeptide

During dissecting of corpora amylacea of the brain by Rudolf Virchow, he observed aggregated deposits whose components were mainly fibrillar species. The terminology *amyloid* refers to the proteinaceous deposits found in infected organs, the most part of which is fibrillar deposits (Westermark et al. 2005). In amyloidogenic process the soluble proteins transform into insoluble

form (Bhak et al. 2009). The sequential attachment of the misfolded peptidic monomers leads to appearance of oligomeric, protofibrillar, and fibrillar structures whose presences in some cases spark degenerative disorders. Although self-assembly in nature can intrinsically be considered as an advantage, in vivo the existence of misfolded peptides leads to misfolded diseases such as Alzheimer disease, Parkinson disease, Huntington disease, and Type 2 diabetes mellitus (T2DM) whose responsible peptides are Aβ, α-Synuclein, huntingtin, and Amylin (islet amyloid polypeptide-IAPP) (IAPP) respectively.

In the context of T2DM, amyloid deposits in Pancreas compose mainly of a 37-residue peptide so-called IAPP (KCNTATCATQRLANFLVHSSNNFGAILSSTNVGSNTY) with amidated C-terminus which is a hormone and synthesized in pancreatic β-cells of Langerhans. The peptide is co-secreted with insulin from the β-cells in a molar (IAPP: insulin) ratio of 1:100 into the blood circulation and is cleared by peptidases in the kidney (Higham et al. 2000; Caillon et al. 2016). It is believed that the IAPP functions in carbohydrate metabolism, modulation of insulin secretion, and suppression gastric emptying (Jayasinghe and Langen 2007).

In more than 90% of T2DM patients, β-cell apoptosis is associated with appearance of amyloid fibril deposits. However, due to prompt conformational changes of IAPP monomer and its conversion into fibril during the cytotoxicity, the intermediates which are involved in onset of β-cell dysfunction have been not fully recognized. Primary results represented that membrane disruption is mainly followed by either barrel-stove model in which aggregated peptide causes pore across the membrane, or detergent-like model (carpet model) whose peptide-lipid connection disrupts the membrane integrity (Jayasinghe and Langen 2007). However, in a work reported by Engel *et al.* (Engel et al. 2008) the mechanism of cytotoxicity was proposed as a

sequential process in which various intermediates collaborate to induce membrane disintegrity. It was found that during the aforementioned process, hIAPP monomers aggregate and damage the membrane and fibrillar inclusion resides perpendicularly at the membrane. This preferential position of the fibril forces the bilayer to unfavorable angles leading to β-cell bursting (Engel et al. 2008; Milanesi et al. 2012).

Fibrillization mechanism is a successive process in which monomers are converted into mature amyloid fibrils. Pillay *et al.* (Pillay and Govender 2013) and Murphy (Murphy 2007) assigned specified terminologies to stratify and unify the definitions of amyloid intermediates which are observed during the amyloid aggregation as following:

i) *Monomer* is the elementary constituent of polypeptide chain which consists of polymerized amino acids.

ii) *Oligomer* is composed of aggregated monomers with globular form which has the diameters between 2.7 nm and 4 nm (Kayed et al. 2004).

iii) *Protofibril* has a linear filamentous structure which grows upon monomer addition at the tip of incorporated oligomer and/or end-to-end addition (Hajiraissi et al. 2017).

iv) *Ribbon/Sheet* is a flat structure which forms as consequence of lateral association of two, three and more protofibrils (Hajiraissi et al. 2017).

v) *Fibril* has a typical diameter of 5-20 nm which sometimes consists of multiple protofibrils twisted around each other (Goldsbury et al. 1999).

vi) *Non-fibrillar aggregate* is defined as amorphous amyloid aggregates (WARD et al. 2000).

Many works have been devoted to analyze and eventually establish a well-defined mechanism for amyloid fibrils. In the context of IAPP, Goldsbury *et al.* conducted a few works to deepen the understanding of amyloid aggregation (Goldsbury et al. 2000). During their works, they realized that amyloid aggregation and self-assembly of IAPP show polymorphic structures *e.g*. oligomer, protofibril, and fibril, and based on electron microscope (EM) images, the hIAPP fibrils appear in high order structure either as laterally associated 5-nm protofibrils, or left-handed coiled fibrils with 25-nm or 50-nm periodicities along the fibril axis (Goldsbury et al. 1997). From modeling point of view, they proposed a mechanism in which monomers form protofibrils and collateral association of protofibrils either as ribbon or twisted protofibrils leads to appearance of mature fibrils (Kreplak and Aebi 2006).

Structurally, fibrils consist of parallel β-strands orthogonal to the fibril axis. Various techniques such as nuclear magnetic resonance (NMR), Fourier Transform Infrared (FTIR), and X-ray diffraction (XRD) have been employed to analyze the position and orientation of potential amyloidogenic regions of peptides in β-pleated sheets. Consequently, various hypotheses together with molecular simulations have been proposed to render better conception about the amyloid self-assembly. Latest model proposed by Sawaya *et al.* proposes that the hIAPP monomer forms a U-shape conformation, and based on crystallography experiments, the protofibril consists of two parallel β-strands which are donations of two monomers in order to form β-sheet (Sawaya et al. 2007; Wiltzius et al. 2008).

Another feature of the hIAPP is the formation a disulfide band between Cys2 and Cys7 where a loop in the region of (K1-A8) forms which makes this region unstructured (Wiltzius et al. 2008). In the time course of the self-assembly, the hIAPP(1-37) protofilaments tend to coil around each

other with left-hand turns along the fibril axis. Kajava *et al*. proposed that presence of disordered region of 8-11 and electrostatic repulsion between K1 and R11 in N-terminal region make the peptide monomer to manifest larger inter-serpentine spacing (0.02 nm) in which induce the protofibrils to tilt by 20° and to manifest a left-hand coil conformation (Kajava et al. 2005).

Interestingly, rat variant of IAPP, which has 84% amino acid sequence analogy to hIAPP, does not possess any fibrillogenic trend. Despite showing similar mechanisms in membrane binding of rIAPP and hIAPP at the initial stage of amyloid aggregation, rIAPP does not show any membrane toxicity. This inability has been ascribed to the presence of three proline residues (Li et al. 1996). However, recently, it was well understood that other residues contribute to fibrillar assembly of rIAPP and there exists a tuning behavior shared by all residues, and even proline at position of 28 can fortify β-sheet formation, based on π-π interactions (Jaikaran et al. 2001; Gazit 2002).

2.4 Adsorption

In various complex systems such as body molecules come into contact with various surfaces. The influential surface characteristics lead to different molecular interactions at adsorbate-adsorbent interface. Upon adhering to the surface, a protein layer forms, the thickness of which varies from monolayer to multilayer. During the process of adsorption basically gaseous molecules, liquid, or dissolved solids in solution adhere to the surface and based on the nature of the interaction, the formed layer shows reversible or irreversible characteristics. The aforementioned process is scientifically referred as *adsorption, in* which the amount of adsorbate is determined by adsorption function $\tau = f(P)$ and plot of which (y-axis as amount of adsorbate τ per unit area and

x-axis as pressure P if the medium is gas) renders the *rate and form* of the forming mono/multilayer (Butt et al. 2003).

Based on the adsorbate-adsorbent interaction, two types of adsorptions are defined: i) physisorption, ii) chemisorption. In the former, the adsorption mainly proceeds via physical interactions such as Van der Waals attractions, whose heat of adsorption is low (20-40 kJ/mol) and the adsorbate has capability to manifest desorption potential. On the other hand, in chemisorption chemical bonds form between adsorbate and adsorbent which lead to changing the surface chemistry and as a consequence of strong interactions the adsorbate becomes immobilized on the substrate. Compared to the physisorption, chemisorption, according to the formed chemical bonds, possesses higher value of the heat of adsorption in the range of 100-400 kJ/mol (Dąbrowski 2001; Butt et al. 2003).

In principle, the adsorption isotherms are classified into eight general trends, types of which have been observed experimentally: linear, Freundlich, Langmuir, Sigmoid, BET1, BET2, High affinity, and Step isotherms as represented in **Figure 2-3**.

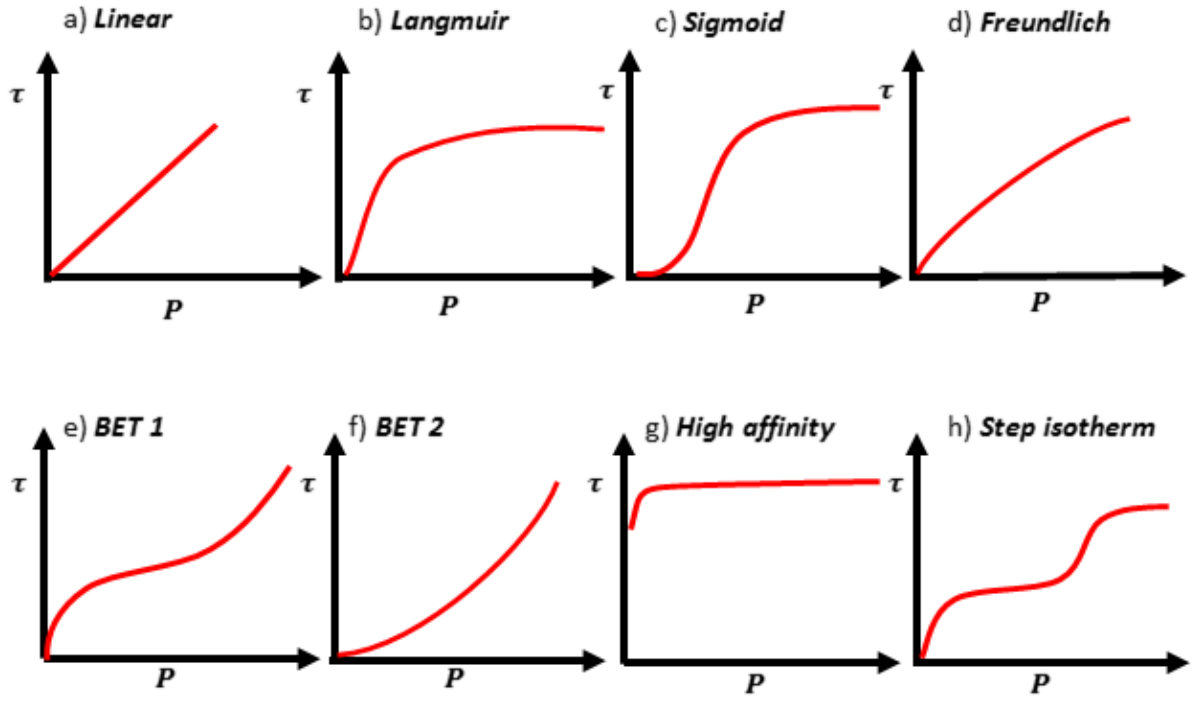

Figure 2-3 *Schematic of eight adsorption isotherms*

The simplest form of adsorption isotherm as *Linear isotherm* graphs and correlates the amount of adsorbate to the partial pressure or concentration of the adsorbate linearly. As this model resembles the Henry's law, this equation is also called *Henry adsorption isotherm equatio*n (Erbil 2006):

$\tau = K_H P$ (1

where K_H is a constant having dimension of (mol/Pa.m^2).

Another type of adsorption referred as *Langmuir model* is representative of *Langmuir adsorption isotherm*. In this model, the adsorbate is assumed as an ideal gas at isothermal condition and the adsorbent is an ideal solid with distinguishable reacting sites on the surface. This adsorption isotherm is based on four assumptions as the following (Langmuir 1918):

1) The substrate is flat
2) All reacting sites are similar and follow same mechanism of adsorption
3) Neighboring adsorbates do not interact with each other
4) Each reacting site is capable of holding one molecule which leads to monolayer formation

In Langmuir adsorption equation the fractional coverage θ is related to the adsorbate's partial pressure P_A by Langmuir constant K_L and adsorption reaches to a plateau at high concentrations:

$$\theta = \frac{\tau}{\tau_{mon}} = \frac{K_L P_A}{1+K_L P_A} \qquad (2$$

where τ_{mon} is the maximum amount of adsorbate which forms a monolayer.

In *Sigmoidal type*, adjacent molecules interact with each other and upon binding to the surface denser adsorbate's layer forms. As can be inferred from this type of adsorption, at the beginning of adsorption, isotherm curve proceeds slowly and in the mid time adsorption shows a sudden enhancement of adsorption which finally reaches to a saturated state at high concentrations (Hans-Jürgen Butt 2003).

Freundlich adsorption isotherm was firstly introduced by Hebert Freundlich in 1909 (Freundlich 1909). By this empirical equation the τ is related to the pressure of the adsorbate.

$$\tau = K_F P^{1/n} \qquad (3$$

K and n are the constants of the adsorbed molecule at the constant temperature. This equation is also presented in logarithmic form:

$$log\tau = logK_F + \frac{1}{n} logP \qquad (4$$

Where P is the equilibrium pressure of adsorbate. The graph represents a typical exponential trend until it reaches to a saturation pressure P_s. From this point on (higher pressures), the equation loses its ability to graph a proper adsorption isotherm.

In order to expand the Langmuir monolayer adsorption theory to other systems with multilayer structures, Brunauer, Emmett and Teller, based on several hypotheses, introduced BET theory of adsorption, known as *BET adsorption isotherm* (Brunauer et al. 1938). The assumptions are as following:

1) Because of physisorption multilayer adsorbate forms
2) Adsorbate molecules interact just with their neighboring molecules
3) Langmuir adsorption theory is valid for each layer

According to the aforementioned assumptions, the following equation defines the adsorption process of adsorbate onto the solid surface:

$$\frac{n}{n_{mon}} = \frac{K_{BET}}{(1-\frac{P}{P_0})\left[(1+\frac{P}{P_0})(C-1)\right]}\frac{P}{P_0} \qquad (5$$

where n is the total of number of adsorbate per unit area and n_{mon} is the representative of the amount of adsorbate in a monolayer per unit area. and P and P_0 are saturation and equilibrium pressures. K_{BET} as BET constant is calculated by heat of adsorption:

$$K_{BET} = \exp(\frac{E_1 - E_L}{RT}) \qquad (6$$

Here, E_1 and E_L are heat of adsorption of the first layer and higher adsorbed layers respectively.

In general, two types of adsorption mechanisms can be fitted by BET theory. In some systems the adsorption at low pressures leads to monolayer formation which is reflected by first concave in low level region of pressure (BET1). After this point, at higher pressure values an enhancement in the level of adsorption is observed, which is the consequence of formation of thick layer of adsorbate. In another class (BET2), due to stronger propensity of adsorbate molecules to interact to each other than to adsorbent, from the beginning of the adsorption process an increasing curve is the typical trend of the adsorption mechanism (Butt et al. 2003).

Seventh type of adsorption isotherm is referred as high-affinity adsorption isotherm in which adsorbate forms strong links at contact with adsorbent (Butt et al. 2003). The last adsorption curve shows a step increase in adsorption. In the first step a monolayer is formed which can be defined by Langmuir theory, and after increasing the pressure, layers of adsorbate start to cover the solid surface in step manner leading to formation of a multilayer (Butt et al. 2003).

2.5 Protein adsorption

To describe the protein adsorption mathematically, isotherm plots would be an efficient way to appraise and predict the adsorption isotherm. In the realm of protein adsorption, most of the models inspire from *Langmuir adsorption* as the base model and development such as involving the overshooting, and structural transitions are involved in this model to further predict various behaviors of protein systems.

Kinetically speaking, nine models have been proposed. The pristine model which simply plots the protein adsorption isotherm is referred as *Langmuir adsorption*.

$$\frac{d\theta}{dt} = k^{on}.C_s.\left(1 - \frac{\theta}{\theta_{max}}\right) - k^{off}.\theta \qquad (7$$

where θ and θ_{max} are fractional protein coverage and the maximum surface coverage which no free unbinding regions are available on the surface. In order to involve the lateral interactions effect of bound protein-surface, k^{on} and k^{on} referred as on-rate and off-rate constants and are dependent of surface coverage, are involved in the equation (M. Rabe, D. Verdes, J. Zimmermann, S. Seeger 2008) . C_s is indicative of protein concentration directly above the adsorbent.

Another model which tries to close the experimental data with predicted adsorption isotherm is *Random Sequential Adsorption* (RSA) (Schaaf and Talbot 1989). As the first assumption, this model proposes that the surface is not fully covered with protein adsorbate. This model was mainly proposed for desorption, diffusion, and structural rearrangement of adsorbed proteins at surface (Schaaf et al. 2000).

By taking the irreversibility and reversibility of adsorbed proteins, McGuire *et al.* suggested a Two-States Model (McGuire et al. 1995). This model suggests two hypotheses in which protein represents two adsorption pathways. Based on the first hypothesis protein starts to adsorb to the surface at the beginning of exposure of the protein to the surface which is reversible step and in the following the protein manifests transition state which is irreversible step (transition model). Another adsorption pathway suggests that the protein either shows reversible behavior at the beginning of surface adsorption or binds to the surface in irreversible pathway (*two-path model*).

In *Multiple-States Model* which is the improved transition model of the McGuire, supposes that during the protein transition at surface, because of increasing tendency of the protein to the surface, protein spreads over the adsorbent (Szollosi et al. 2004).

Lateral interactions of proteins in the time course of the adsorption were involved in the adsorption isotherm by Wahlgren *et al*.. In the suggested adsorption isotherm *Monomer/Dimer Exchange* (Wahlgren and Elofsson 1997), pre-adsorbed monomers are replaced with either monomer or dimer. It is also suggested that adsorbed monomers and dimers are able to establish lateral interactions which lead to structural transition and enhancement of attachment to the surface.

As was mentioned earlier, one of the effects observed during the protein adsorption is overshoot behavior during the adsorption process. This behavior was involved in a model so-called *Rollover Model* by Wertz *et al*. (Wertz and Santore 2001). Upon protein adsorption which protein holds end-on position, due to weak protein-surface interaction, the protein takes a side-on orientation which results from the higher affinity of the adsorbent to some regions of the protein structure. As a consequence of side-on orientation, the protein spans more surface compared to end-on orientation and this enhancement of surface coverage which is reflected by a maximum peak in the mid time of the protein adsorption is referred as the overshooting behavior.

Taking the aforementioned models into account, it can be seen that all models consider the adsorption isotherm with various protein adsorption behaviors. That is, the protein shows different propensities of irreversible/reversible trends during the adsorption at all stages of adsorption process. Rabe *et al*. proposed a model the value of which can be the contribution of all the adsorption stages to one model as *Three-States Model*. The adsorption process is divided into three steps: i) irreversibly starting adsorption stage, ii) reversible intermediate stage, iii) irreversibly attached protein stage. At the beginning of adsorption, the protein is irreversibly attached to the adsorbent and starts to cover the surface. Shifting to the second stage is the result

of lateral interactions of proteins with each other. Upon reaching to the maximum of surface coverage, the third stage of adsorption starts in which the conformational transition occurs and the adsorbed protein monomers adopt a relaxed conformation. Rabe *et al*. considered that during the transition to second stage, the adsorbed proteins show ability to alter their surface tendency by showing desorption. The occurred desorption process in this stage is mirrored by overshooting characteristic in adsorption isotherm plot (Rabe et al. 2007).

In one of the models added to the library of protein adsorption isotherm, it is considered that adsorbed proteins as monomer, dimer, trimer, etc., make interactions with adsorbing proteins and form clusters in varying sizes. The adsorbing proteins are able to adsorb to the adsorbent individually and migrate towards the existing clusters or they can be adsorbed by existing clusters. This model known as *Surface Cluster Model* was firstly proposed by Minton *et al*. (Minton 2001). In the following, Rabe *et al*. expanded the Minton's model to *Tracking Model* (Rabe et al. 2008). They assumed that the adsorbing proteins to the surface are attracted by the electrostatic interactions between the protein and surface. However, lateral electrostatic repulsion between the adsorbing protein and pre-adsorbed protein guides the protein monomer to reside in the proximity of the other proteins. As a matter of electrostatic interaction/repulsion, the surface coverage shows homogeneity. In other words, some areas possess highly dense layers of proteins, and some areas show loosely packed structures.

Implantation, drug delivery, and sensor are the newly introduced techniques in therapeutic application which are becoming widespread in medical applications. In these techniques the efficiency of the technique depends on the protein-substrate interaction. When an external material enters the body, the immune system attacks the alien by existent proteins in the blood

stream. Henceforth, the undergoing interactions between the protein and the alien lead to acceptance or rejection of the guest material.

In biological environment the peptide/protein exposes to many biological surfaces and aggregation and fibrillization mechanisms become more complicated. Accordingly, protein adsorption onto the adsorbent is a complex mechanism which depends upon various parameters.

When the protein comes into contact a solid surface, peptide/protein's characteristics such as size, structural stability, and amino acid sequence are the main parameters which should be taken into consideration in order to interpret the complexity of adsorption mechanism (Rabe et al. 2011). Upon exposure to the surface, peptide/protein changes the conformation in order to gain the minimum Gibb'S free energy (Norde 1996). This process consists of conformational transition from one state to more stable state. Proteins with small and rigid structures like Lysozyme and β-Lactoglobulin show low propensity to conformational changes (Norde 1996, 2008). On the other hand, bigger proteins whose sequences consist of hydrophobic, hydrophilic, negative, and positive regions behave in such a way to reach to minimum free energy (Rabe et al. 2011). Therefore, upon exposure to a hydrophobic interface, the protein exposes the hydrophobic domains to the interface. Consequently, with respect to charged surfaces, it can be also inferred that because of electrostatic attraction between oppositely charged species, the negative and positive sequences bind to oppositely charged substrates which leads to enhancement in adsorption process. Once the protein is attached, the attachment mechanism can be implemented via long axis or short axis of the protein structure to the solid surface, the former as side-on and the latter as end-on orientation. As a matter of protein layer density: the end-on orientation has higher density than side-on orientation (Wertz and Santore 2002; Noinville et al. 2003; Karlsson and Carlsson 2005).

However, it should be implied that after surface saturation, electrostatic repulsion between neighboring proteins due to adjacent residues with similar charges becomes dominant which leads to reorientation and lowering the protein layer density (Tie et al. 2003; Rabe et al. 2007). This lateral interaction which is called "*catalysis of desorption"* may be the consequence of collision of adsorbing proteins with the pre-adsorbed proteins which leads to decrease in layer density and even desorption (Kurrat et al. 1994). Interestingly, the inverse behavior was also in some cases observed so-called *cooperativity*. To better clarify this effect, the *Langmuir adsorption isotherm* should be considered as the main undergoing isotherm. Based on this model, if the adsorption isotherm is faster than the reference model, it is called *positive cooperative adsorption*. In case of slower rate of adsorption compared to the reference model, isotherm is referred as *negative cooperativity* and when the adsorption isotherm follows the same trend similar to Langmuir model, the model is referred as *non-cooperative isotherm* (Chatelier and Minton 1996; Minton 2000, 2001). In addition to the aforementioned structural arrangement on surface, several isotherm curves represent an optimum before saturation. This behavior is defined as *overshooting* and the isotherm model defined for this type of trend is labeled as *time delay model* (Rabe et al. 2011). Various interpretations have been proposed to better evaluate the overshoot behavior. Vroman *et al*. postulated that in a system containing different proteins with different sizes, the surface is covered with small molecules, however, during the time course of adsorption, the small adsorbed molecules are replaced with larger molecules with higher affinities to the surface (*Vroman effect*) (Vroman et al. 1971; Vroman et al. 1980). Other explanations were given by Daly and Wertz. They interpreted overshoot trend as rearrangement of end-on orientation with side-on

orientation which the overshoot is the consequence of occupying more surface coverage (Wertz and Santore 2002; Daly et al. 2003).

surface topography also plays a pivotal role in protein adsorption. Interaction between biomaterial and biological molecule is under control of texture and physicochemical properties of surface which play important roles in protein adsorption and formation of the protein layer on the biomaterial surface. Over the last decades, various techniques have been introduced to fabricate different surfaces with varying texture, roughness (Rechendorff et al. 2006), and size (Flemming et al. 1999; Lord et al. 2010; Scopelliti et al. 2010). As in vivo interactions are in the range of nanometers, fabricating surfaces with nanoscale topographies render valuable information about the undergoing interactions in vivo. In this regard, various techniques such as photon lithography, electron-beam lithography, nano-imprint lithography, and laser modification have been introduced in order to mimic textures such as grooves, pits, ridges, steps, waves, wells, pores, spheres, cylinders, and general roughness whose influences are experienced by biological molecules once they come into contact with various existent surfaces (Flemming et al. 1999; Lord et al. 2010).

In biological research, the study of surface structure (nano/micro scale) draws the attention of researchers to profoundly analyze the surface characteristics on protein adsorption, since in designing the bio materials (tissue engineering, drug delivery, bio sensing) the bio material surface is covered by protein which mediates the cell-surface binding (Mitragotri and Lahann 2009).

Although a regular trend in protein adsorption has not been recorded, it seems that protein size and protein type along with surface roughness (Scopelliti et al. 2010; Ouberai et al. 2014) are the

controlling parameters at the interface between protein and surface. The influence of surface roughness on Fibrinogen adsorption evaluated by QCM-D, showed that the adsorbed peptide layer increases with respect to increasing the surface roughness (Rechendorff et al. 2006). Additionally, fibrinogen was found to aggregate and form thick adsorbed layer in parallel with increasing the surface roughness in which increase in surface area gives rise to enhancement of fibrinogen uptake (Scopelliti et al. 2010).

In addition to the effect of surface roughness on protein adsorption, kinetics of fibrillization inspires from the surface roughness. In the time course of fibrillization, peptidic monomers are attached to the growing ends of the oligomers. The aforementioned mechanism was traced and observed by incubation of hIAPP on mica surface via AFM imaging (Goldsbury et al. 1999). The proposed mechanism assumes that in the presence of surface, monomers are adsorbed to the surface and the growth is followed by 2D diffusion of the peptidic monomers by attaching to the ends of the formed protofibrils (Yu et al. 2012). Based on observed track of single dye-labeled Aβ monomers, it was found that increasing the surface roughness hindered the 2D diffusion of monomers so that the presence of obstacles retards the 2D surface mobility. Consequently, retarded monomer mobility reduces the rate of fibrillization. On the other hand, presence of smooth polymeric surface was found to expedite the fibrillization mechanism by providing a bed to concentrate and facilitate the peptide-peptide interactions (Shezad et al. 2016) Interestingly, increase of surface roughness promoted the adsorption of Aβ monomers on the surface (Shezad et al. 2016).

2.6 IAPP Aggregation at Interfaces

The self-assembly process in bulk is followed by inter/intra molecular interactions and no confinement from the surrounding affects the aggregation. On the other hand, at contact with various model surfaces the liquid-surface interface plays a pivotal role in amyloid aggregation. Polypeptides which consist of polymerized amino acids possess various charge states whose interactions at interface stem from the hydrophobic, hydrophilic, negative, and positive natures of their individual amino acids and consequently, it can be expected that amyloid fibrillization varies by changing the physicochemical properties of the surface.

In the physiological environment many mechanisms are dominated by interfacial interactions between proteins and cells. Virtually, all amyloid fibrils represent a well-formed, long entities, however, closer look sheds light on the discrepancies among the formed fibrils whose heights, lengths, and periodicities are described as the structural polymorphism, the dissection of which deciphers the influence of surrounding on the self-assembly and aggregation. The amyloid fibrillization not only occurs in bulk, but carries on also at contact with surface. In vivo proteins experience different cell membranes where the onset and growth of amyloid fibrillization in some cases sparks the membrane cytotoxicity. In order to involve different characteristics of protein regions separately, various model surfaces are utilized. Over the last decades, various standard templates have been introduced and are commonly applied to experimentally extract polymorphism, adsorption, and dynamics of proteins at contact with various charged surfaces. These standard surfaces can in general be classified as: inorganic templates (mica, Silicon dioxide SiO_2, tantalum oxide Ta_2O_5, titanium oxide TiO_2(Hemmersam et al. 2005; Hovgaard et al. 2007; Hemmersam et al. 2008; Keller et al. 2011a; Yu et al. 2012a; Hajiraissi et al. 2017)), polymeric

surfaces (Cabaleiro-Lago et al. 2010), lipids (Green et al. 2004; Knight and Miranker 2004; Jayasinghe and Langen 2005; Knight et al. 2006; Lopes et al. 2007; Domanov and Kinnunen 2008; Dupuis et al. 2009; Nanga et al. 2009; Andrews and Winter 2011; Nanga et al. 2011; Caillon et al. 2013), and self-assembled monolayers (Love et al. 2005)

Based on the reported works, in the study of amyloid aggregation and fibrillization, model surfaces with different surface chemistry are used. Accordingly, surfaces with hydrophobic, hydrophilic, negative, and positive charge states are fabricated to study the adsorption, dynamics, and polymorphism of amyloid structures. In general, most of the studies show that protein has higher affinity to adsorb to hydrophobic substrate than to hydrophilic one (Jeworrek et al. 2009). Adsorption of hIAPP at contact with polymeric surfaces with varying polarities was investigated by neutron reflectometry and it was shown that the adsorption affinity reaches to the highest value when the peptide comes onto contact with the hydrophobic surface compared with positively and negatively charged ones (Jeworrek et al. 2009). The hIAPP also adsorbed to the positively and negatively charged surfaces, although not as remarkable as hydrophobic surface. Due to the positive charge state of hIAPP at pH 7.5 (Dupuis et al. 2009), electrostatic attraction led to peptide adsorption on negatively charged surface. On the other hand, electrostatic repulsion between positive hIAPP and positively charged surface decreased the amount of adsorption.

Increased amount of adsorption by hydrophobic surfaces motivated researchers to not only analyze the amount of adsorption, but also to investigate the kinetics and polymorphism of amyloid fibrillization. By using atomic force microscopy (AFM) and fabricating hydrocarbon-modified mica surface with varying degrees of hydrophobicity, the speed and morphology of amyloid fibrillization of hIAPP showed that increasing the surface hydrophobicity decelerates the

fibrillization and amyloid fibrils were replaced with oligomeric species (Keller et al. 2011a). The retardation trend of fibrillization was also observed in the presence of copolymeric particles whose effects was related to the depletion of peptide monomers in solution by migration to surface of the copolymer (Cabaleiro-Lago et al. 2010).

Cells usually contain 10-20% (Rustenbeck et al. 1994) negatively charged lipids and these partially negatively charged cell membranes function as a template to structure the hIAPP towards amyloid fibrils (Sparr et al. 2004; Engel 2009). As a result, it was observed that the hIAPP shows different rates of fibrillization on the lipid bilayers. Upon contact with negative lipid substrate and enhancement of the negative portion of the lipid bilayer, it is seen that the hIAPP represents accelerated amyloid fibril formation compared with zwitterionic and cationic lipids (Knight and Miranker 2004; Lopes et al. 2007; Caillon et al. 2013).

In addition to evaluated rate of fibrillization, the polymorphism of the hIAPP showed that the formed morphology on freshly mica surface is under control of interface interaction and despite having tendency to show a coil structure in test tube, formed protofibrils and fibrils showed uncoiled structures with abundant portion of protofibrils. The observed discrepancy in polymorphism was ascribed to the imposed constraint from the surface on the hIAPP monomers which is derived from electrostatic interactions during the aggregation process (Goldsbury et al. 1999).

In addition to the extracted data regarding the polymorphism and kinetics of fibrillization, the hIAPP structuring while coming onto contact with surfaces was analyzed. By using lipid bilayers, it was revealed that half of the hIAPP is transferred into α-helical structure containing residues 9-22,

while positively charged amino acids point to the outermost surface of the lipid bilayer and hydrophobic residues face to the core of the bilayer (Jayasinghe and Langen 2005; Apostolidou et al. 2008). Interestingly, residues 23-37 remain unstructured and upon neighboring the other monomeric peptides, self-assembly and fibrillization spark (Westermark et al. 1990; Moriarty and Raleigh 1999; Tenidis et al. 2000). From thermodynamics point of view, binding to lipid membrane contains different stages of binding, folding, and permeation with different contributions of Gibs'free energy in which binding, partitioning, α-helical conformation, and β-sheet propagation allocate various amounts of Gibs'free energy (Knight et al. 2006; Lopes et al. 2007; Dupuis et al. 2009; Nanga et al. 2011).

Unlike the human IAPP, rat variant does not possess any fibrillogenic trend. Interestingly, the first step of membrane disruption which is ascribed to monomer binding to the lipid membrane, is similar in both human and rat variants. As a matter of conformational structure, the region 1-19 adapts an α-helical structure at lipid surface both in the hIAPP and the rIAPP (Nanga et al. 2009; Andrews and Winter 2011). However, after attachment to the membrane, presence of three prolines in region 20-29 in rat variant prevents the C-terminal region from formation of β-sheet structure at membrane (Westermark et al. 1990; Green et al. 2003). Nanga *et al.* analyzed the responsible region for membrane attachment, region 1-19 of hIAPP and rIAPP, in order to appraise the toxicity. NMR spectroscopy revealed that this region in the hIAPP is more buried within the lipid membrane, whereas the rIAPP(1-19) has more propensity to the membrane surface which gives rise to less toxic behavior. This behavior was ascribed to the presence and spatial conformation of N-terminal loop (region 2-7) where in the hIAPP faces the hydrophobic amino acids in N-terminal region to the membrane which favors membrane disruption, while in the rIAPP

prevents the hydrophobic amino acids of the region 1-19 from membrane binding (Nanga et al. 2009).

Chapter 3

Experimental Techniques

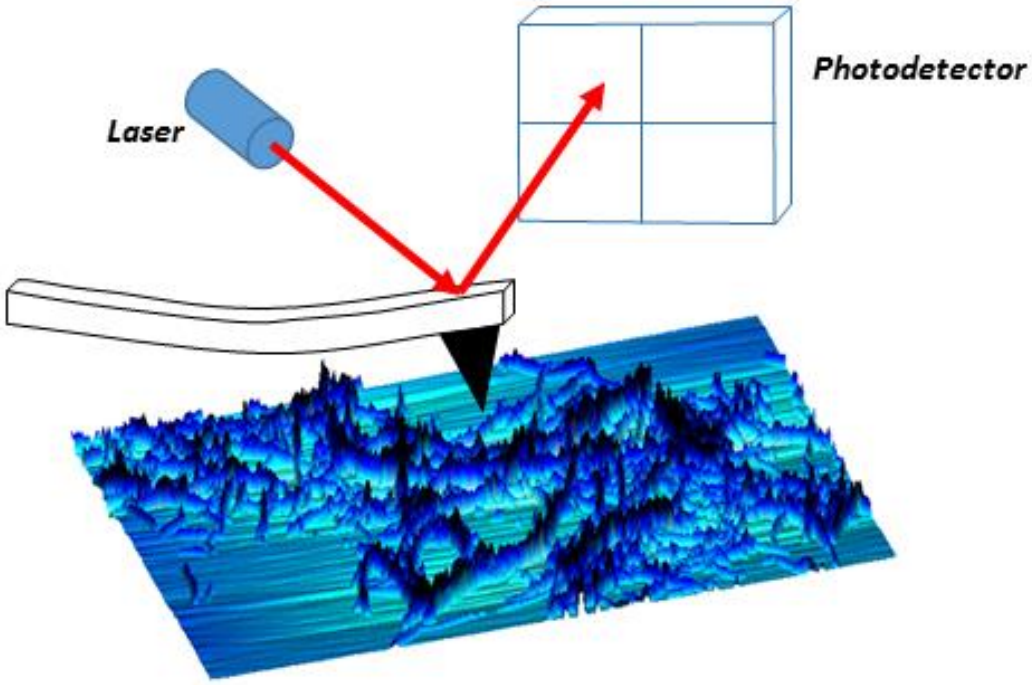

3.1 Quartz Crystal Microbalance with Dissipation Monitoring (QCM-D)

One of the techniques which its utilization glitters among the mass sensitive methods is quartz crystal microbalance (QCM) whose high sensitivity is considered as an advantage to detect the mass changes in the range of nanogram. Despite having being employed in the last decades, QCM is ascribed to Sauerbrey who extracted a linear correlation between resonance frequency ΔF and deposited mass Δm on quartz crystal sensor and as a consequence of his work an equation so called "*Sauerbrey Equation*" was established in 1959 (Sauerbrey 1959).

The nanogram sensitivity of QCM stems from the *piezoelectric effect*. This phenomenon was first discovered by Jacques and Pierre Curie in 1880. They found out that upon inserting a mechanical stress on quartz, an electric current is generated (Curie, Jacques, and Pierre Curie 1880). In the following works, Lippmann recognized the converse effect where the crystals were exposed to an external electric field, a mechanical strain was produced in crystals which is called "Inverse Piezoelectric Effect"(Lippmann 1881). Piezoelectricity is exhibited in 20 out of 30 of crystalline materials. This phenomenon is basically stems from electric dipoles within these materials. Quartz crystal lattice is intrinsically neutral, but when the crystal lattice is distorted due to compression or tension, the random orientation of dipolar domains becomes ordered and an alternating electric field is induced across the crystal. oppositely, when an electric field is applied, a mechanical stress is generated in crystal (O'Sullivan and Guilbault 1999).

Among the piezoelectric materials quartz possesses combined mechanical, electrical, chemical, and thermal characteristic which has made it commercialized. To fabricate an applicable quartz plate various cuts are applied, for instance, AT-, BT-, CT-, DT-, NT-, and GT-cut, which ensue various

piezoelectric and dielectric properties. Based on the type of quartz cut different resonators such as thickness-shear-mode (TSM) known as quartz crystal microbalance, flexural-plate-wave plate resonator (FPW), surface-acoustic-wave resonator (SAW), shear-horizontal-acoustic-plate-mode resonator (SH-APM) are fabricated (Janshoff et al. 2000).

It is well-found that AT-cut has almost zero temperature coefficient and the highest frequency stability at around room temperature. Consequently, in QCM the quartz with AT-cut is employed as template to analyze the kinetics of protein ad/desorption at functionalized surfaces coated with various organic (lipid) and inorganic (SiO2) materials.

In principle, three modes of operations are used to drive quartz crystal and to monitor resonance frequency. As the first and economic approach, an *oscillator circuits* is utilized to generate frequency at which the quartz starts oscillating (Arnau et al. 2002). However, limited extracted data based on one single frequency and lack of dissipation mode lower the applicability of this mode of operation. In *impedance analysis,* network analyzer and impedance analyzer are connected to each other to calculate electric conductance as a function of frequency sweep (Janshoff et al. 2000). In this technique band-width of the resonance frequency is extracted by fitting the conductance and resonance curves. The last method as *ring-down*, is applied in QCM-D in which a sudden exciting voltage is generated across the electrodes and upon cessation of the voltage, a decaying sine curve represents the period of oscillation and decay rate (Sittel et al. 1954).

Expansion and contraction of quartz crystal, as a consequence of applied voltage with frequency close to the resonant frequency of the crystal f_0, give rise to a standing wave. As a matter of

sensitivity, it can be concluded that the thinner the crystal, the higher the resonant frequency is generated. For a quartz crystal with the thickness of 0,330 mm the frequency is 5 MHz. Sauerbrey proposed an equation where the frequency change is related to adsorbed mass by an equation so-called *Sauerbrey equation* (equations 8 and 9)(Sauerbrey 1959).

$$\Delta m = \frac{C}{n}\Delta F \qquad (8$$

$$C = \frac{t_q \rho_q}{f_0} \qquad (9$$

Where n and *C* are the overtone and Sauerbrey constant respectively, t_q as the thickness and ρ_q is the density of the Sauerbrey constant. It should be pointed out that this equation is valid under three assumptions: the adsorbed film is rigid, small compared to the mass of quartz crystal, and covers the sensor surface.

Another feature of QCM which makes this tool unique in balancing the adsorbed biomolecules at different surfaces is its ability to plot a dissipation curve which mirrors the viscoelasticity of adsorbed protein layer so-called QCM with dissipation mode (QCM-D)(Dixon 2008). The dissipation parameter is defined as a dimensionless parameter which is representative of the ratio of dissipated energy per oscillatory cycle to stored energy defined as quality factor Q (equation 10).

$$D = \frac{1}{Q} = \frac{E_{Dissipated}}{2\pi E_{Stored}} \qquad (10$$

3.2 Atomic force microscopy (AFM)

One of the potent techniques to record the surface topography of samples along with obtaining the surface characteristics is AFM. This technique as one of the scanning probe microscopic methods was firstly introduced by IBM Scientists in 1986 (Binnig et al. 1986; Seidel 2008). Despite existence of various microscopic techniques, several features are distinguished AFM among the other techniques. These features can be summarized as mapping a high resolution 3D image on the order of nanometer, ability to run in different ambient conditions, and rendering mechanical properties of the sample. Base on the aforementioned capabilities, window of demands to utilize the AFM is becoming wider in various fields of science such as polymer science, surface chemistry and molecular biology has proven it as an efficient method to obtain the material characteristics.

In principle, a setup of various elements is applied to image and extract the desired material characteristic. A sharp tip with curvature of nanometer and positioned at the free end of a cantilever probes the surface and changing height or cantilever deflection is sensed by a *detector* and transferred as an electrical signal. The detector analyzes the reflected laser beam off the cantilever on the *four-quadrant photodetector* as a function of height variation and the angular deflection of cantilever and transfers an electrical signal which leads to imaging a 3D surface topography.

The cantilever functions as a spring with spring constant. Upon reaching to the proximity of the surface, various forces such as mechanical contact force, van der Waals forces, capillary forces, chemical bonding, electrostatic forces, magnetic forces *etc.* deflect the cantilever. The imposed forces on the cantilever can be described by the Hook's Law and as a matter of stiffness, if the

spring constant of the cantilever is less than that of the surface, the deflection is recorded (Cappella and Dietler 1999).

$F = -K.X$ (11

where F is the force, K as spring constant, and X is defined as the cantilever deflection.

In order to keep the imposed force on the cantilever constant, an electronic *feedback loop* is employed. When the distance between the probe and the sample changes, the deflection is taken as input and the output is the adjustment of the height between the sample and probe based on the predefined deflection. In this regard, the feedback look continuously controls and adjust the deflection to keep it constant during the scanning period (JPK).

AFM enables the operator to extract the information in different modes: contact mode, tapping mode, and non-contact mode. By keeping the cantilever close to the surface, the prominent repulsive interactions deflect the cantilever. On the other hand, at long distance between the probe and surface, other long-range interactions such as electrostatic interactions and Van der Waals interactions play key roles to attract the cantilever towards the surface. If the probe is brought close to the surface, the repulsive forces keep the probe away from the surface (which is the common rule in the contact mode). As the distance between the probe-surface increases, the repulsive force is replaced with attractive force and the cantilever bends towards the surface (JPK).

In contact mode of operation, due to the close distance between probe and the surface, repulsive forces keep the probe away from the surface and the force curve (see **figure 3-1**) lies in repulsive region. In order to manifest enough deflection, cantilevers used in this mode have low spring constant. Here, the feedback loop by receiving the signal as a consequence of decrease of

distance, adjusts the imposed force to maintain the probe at a constant position. In another type of operation so-called non-contact mode, the probe is kept away from the surface and the probe does not touch the surface. The cantilever oscillating at its approximate resonance frequency approaches to the surface and recedes from the surface. As a result of changing interactions, the resonance frequency decreases and the feedback loop changes, and as an output of feedback loop, the system maintains the resonance frequency and sample-probe distance at a constant state (Gross et al. 2009). Compared with contact mode, in non-contact mode the surface does not experience any contact of the tip which not only keeps the tip from deforming the surface, but also prevents the tip from contamination which is a proper candidate to image soft films such as biological and polymeric ones. However, in some cases, a fluid layer is formed on the surface of samples which makes the surface scanning difficult. In this regard, approaching the tip close enough to the surface causes the tip to stick to the surface. In order to overcome the aforementioned issue, intermittent contact or tapping mode was introduced (Zhong et al. 1993). The piezo positioned in cantilever holder controls the oscillation of the tip at the free end of the cantilever. The cantilever is driven at a constant frequency and during the scanning, the tip comes into contact with the surface for a short time which makes the technique suitable for soft surfaces such as proteins. During the approaching to and retracting from the surface the force curve is switched from repulsive force to attractive force. Consequently, in this type of operation, the force curve lies between two extremes of the force curve: at the one end the repulsive force and at the other end attractive force. As a result, the change in height of the cantilever is sent as an electric signal in order to keep the amplitude of the oscillation at the pre-adjusted value (Roiter and Minko 2005).

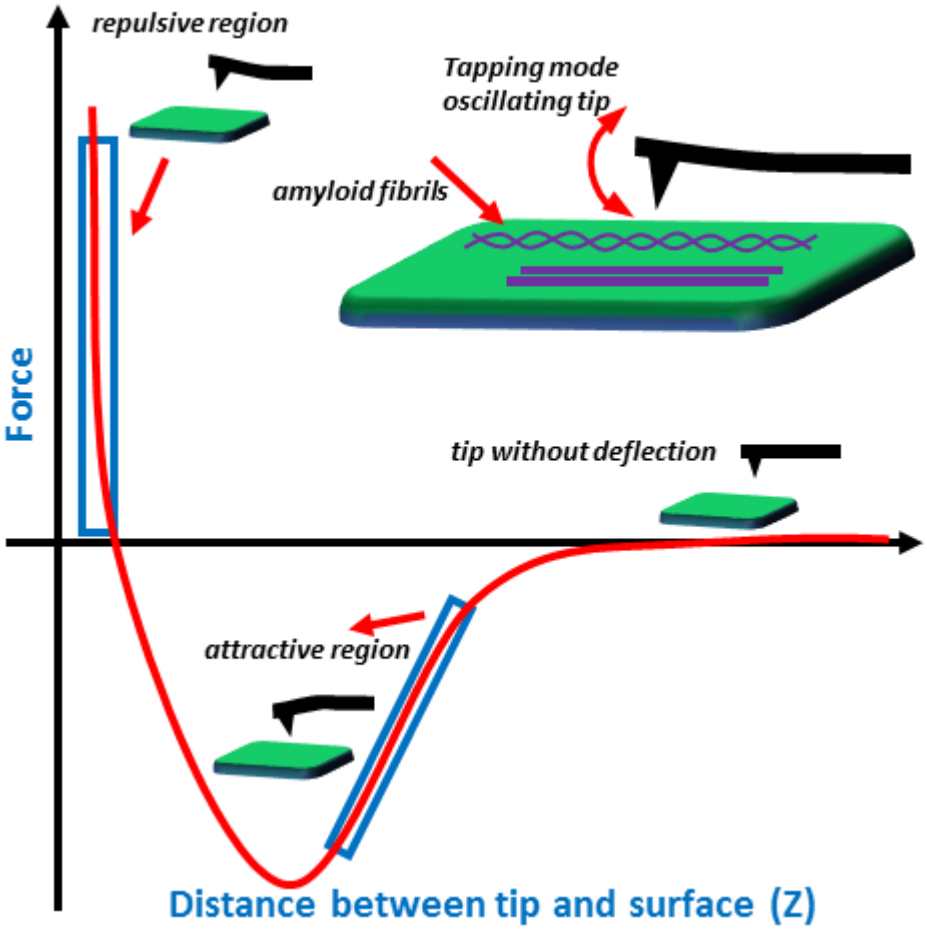

Figure 3-1 *Schematic of force regimes during taking surface topography by AFM*

Chapter 4

Self-Assembly, Dynamics, and Polymorphism of hIAPP(20-29) Aggregates at Solid-Liquid Interfaces

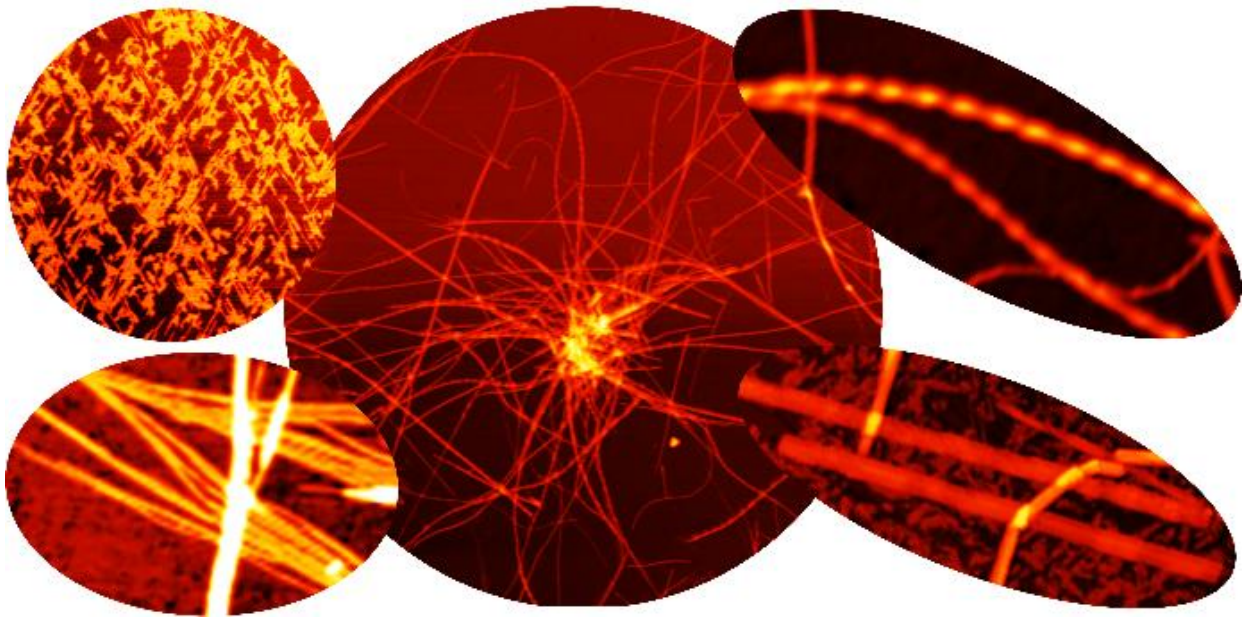

4.1 Introduction

Conversion of proteins and peptides into insoluble amyloid aggregates comprises an important step in the development of numerous degenerative disorders including Alzheimer's disease, Parkinson's disease, Huntington's disease, and type 2 diabetes mellitus (Chiti and Dobson 2006). In the course of type 2 diabetes, amyloid aggregates of a peptide hormone called islet amyloid polypeptide (IAPP) or amylin are deposited in the pancreas. The physiological function of IAPP includes adjustment of glucose metabolism, carbohydrate metabolism, modulation of insulin secretion, inhibition of bone resorption, and prevention of gastric emptying (Cooper et al. 1988). Its different amyloid aggregates, however, are able to damage the membranes of the β-cells in different ways which may lead to long-term β-cell failure (Höppener et al. 2000; Khemtémourian et al. 2008).

Amyloid aggregation occurs in the form of a nucleation process that typically is found to proceed in three distinct stages (Eichner and Radford 2011). In an initial lag phase, thermodynamically disfavored oligomeric nuclei are assembled which then grow rapidly into larger, thermodynamically stable fibrillar aggregates in the so-called elongation phase. This growth proceeds via addition of monomers or smaller oligomers from solution. The final plateau phase represents a saturation regime, in which a variety of morphologically different fibrillar structures may be found. Although their morphology may differ substantially, virtually all amyloid fibrils are characterized by intermolecular β-sheets oriented perpendicular to the fibril axis (Eichner and Radford 2011).

The kinetics of fibrillization and the morphology of the resulting fibrils depend on a large number of environmental factors including, monomer concentration, ionic strength, pH, temperature, and mechanical stress (Pedersen et al. 2010). Similarly, also the presence of a surface may have a strong effect on fibrillization as it may influence local monomer concentrations due to specific or nonspecific adsorption and induce conformational changes in the adsorbed monomers. In this context, the physicochemical surface properties such as hydrophobicity, charge, and surface chemistry play an important role since they directly affect the interaction with the molecule. Consequently, several studies have investigated the interaction of various amyloidogenic peptides and proteins with different model surfaces (Sluzky et al. 1991; Goldsbury et al. 1999; Kowalewski and Holtzman 1999; Zhu et al. 2002; Giacomelli and Norde 2003, 2005; Rocha et al. 2005; Losic et al. 2006; Hovgaard et al. 2007; Linse et al. 2007; Nayak et al. 2008; Rocha et al. 2008; Jeworrek et al. 2009; Cabaleiro-Lago et al. 2010a; Keller et al. 2011a; Wang et al. 2011; Yu et al. 2012a; Lin et al. 2014).

Human IAPP (hIAPP) consists of 37 amino acid residues with the region 8-37 taking part in the formation of intermolecular β-sheets (Cao et al. 2013). It was shown that the hydrophobicity of hydrocarbon (HC) surfaces has a strong influence on surface-catalyzed hIAPP assembly, with increasing hydrophobicity resulting not only in delayed fibrillization but also pronounced changes in aggregate morphology (Keller et al. 2011a). These alterations may be attributed to specific interactions between the different surfaces and the charged and hydrophobic amino acid residues of the peptide, respectively, which result in different conformations of the adsorbed monomer and consequently different assembly pathways.

In order to develop a deeper understanding of the molecular processes that govern surface-catalyzed amyloid aggregation, we here investigate the self-assembly of hIAPP(20-29) at hydrophilic and hydrophobic model surfaces. hIAPP(20-29) is an amyloidogenic core fragment of hIAPP whose aggregates are structurally different from those of full-length hIAPP(1-37) but also show cytotoxicity.(Tenidis et al. 2000) Compared to hIAPP(1-37), hIAPP(20-29) displays different assembly dynamics in solution and also a richer polymorphism of fibrillar species which is in particular characterized by the coexistence of coiled and ribbon-like fibrils (Goldsbury et al. 2000; Sedman et al. 2005; Cabaleiro-Lago et al. 2010b; Zhang et al. 2013). Furthermore, while hIAPP(1-37) has several positively charged and hydrophobic amino acid residues, hIAPP(20-29) features only hydrophobic residues but no charged ones. Therefore, its interaction with charged surfaces is mediated predominantly by the charged termini. Interactions with hydrophobic surfaces, however, will involve four hydrophobic amino acid residues located in the β-sheet forming region (Madine et al. 2008).

Despite these differences, Cabaleiro-Lago *et al*. observed that both peptides interact with copolymeric nanoparticles in a similar way, with increased hydrophobicity resulting in delayed fibrillation (Cabaleiro-Lago et al. 2010b). Apart from this study, however, very little is known about the interaction of hIAPP(20-29) with solid surfaces. In this paper, we thus present a detailed time-lapse atomic force microscopy (AFM) study that compares the self-assembly of hIAPP(20-29) in bulk solution and at different solid-liquid interfaces. Although AFM does not yield any molecular or structural information, it enables the parallel investigation of self-assembly dynamics and aggregate morphology and is therefore frequently used to study amyloid formation both in bulk solution and at surfaces (Kowalewski and Holtzman 1999; Blackley et al. 2000; Zhu et al. 2002;

Green et al. 2004; Hoyer et al. 2004; Goldsbury et al. 2005; Sedman et al. 2005; Dong et al. 2006; Losic et al. 2006; Podestà et al. 2006; Zhang et al. 2006; Hovgaard et al. 2007; Karsai et al. 2007; Manno et al. 2007; Yang et al. 2007; Adamcik et al. 2010; Loksztejn and Dzwolak 2010; Keller et al. 2011a; Wang et al. 2011; Dai et al. 2013; Zhang et al. 2013; Zhou et al. 2013; Lin et al. 2014). We use freshly cleaved mica surfaces and thin HC films as perfectly hydrophilic and hydrophobic model surfaces for amyloid assembly, respectively. The presence of the hydrophilic mica surface is found to promote fibrillization and the assembled hIAPP(20-29) fibrils exhibit a distinctly different polymorphism compared to fibrils formed in bulk solution. Furthermore, we find that fibrillization at the hydrophobic surface is retarded but not completely suppressed, in contrast to previous studies with hIAPP(1-37) where complete inhibition of fibril formation was observed at such hydrophobic surfaces (Keller et al. 2011a).

4.2 Materials & Methods

Synthetic hIAPP(20-29) was purchased from Bachem and mica substrates (grade V1) from Ted Pella. Mica substrates were freshly cleaved directly before use. Hydrophobic HC films with contact angles of about 90° were prepared as previously described by prolonged exposure of ion-beam modified mica surfaces to the laboratory atmosphere (Keller et al. 2011b). In brief, the mica surfaces were irradiated in ultra-high vacuum with low-energy (≤ 500 eV) Xe^+ ions to chemically activate the surfaces, resulting rapid adsorption of a thin HC film upon contact with the laboratory atmosphere. When stored under ambient conditions, continuous HC adsorption from the environment leads to a slow increase of the film thickness and, therefore, to a continuous increase

of the contact angle of the surface (Keller et al. 2011b). To reach a final contact angle of ~ 90° (Hajiraissi et al. 2017), the samples were stored for a period of about three months.

The protocol for hIAPP(20-29) sample preparation was based on previously reported protocols for this peptide (Elgersma et al. 2006; Madine et al. 2008; Cabaleiro-Lago et al. 2010b; Andreasen et al. 2012; Brender et al. 2013; Zhang et al. 2013). One milligram of hIAPP(20-29) was carefully dissolved in 100 µl of dimethyl sulfoxide (DMSO, Sigma-Aldrich), divided into 5 µl aliquots and stored at -20°C. Directly before the experiments, the 5 µl aliquots were diluted in 495 µl of ultrapure water to reach a final concentration of 100 µM and gently mixed. Water was chosen instead of buffer in order to minimize screening of electrostatic interactions and avoid residual salt deposits on the surfaces which may obscure the AFM images. All the samples used in this study were taken from the same stock solution and contained 1 % of residual DMSO. This low amount of DMSO did not result in a different contact angle on the substrate surfaces compared to pure water (Hajiraissi et al. 2017).

For bulk experiments, the 500 µl sample was incubated without agitation in a closed tube at 25°C for 24 h. After different time intervals, aliquots of 5 µl were carefully removed and deposited on freshly cleaved mica substrates. After 5 min of incubation, the samples were gently dried in a stream of ultrapure air.

To study the surface-catalyzed assembly of hIAPP(20-29), aliquots of 20-35 µl volume were directly deposited on the different substrate surfaces. Due to variations in the size of the cut mica substrates, the sample volumes were individually adjusted in order to completely cover the substrate surfaces with solution. The liquid-covered substrates were then incubated in a humidity

chamber (r.h. 95 %) for different times ranging from 20 min to 120 min at 25°C in order to minimize any evaporation-induced effects (Accardo et al. 2015). After incubation, the samples were dried in a stream of ultrapure air as described previously (Keller et al. 2011a). Due to the directionality of the air stream, the exposed boundary of the sample drop was moving towards the corner opposite to the air nozzle, so that possible bulk aggregates were predominantly deposited in this sample corner. AFM imaging, however, was performed in the center of the sample surfaces, thus minimizing the influence of bulk artifacts.

The samples were investigated in the dry state by *ex-situ* AFM because during imaging in liquid, we observed that the interactions between the aggregates and the mica surface are so weak that the aggregates can easily be moved around and even completely desorbed from the surface by the scanning AFM tip (**figure 4-1**). After gently drying the samples, however, the dehydrated aggregates were found to be more firmly attached and remain in place during scanning. Therefore, imaging was performed in air using a JPK Nanowizard II and a JPK Nanowizard III AFM operated in intermittent contact mode and HQ:NSC18/Al BS cantilevers from MikroMasch with a nominal force constant and tip radius of 2.8 N/m and 8 nm, respectively. However, as was reported previously for hIAPP(1-37) and Aβ(1-42) (Maurstad et al. 2009), drying does not induce major changes in fibril morphology.

AFM imaging of hIAPP(20-29) aggregates formed on the freshly cleaved mica surface during 2 h of incubation was also performed in situ under liquid conditions. However, no clear images of fibrils could be obtained, indicating that the interaction of hIAPP(20-29) with the mica surface is so weak that the AFM tip can easily move the aggregates around and even desorb them from the mica

surface. This is particularly obvious in **Figure 4-1** which shows the trace and the retrace image of one of the few regions where fibrillar structures could actually be identified at the surface. Apart from many imaging artifacts that result in tails and streaks oriented in scan direction, there is one fibril in the lower right corner (indicated by the white arrow) that is visible in the trace image but almost completely disappears in the retrace image. This indicates that this fibril was either desorbed or displaced due to interaction with the scanning AFM tip. Furthermore, the height profile taken along the line indicated in the trace image shows fibril heights of only about 0.1 nm which are much lower than the heights obtained in dry imaging (see **table 4-1** and **figure 4-10**), indicating that the fibrils were displaced sideways during each tapping cycle. After drying the sample, however, AFM images comparable to those shown in **Figure 4-6** could be obtained without difficulty, confirming the presence of many fibrils on the mica surface. A similar effect could also be observed for the epitaxially grown sheet-like structures on the mica surface. **Figure 4-2** shows a large-scale AFM image of a smaller region that has previously been scanned twice. The previously scanned region is clearly visible because the repeated scanning led to the desorption of aggregate structures from the surface. The corresponding height profile reveals a height of the adsorbed film of about 2 to 2.5 nm, in agreement with the heights determined by ex-situ AFM (see **table 4-1**).

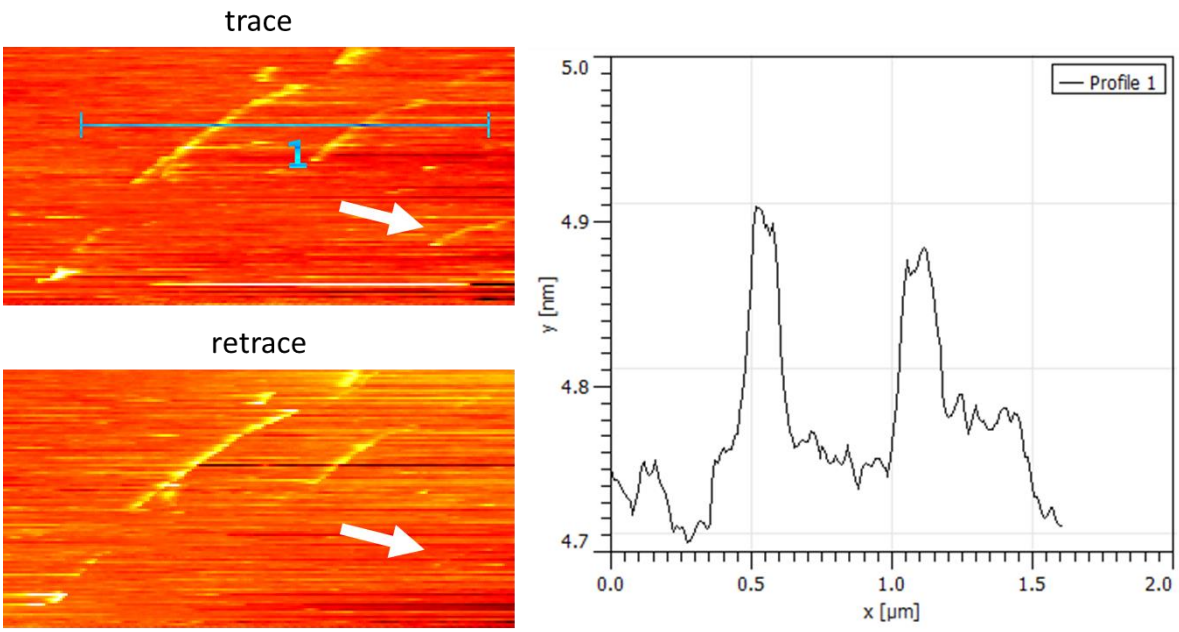

Figure 4-1. *In-situ AFM images (trace and retrace) of hIAPP(20-29) fibrils on a freshly cleaved mica surface. The corresponding height profile was taken along the line indicated in the trace image. AFM images have a size of 2 x 1 µm².*

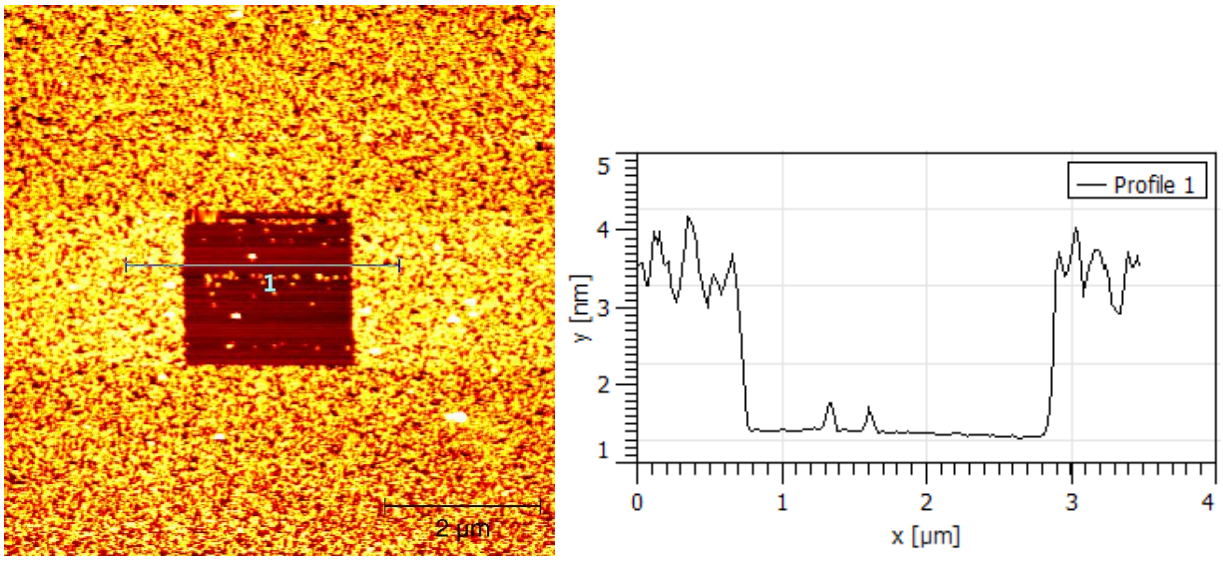

Figure 4-2. In-situ AFM image of epitaxially grown hIAPP(20-29) on a freshly cleaved mica surface showing a previously scanned region in which the AFM tip induced the desorption of the adsorbates. The corresponding height profile was taken along the line indicated in the AFM image.

For the statistical determination of the fibril heights and coiling periodicities summarized in **table 4-1**, between 13 and 1135 structures recorded at different areas of the sample surfaces have been analyzed per experimental condition and aggregate species.

Table 4-1. *Mean dimensions (in nm) of the different hIAPP(20-29) aggregate species formed within the first 2 h of incubation in bulk solution and on mica and HC surfaces, respectively. Errors represent standard deviations.*

Species	bulk	mica	HC
epitaxial sheets (height)	2.5 ± 0.6	2.0 ± 0.8	-
oligomers (height)	-	-	1.6 ± 1.0 after 20 min to 5.5 ± 3.2 after 120 min
linear fibrils (height)	6.7 ± 1.4	8.8 ± 4.8	6.7 ± 2.8
coiled fibrils (height)	6.2 ± 0.7	10.6 ± 4.7	-
coiled fibrils (periodicity)	35.8 ± 7.6	110.9 ± 65.6	-
ribbons (height)	-	8.3 ± 3.6	-

Only height values and lateral periodicities are reported in this work and no absolute lateral dimensions because the latter cannot be measured accurately due to the finite size of the AFM tip (Murray et al. 1993; Paige et al. 1998). Heights were measured with respect to the underlying, adsorbate-free surface. In the case of coiled fibrils, maximum heights are reported that correspond to the local maxima of the periodic height modulation along the fibril axis. Due to the

occurrence of rapid epitaxial growth on the freshly cleaved mica surface, careful inspection of both fibril morphology and substrate topography was required to avoid confusion of straight fibrils that just followed the topographic modulation of the underlying substrate with coiled fibrils that exhibited an intrinsic height modulation as a result of protofibril coiling. Similarly, for high fibril coverage, only those regions of the individual fibrils were analyzed that were clearly not overlapping with other fibrils. In addition, care was taken not to count fibrils twice. Image analysis was performed using Gwyddion open source software (Nečas and Klapetek 2012).

4.3 Results & Discussion

4.3.1 Self-assembly of hIAPP(20-29) in bulk solution

Figure 4-3 depicts AFM images of hIAPP(20-29) incubated for different times in bulk solution. After 30 min of bulk incubation (**figure 4-3 a,b**), sheet-like structures are observed all over the mica surface. These sheet-like structures have a mean height of 2-3 nm (**figure 4-3 i**) and are aligned along two prominent directions that enclose an angle of roughly 60°, coinciding with the pseudo-hexagonal symmetry of the single-crystalline mica surface (Franzini 1969). Therefore, these structures are probably assembled at the mica surface from non-aggregated monomers during the 5 min of incubation at the surface. Such epitaxial growth on mica surfaces has previously been observed for a number of amyloidogenic peptides and proteins including α-synuclein, Aβ(25-35), insulin and the short model peptide GAV-9 (Hoyer et al. 2004; Zhang et al. 2006; Karsai et al. 2007; Zhou et al. 2013). For Aβ(25-35), it was shown that acetylation of lysine resulted in the suppression of epitaxial growth, while acetylation of the N terminus only had little effect (Karsai et al. 2007). Therefore, epitaxial growth was attributed to the interaction of positively charged lysine

residues with the negatively charged mica surface. Also in the case of α-synuclein, epitaxial growth was explained as resulting from lysine-surface interactions (Hoyer et al. 2004). Since GAV-9 does not exhibit any charged residues, however, epitaxial growth of this peptide probably proceeds via electrostatic interactions between its positively charged N terminus and the mica surface (Zhang et al. 2006). Similar to GAV-9, hIAPP(20-29) also has no charged residues which thus hints at a similar assembly mechanism. Interestingly, no epitaxial growth is observed for full-length hIAPP(1-37) under the same experimental conditions, even though it exhibits a lysine residue at the N terminus (see **figure 4-4**).

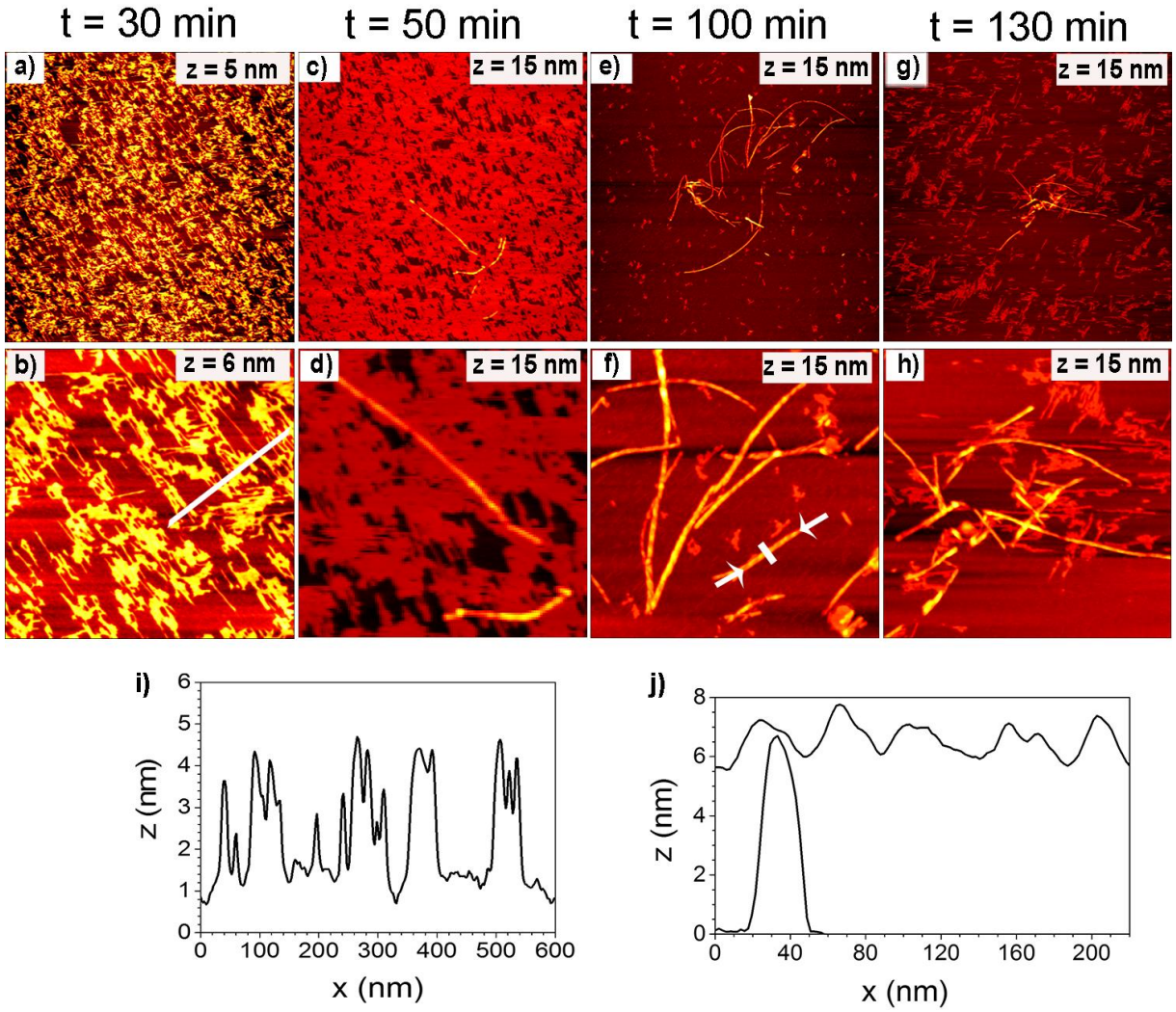

Figure 4-3. *AFM images of hIAPP(20-29) incubated in bulk for t = 30 min (a,b), 50 min (c,d), 100 min (e,f), and 130 min (g,h). Images in the upper and lower row have a size of 4 x 4 µm² and 1.5 x 1.5 µm², respectively. The ranges of the z-scales are given in the individual images. Panel (i) shows a height profile taken along the white line in image (b). Panel (j) shows height profiles taken along the white (lower curve) and between the white arrows (upper curve) in image (f).*

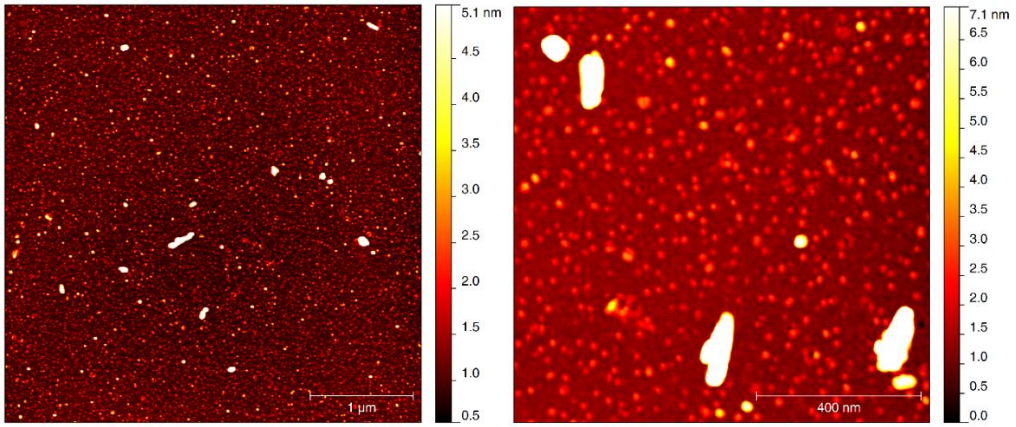

Figure 4-4. *AFM images of 100 µM IAPP(1-37) after 5 min of incubation on a freshly cleaved mica surface.*

Apart from the epitaxially grown sheet-like structures, no other aggregates are observed after 30 min of bulk incubation. Only after 50 min of incubation, a few first fibrils appear (**figure 4-3 c,d**). These fibrils have a height of 6 to 7 nm and do not show any distinguishable periodicity along the fibril axis that stems from the coiling of protofibrils around each other. In the following, this fibril species will thus be referred to as straight fibrils. Although these straight fibrils are present at the surface up to at least 130 min of incubation, a second fibrillar species appears after incubation for 100 min (**figure 4-3 e,f**) which does exhibit a clearly distinguishable periodicity of about 38 nm and has a similar height as the straight fibrils (height profiles in **figure 4-3 j**). The fact that both fibrillar species have almost identical heights is quite surprising since it has been shown for a variety of amyloidogenic proteins and peptides, including hIAPP(1-37),(Goldsbury et al. 1999; Keller et al. 2011a) that coiled fibrils represent mature higher-order fibrils that form due to the association of straight protofibrils. Consequently, in AFM, mature fibrils are typically observed to be at least twice as high as protofibrils (Goldsbury et al. 1999; Keller et al. 2011a). The fact that this is not the

case in the present experiments therefore suggests that the coiled and the straight fibrils represent two fibrillar species that form independently.

Up to 130 min of incubation, the numbers of both fibril species increase slightly with incubation time while their dimensions remain unaltered. However, fibrils remain rather scarce even after 130 min of incubation. Prolonging the incubation time to 24 h also does not result in more fibrils, but rather in drastically increased fibril lengths and heights as can be seen in **Figures 4-5**. After this time, the observed fibrils have lengths of several microns and heights ranging from 10 to 100 nm. **Figure 4-5** furthermore reveals that these large fibrils are composed of smaller fibrils that laterally associate with each other. Although most of the large fibrils are of straight morphology, some of them have a ribbon-like shape with a flat and almost rectangular cross section.

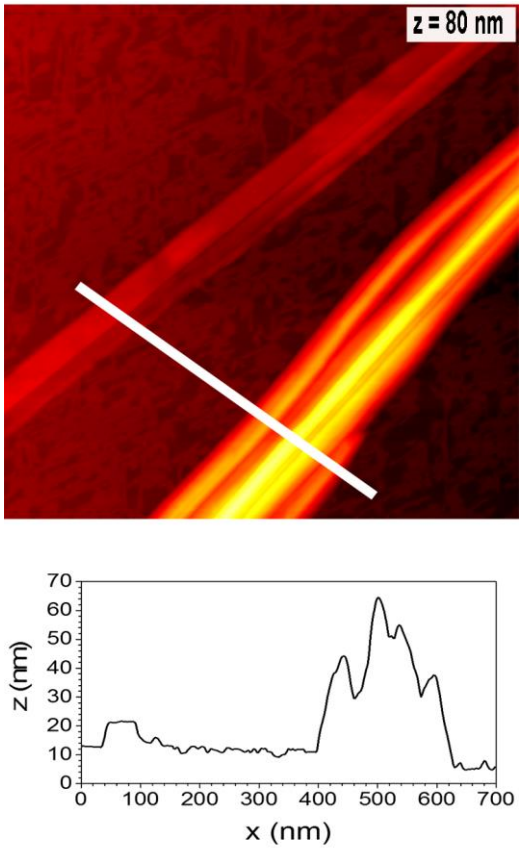

Figure 4-5. *AFM image of hIAPP(20-29) fibrils after 24 h incubation in bulk with a corresponding height profile taken along the white line.. The image size is 1 x 1 µm².*

Sedman *et al*. investigated the morphology of hIAPP(20-29) fibrils assembled in bulk solution by AFM (Sedman et al. 2005). They found that at short incubation times, the formed fibrils had a periodic or coiled morphology while at long incubation times, only straight fibrils were observed. In contrast, we observe in above experiments the coexistence of straight and coiled fibrils, with straight fibrils appearing before coiled ones. In addition, the straight fibrils observed by Sedman *et al.* had heights of 4–5 nm which is slightly lower than in our experiments. Similarly, the coiled fibrils observed by Sedman *et al.* had a periodicity of about 75 nm while the ones found in our experiments have an average periodicity of only about 38 nm.

Zhang *et al.* observed the coexistence of coiled and ribbon-like fibrils of hIAPP(20-29) assembled in bulk solution by AFM (Zhang et al. 2013). In contrast to our results, however, they found that those ribbons represent the first fibrillar species formed in solution with their height increasing with incubation time from about 4 to about 7 nm. Coiled fibrils appeared only after several hours of incubation while straight fibrils as in our experiments were not observed at all. Furthermore, the authors found three different species of coiled fibrils with different heights ranging from about 15 to about 30 nm but constant periodicities of about 200 nm. Comparison with the dimensions stated above and summarized in **table 4-1** reveals that the fibrils observed in our experiments clearly belong to different species. All these differences show how strongly fibrillation dynamics and fibril morphology are affected by environmental conditions such as buffer composition and initial monomer concentration, which both differed in the mentioned studies and our experiments.

4.3.2 Self-assembly of hIAPP(20-29) at hydrophilic mica surfaces

AFM images of hIAPP(20-29) incubated for different times at hydrophilic mica surfaces are shown in **Figure 4-6**. Again, epitaxial growth of sheet-like structures is apparent all over the mica surfaces. However, already after 20 min of incubation, few fibrillar structures are observed whose density and lengths increase drastically with incubation time (**figure 4-6**). A closer inspection of the fibrils reveals that these fibrils also have a slight tendency to align along the crystallographic directions of the mica surface (see in particular (**figure 4-6 c,e**). However, the degree of orientation is much lower for the fibrils than for the epitaxially grown sheets. This effect is not visible in the AFM

images of **figure 4-3**, where the fibrils did not assemble at the surface but were deposited from bulk solution.

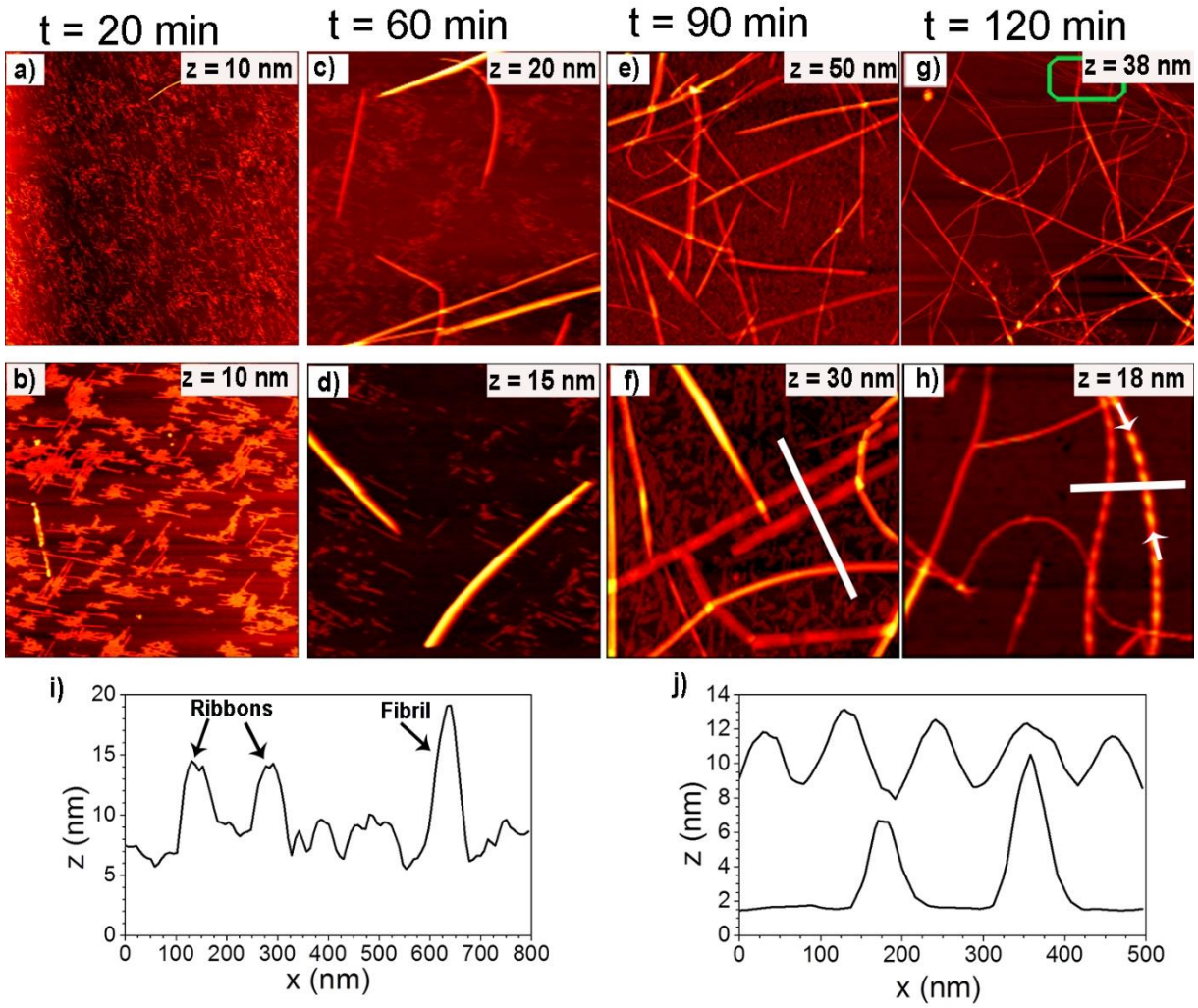

Figure 4-6. *AFM images of hIAPP(20-29) incubated on freshly cleaved mica surfaces for t = 20 min (a,b), 60 min (c,d), 90 min (e,f), and 120 min (g,h). Images in the upper and lower row have a size of 4 x 4 µm² and 1.5 x 1.5 µm², respectively. The ranges of the z-scales are given in the individual images. Panel (i) shows a height profile taken along the white line in image (f). Panel (j) shows height profiles taken along the white (lower curve) and between the white arrows (upper curve) in image (h).*

From a morphological point of view, three different fibril species can be distinguished. At low incubation times, only straight fibrils are found which have an average height around 10 nm (see **figure 4-6 i**). In addition to their larger height, these straight fibrils also appear in general less curved than the ones assembled in bulk solution (see **figure 4-3**). This might be a result of adsorption-induced bending of the preassembled fibrils or stem from the surface-assisted assembly along certain crystallographic directions. The first coiled fibrils appear after an incubation time of 60 min and have similar heights as the straight fibrils and an average periodicity of about 110 nm (**figure 4-6 j**). After 90 min of incubation, a third fibril species with a ribbon-like morphology similar to the ones observed in bulk assembly after 24 h incubation appears with a height of again about 10 nm (**figure 4-6 f,i**). All three fibrillar species persist up to the longest incubation time of 120 min with their dimensions remaining constant.

The relative occurrence of each fibrillar species as a function of time is shown in **figure 4-7**. Clearly, straight fibrils are the dominating species at all incubation times. When the first coiled fibrils appear after 60 min of incubation, the fraction of straight fibrils drops to about 70 %. The additional appearance of ribbons at 90 and 120 min leads to a further drop to about 50 % straight fibrils. Interestingly, once ribbons and coiled fibrils appear, their relative occurrence remains more or less constant. This indicates that all three fibrillar species, in spite of their different lag times, have similar assembly rates.

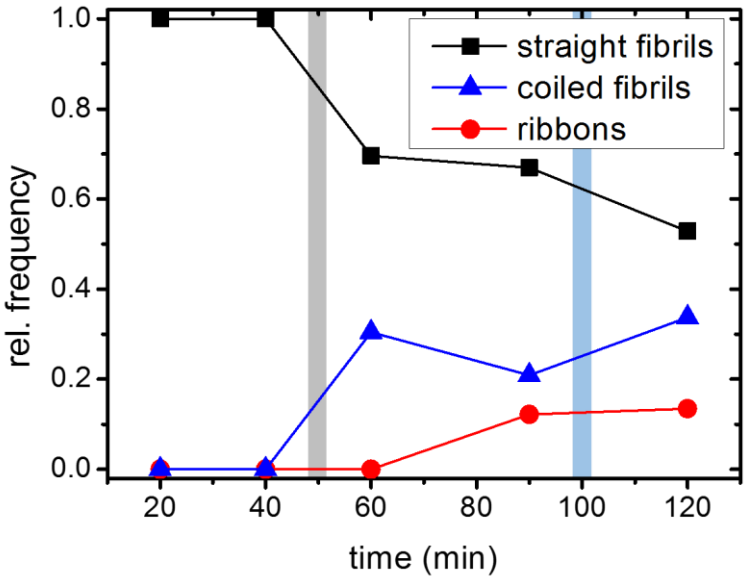

Figure 4-7. *Relative occurrence of the different fibrillar species at the mica surface as a function of incubation time. The grey and light blue region marks the first observation of straight and coiled fibrils after bulk incubation, respectively.*

Compared to assembly in bulk solution, both straight and coiled fibrils appear much earlier in the presence of the hydrophilic mica surface (see **figure 4-6**). This accelerated fibrillization may be attributed to the rapid adsorption and preferential orientation of the monomers on the negatively charge mica surface. Since adsorption is mediated predominantly by the positively charged N terminus and does not involve any residues, the adsorbed monomers are locally confined at the surface yet maintain a large degree of conformational freedom and, as indicated by *in-situ* AFM imaging (see **figure 4-1**), some degree of lateral mobility. Therefore, they can easily rearrange and adopt a conformation that favors intermolecular β-sheet formation as exemplified by the epitaxial growth of sheet-like structures. So formed initial seeds may then grow, depending on their molecular structure, into different fibrillar species.

In the physiological environment, the most relevant interfaces for hIAPP aggregation are cell membranes which have been proposed to catalyze hIAPP aggregation (Knight and Miranker 2004). Several studies have pointed out that this catalytic effect depends crucially on the lipid composition (Knight and Miranker 2004; Jayasinghe and Langen 2005; Caillon et al. 2013). Especially the presence of anionic lipid membranes was found to drastically decrease the lag time of hIAPP(1-37) aggregation from hours to minutes. These observations seem to agree with our results that show that the negatively charged mica surface promotes aggregation of hIAPP(20-29). This is particularly interesting because although the interactions of the peptide monomers with both interfaces are controlled by electrostatics, there are pronounced differences in interaction at the molecular level. hIAPP(1-37) is interacting with anionic membranes via insertion of its N-terminal region which carries a number of positively charged amino acids residues and thus displays a strong preference for negatively charged lipids (Knight and Miranker 2004; Jayasinghe and Langen 2005; Engel et al. 2006; Apostolidou et al. 2008). hIAPP(20-29), however, does not exhibit any charged residues. Consequently, it was observed that although hIAPP(20-29) also inserts into lipid membranes, it exhibits lower binding affinity and no preference for anionic lipids (Engel et al. 2006). At first glance, this observation seems at variance with our results for mica surfaces. However, when interacting with the solid mica surface, hIAPP(20-29) remains loosely attached to the surface via its N terminus while the rest of the peptide remains in native, unfolded conformation. Therefore, this situation is actually more similar to the case of hIAPP(1-37) at anionic lipid membranes, where the N-terminal residues are inserted into the membrane while the C-terminal residues remain largely unstructured and may promote the formation of intermolecular β-sheets (Apostolidou et al. 2008).

4.3.3 Self-assembly of hIAPP(20-29) at hydrophobic HC surfaces

For hIAPP(1-37), it was shown that the hydrophobicity of the surface has a strong effect on the assembly dynamics and the morphology of the resulting amyloid species (Keller et al. 2011a). In order to evaluate whether this is also the case for hIAPP(20-29), another set of experiments has been carried out using thin HC films grown on ion-beam modified mica substrates as model surfaces. In contrast to freshly-cleaved mica surfaces which have a contact angle close to 0°, the HC surfaces used in this study were perfectly hydrophobic with contact angles of about 90° (Keller et al. 2011b).

Figure 4-8 shows AFM images of HC surfaces after incubation with hIAPP(20-29) for varying times. As can be seen in **Figure 4-8 a,b**, after 20 min of incubation, particle-like oligomeric structures along with some short fibrils appear on the HC surface. Due to the amorphous nature of the HC films, no influence of the crystallographic structure of the underlying mica surface on the amyloid aggregates is observed. The formed short fibrils grow with incubation time and maintain their straight morphology, *i.e.*, no development of a periodic height modulation along or lateral growth perpendicular to the fibril axis can be observed. The growth rate, however, is much lower than on the mica surface and also the fibril density remains very low (see **figure 4-6 g,h**). In addition, strong deposition of amorphous aggregates is observed at longer incubation times (**figure 4-8 c-f**). The straight fibrils have constant heights ranging from about 3 to about 10 nm (**figure 4-8 g**) with a mean value of about 7 nm that is close to the height of the straight fibrils assembled in bulk solution (see **table 4-1**). In contrast to the fibril height, the height of the oligomeric aggregates is

found to slightly increase with incubation time from about 1.6 nm at 20 min incubation to about 5.5 nm at 120 min (see **figure 4-8 g,h**).

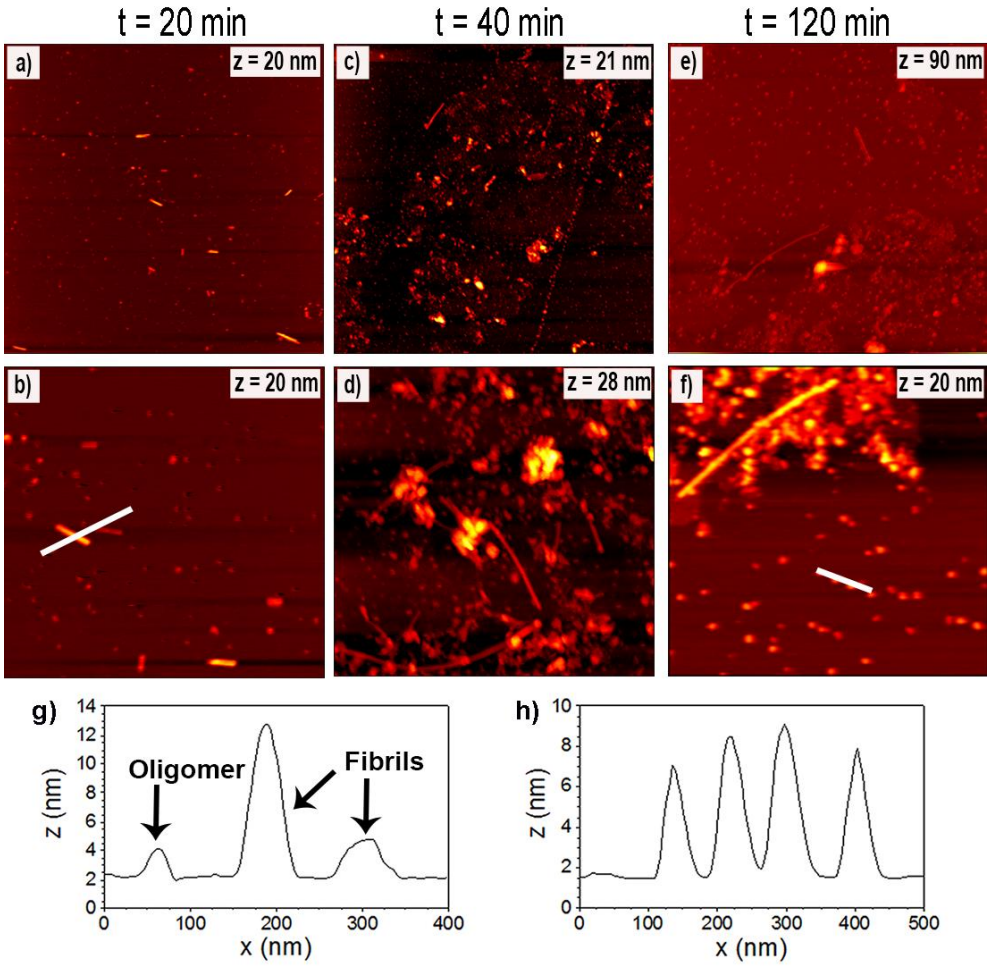

Figure 4-8. *AFM images of hIAPP(20-29) incubated on HC surfaces for t = 20 min (a,b), 40 min (c,d), and 120 min (e,f). Images in the upper and lower row have a size of 4 x 4 µm² and 1.5 x 1.5 µm², respectively. The ranges of the z-scales are given in the individual images. Panels (g) and (h) show height profiles taken along the white lines in images (b) and (f), respectively.*

When in a previous study full-length hIAPP(1-37) (13 µM in pure water) was incubated on such HC surfaces with contact angles ranging from about 20° to about 90°, a similar effect on fibrillization

dynamics was observed (Keller et al. 2011a). Increasing the hydrophobicity of the surface resulted in a continuous delay of fibrillization as found here for hIAPP(20-29), as well as in an increase in the number of oligomeric species and amorphous aggregates at the surface. In the present experiments, retarded fibrillization may also be responsible for the fact that neither coiled nor ribbon-like fibrils are formed at the surface. Such fibrillar species might appear only after much longer incubation times at such hydrophobic surfaces.

However, there are also some distinct differences between the two peptides:(Keller et al. 2011a) i) For hIAPP(20-29) at the HC surface with 90° contact angle, fibrillar and oligomeric species coexist. In the case of hIAPP(1-37), such coexistence was observed only for lower contact angles ≤ 76° while at 90° contact angle, the surface was crowded with oligomers and fibrillization was completely suppressed. ii) Amorphous aggregation of similar extent as found here was observed for hIAPP(1-37) only at intermediate contact angles around 60°. iii) Increasing the hydrophobicity of the surface not only retarded hIAPP(1-37) fibrillization but also resulted in significantly altered fibril morphology. In particular, the height of the assembled protofibrils decreased from about 2 nm to about 1 nm. Consequently, also the diameter of the mature coiled fibrils decreased from about 4.5 nm to about 1.8 nm. For the straight hIAPP(20-29) fibrils in above experiments, only a rather small decrease in height (from about 9 nm to about 7 nm) has been observed on the HC surface.

Above observations reveal a more robust pathway of surface-catalyzed hIAPP(20-29) fibrillization that is less dependent on the physicochemical surface properties than is the case for hIAPP(1-37) under the respective experimental conditions. This is consistent with the fact that the interaction

of hIAPP(20-29) with hydrophobic surfaces is governed by only four hydrophobic residues while hIAPP(1-37) has additional hydrophobic residues in its N-terminal and C-terminal regions. Furthermore, it is believed that aggregated hIAPP(1-37) monomers have a U-shaped conformation with a bend in region 18-22 (Cao et al. 2013). The monomers in hIAPP(20-29) fibrils, on the other hand, are arranged in a straight conformation (Madine et al. 2008). Therefore, intermolecular β-sheet formation should be less sensitive toward hydrophobic surface interactions for hIAPP(20-29) than for hIAPP(1-37).

4.3.4 Polymorphism of hIAPP(20-29) fibrils: bulk vs. surface

Figure 4-9 a compares the heights of the different fibrillar species observed in bulk and at the mica and HC surfaces within the first 2 h of incubation. Obviously, the straight and coiled fibrils assembled in bulk, and the straight fibrils assembled at the hydrophobic HC surface have very similar heights around 6.5 nm, while the straight, coiled, and ribbon-like fibrils are in general a few nm higher with 8.5 to 10.5 nm. These morphological differences are reflected even stronger in the periodicity of the coiled fibrils (see **figure 4-9 b**). When assembled in bulk solution, these fibrils have an average periodicity of 38 nm, while the coiled fibrils assembled at the mica surface have one of 110 nm. This strong increase in periodicity clearly proves that the coiled fibrils assembled in bulk and at the mica surface belong to different species. Therefore, it can be concluded that the presence of a negatively charged surface does not only promote fibrillization of hIAPP(20-29) but also leads to the assembly of different fibril species.

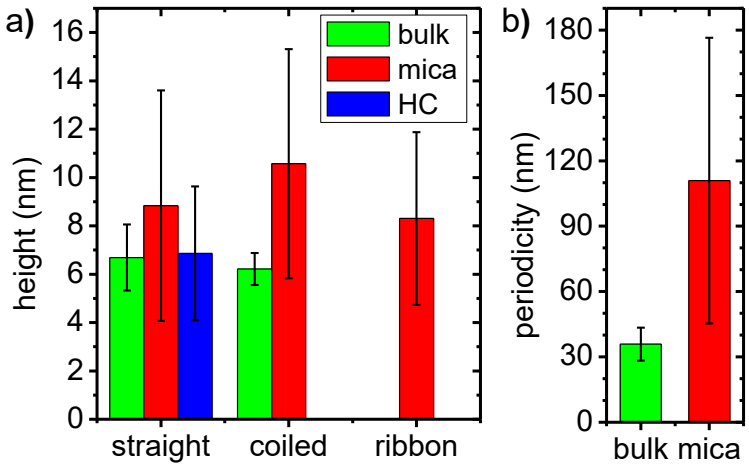

Figure 4-9. *Comparison of the heights of the different fibrillar species (a) and the periodicities of the coiled fibrils (b) assembled in bulk solution and at the different surfaces within the first 2 h of incubation. Error bars represent the standard deviations of the measured distributions.*

Comparing not only the mean values of the dimensions but also the standard deviations (represented as error bars in **figure 4-9**), it becomes clear that assembly at both mica and HC surfaces also leads to more variations in the fibril dimensions than in bulk. This is particularly obvious for the mica surface, where standard deviations of the order of 50 % of the mean are observed. The corresponding height distributions of all three fibrillar species shown in **Figure 4-10** are surprisingly broad and do not exhibit any clearly distinguishable secondary peaks. Therefore, all three fibrillar species actually include a variety of morphologically different fibrils which probably form by lateral association of arbitrary numbers of much smaller protofibrils. Since protofibrils typically are of straight morphology, we assume that the populations of straight fibrils with the lowest heights in **Figure 4-10 a** actually represent or at least include the protofibrils that compose the three higher-order fibrillar species.

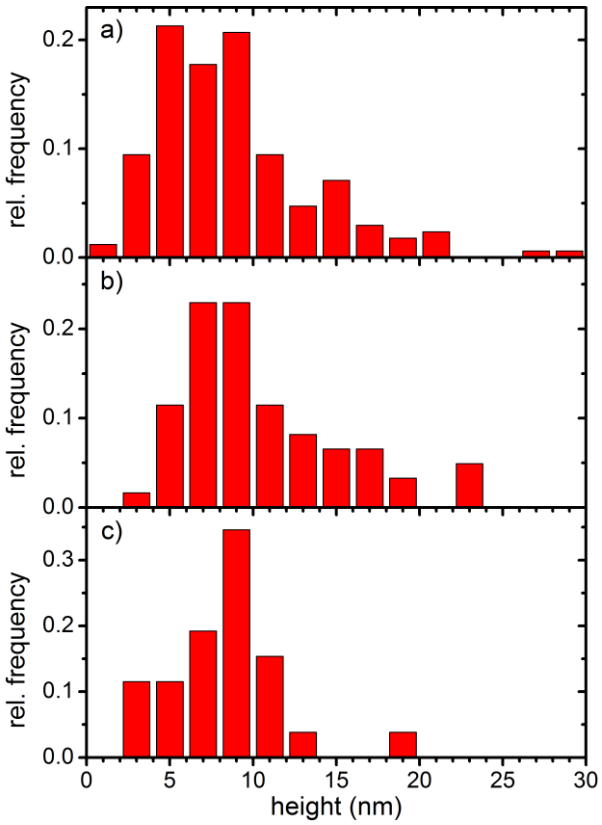

Figure 4-10. *Height distributions of straight (a), coiled (b), and ribbon-like fibrils (c) assembled at the hydrophilic mica surface.*

Morphological evidence in support of this interpretation can be found in **Figure 4-11** which depicts a magnified AFM image of the region indicated in **Figure 4-6 g**. In this image, fibrils with heights of about 2 nm align laterally with each other to form loosely connected, discontinuous ribbon-like structures of the same height. This image may thus show the initial formation of ribbon-like fibrils from those low-height protofibrils. Furthermore, the height of about 2 nm falls well in the range of the two low-nm populations of the height distribution of the straight fibrils shown in **Figure 4-10 a**. Therefore, we propose that all three fibrillar species actually consist of these protofibrils with height of around 2 nm. The protofibrils obviously have a strong tendency to associate with each

other and thereby form a multitude of higher-order fibrils of different morphologies which can turn out to be straight, coiled, or ribbon-like.

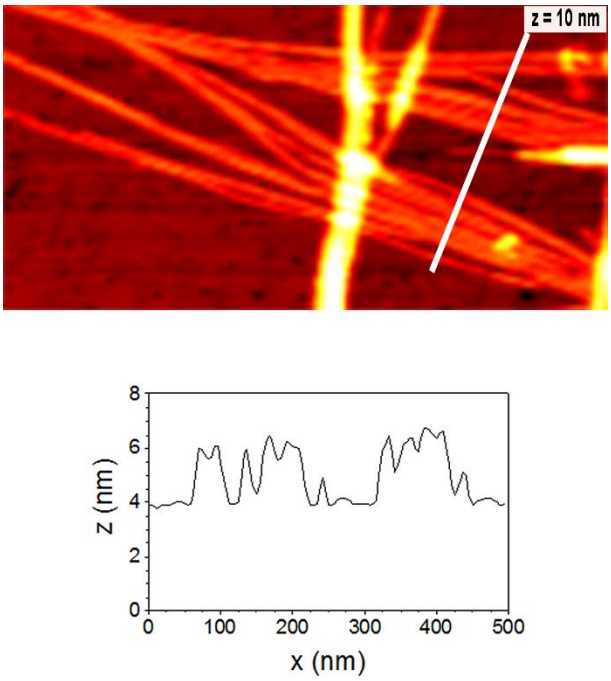

Figure 4-11. *Magnified AFM image of the region indicated in* ***Figure 4-6 g*** *with corresponding height profile taken along the white line. The image size is 1.0 x 0.5 µm².*

4.4 Conclusion

In summary, we have investigated the self-assembly of a fragment of human islet amyloid polypeptide, hIAPP(20-29), in bulk solution as well as at two different solid-liquid interfaces, *i.e.*, hydrophilic mica and hydrophobic HC surfaces. Rapid epitaxial growth of sheet-like hIAPP(20-29) structures is observed within the first few minutes of incubation on the mica surface. Since hIAPP(20-29) does not exhibit any charged residues, epitaxial growth probably results from the interaction of the positively charged N terminus with the negatively charged mica surface.

For assembly in bulk solution, low numbers of straight and coiled fibrils of similar heights of about 6.5 nm were observed for incubation times ranging from 50 to 130 min. The presence of the mica surface, however, was found to promote fibrillization and induce a more pronounced polymorphism in the assembled fibrils. Three different fibrillar species were found to coexist on the mica surface, *i.e.*, straight, coiled, and ribbon-like fibrils. Although those fibrillar species have distinctively different morphologies, their height distributions are very similar and characterized by global maxima between 8.5 and 10.5 nm, and comparatively large widths. This indicates that these fibrillar species form independently from each other by lateral association of arbitrary numbers of smaller protofibrils. These protofibrils are most likely represented by a subspecies of the straight fibrils with a height of about 2 nm.

Incubation of hIAPP(20-29) under identical conditions but in contact with a hydrophobic HC surface resulted in delayed fibrillization and stronger formation of oligomeric structures and amorphous aggregates, similar to previous observations for hIAPP(1-37)(Keller et al. 2011a). However, also distinct differences are observed, namely the coexistence of fibrils and oligomers on a fully hydrophobic surface with a contact angle of about 90°, and that fibrils assembled at the hydrophobic surface have only slightly smaller heights as for the mica surfaces.

These results further stress the importance of the physicochemical surface properties in surface-catalyzed amyloid assembly and show that peptide-surface interactions may induce diverse, peptide-specific alterations not only of amyloid aggregation dynamics but also of fibril morphology and polymorphism. In particular, due to the similarities with hIAPP(20-29) adsorbed on mica surfaces, one might speculate that the presence of anionic lipid membranes could induce the

formation of different fibrillar species during hIAPP(1-37) aggregation. Since a correlation between fibril morphology and amyloid cytotoxicity has previously been suggested,(Seilheimer et al. 1997; Petkova et al. 2005; Yoshiike et al. 2007) this may further imply that the presence of surfaces and membranes cannot only inhibit or promote amyloid aggregation but possibly also modulate the physiological effects of the resulting aggregates. Our results may thus contribute to a deeper understanding of the molecular processes involved in amyloid assembly and toxicity.

Chapter 5

Adsorption and fibrillization of islet amyloid polypeptide at self-assembled monolayers studied by QCM-D and AFM

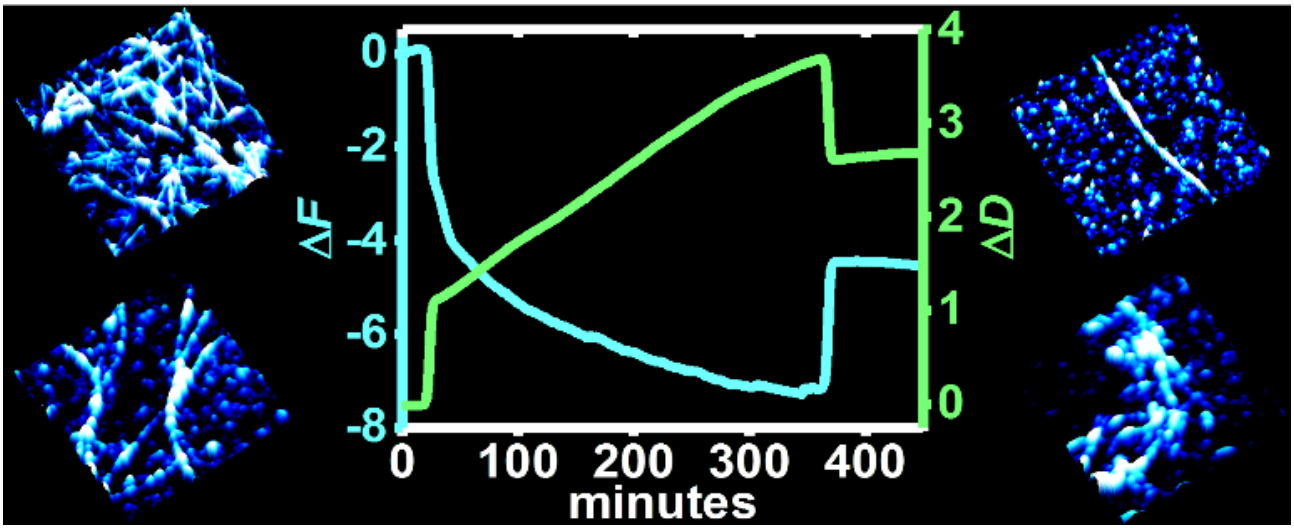

5.1 Introduction

The self-assembly of macromolecules into well-defined one-, two-, and three dimensional structures is a ubiquitous phenomenon in nature and technology(Whitesides and Grzybowski 2002). In biological systems, biomolecular self-assembly is of tremendous importance for cellular functions, *e.g.,* in the formation and dynamics of the cytoskeleton (Pollard and Borisy 2003), the cell membrane (Zimmerberg and Kozlov 2006), and the extracellular matrix (Aumailley and Gayraud 1998). On the other hand, self-assembly of proteins and peptides into insoluble amyloid aggregates plays a crucial role in the development of various diseases such as Alzheimer's disease, Parkinson's disease, and type 2 diabetes mellitus (Knowles et al. 2014). For instance, in > 95 % of type 2 diabetes patients, a decline in insulin-producing β-cells is observed, which correlates with the build-up of amyloid deposits in the islets of Langerhans (Westermark et al. 2011). These deposits are composed of a 37-residue hormone called human islet amyloid polypeptide (hIAPP, **figure 5-1**) which is produced in the β-cells and co-secreted with insulin. While it is well established that prefibrillar oligomeric structures are the primary trigger of β-cell dysfunction, also the growth of amyloid fibrils on the cell membrane can lead to membrane rupture and subsequent cell death (Mirzabekov et al. 1996; Kayed et al. 2004; Engel et al. 2008; Milanesi et al. 2012). Consequently, the interaction of hIAPP with lipid bilayers and various model surfaces has become a field of intense study (Mirzabekov et al. 1996; Goldsbury et al. 1999; Kayed et al. 2004; Knight and Miranker 2004; Jayasinghe and Langen 2005; Engel et al. 2006; Knight et al. 2006; Lopes et al. 2007; Apostolidou et al. 2008; Engel et al. 2008; Nayak et al. 2008; Evers et al. 2009; Jeworrek et al. 2009; Nanga et al. 2009; Cabaleiro-Lago et al. 2010b; Keller et al. 2011a; Liu et al. 2012; Milanesi et al. 2012; Yu et al. 2012b; Caillon et al. 2013; Hajiraissi et al. 2017).

Virtually all amyloid fibrils are composed of β-pleated sheets oriented orthogonal to the fibril axis but may display profoundly different morphologies (Kreplak and Aebi 2006; Pedersen et al. 2010; Eichner and Radford 2011). In hIAPP, three potential β-strand regions have been identified as the fibrillogenic centers, *i.e.,* regions 12-17, 23-27, and 32-37, with each region having different contributions to fibril assembly (Jaikaran et al. 2001b; Scrocchi et al. 2003; Abedini and Raleigh 2005; Koo and Miranker 2005; Gilead and Gazit 2008; Pillay and Govender 2013). Interestingly, the rat variant of IAPP (rIAPP), which has 84 % amino acid sequence analogy to hIAPP (rIAPP **figure 5-1**), exhibits no fibrillogenic properties and no membrane toxicity (Westermark et al. 1990; Green et al. 2003). This behavior has been ascribed to the presence of three proline residues in region 20-29 that inhibit β-sheet formation (Westermark et al. 1990). However, it was shown that also other residues may modulate or induce fibrillization of rIAPP(Green et al. 2003).

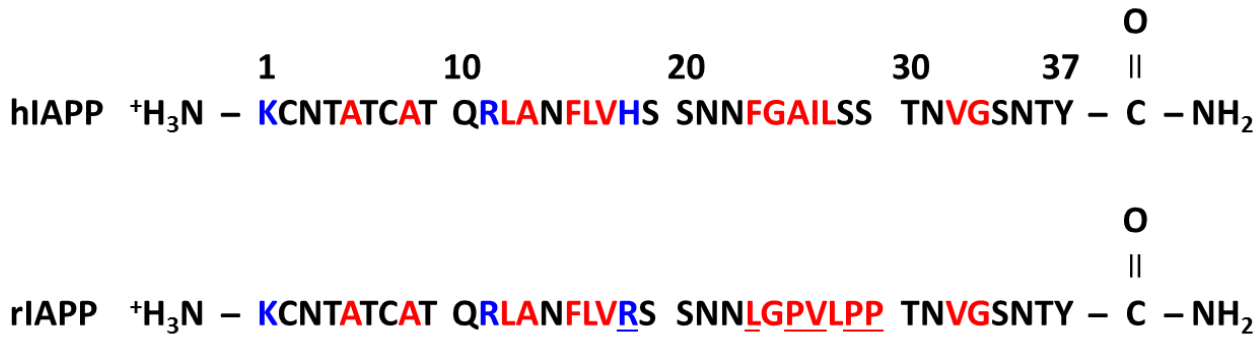

Figure 5.1. *Sequences of hIAPP and rIAPP. Positively charged and hydrophobic residues are indicated in blue and red, respectively. rIAPP residues that differ from the hIAPP sequence are underlined. Note that native IAPP features an amidated C terminus.*

A few previous studies have addressed the effect of physicochemical surface properties such as charge and hydrophobicity on the adsorption and aggregation of hIAPP and some of its fragments

at various model surfaces including negatively charged mica (Hajiraissi et al. 2017), hydrocarbon films of varying hydrophobicity (Keller et al. 2011a; Hajiraissi et al. 2017), lipid bilayers (Knight and Miranker 2004; Jayasinghe and Langen 2005; Lopes et al. 2007; Caillon et al. 2013), and hydrophilic and hydrophobic polymer surfaces (Jeworrek et al. 2009; Cabaleiro-Lago et al. 2010b). In these studies, some general features of hIAPP aggregation could be established. In particular, it was shown that fibrillization is accelerated at strongly negatively charged surfaces (Knight and Miranker 2004; Jayasinghe and Langen 2005; Caillon et al. 2013; Hajiraissi et al. 2017), whereas hydrophobic surfaces tend to retard or even completely suppress fibrillization (Lopes et al. 2007; Cabaleiro-Lago et al. 2010b; Keller et al. 2011a; Hajiraissi et al. 2017). For hydrophobic copolymeric nanoparticles, however, it was found that their potential to inhibit hIAPP aggregation decreased with increasing hydrophobicity (Cabaleiro-Lago et al. 2010b). On the other hand, Jeworrek *et al.* observed that hydrophobic polymer surfaces adsorbed the largest amount of hIAPP while adsorption to positively and negatively charged polymer surfaces was significantly reduced (Jeworrek et al. 2009). In addition, some studies indicate that the presence of surfaces may affect not only adsorption and aggregation dynamics but also the morphology of the assembled hIAPP aggregates (Goldsbury et al. 1999; Keller et al. 2011a; Yu et al. 2012b; Hajiraissi et al. 2017).

In this work, we utilize self-assembled monolayers (SAMs) that present different functional groups, *i.e.,* CH_3, COOH, NH_2, and OH in order to fabricate well-defined hydrophobic, negatively charged, positively charged, and polar surfaces, respectively (Love et al. 2005). The adsorption and aggregation of hIAPP and rIAPP on these SAMs is investigated *in situ* and *ex situ* by quartz crystal microbalance with dissipation monitoring (QCM-D) and atomic force microscopy (AFM), respectively. QCM-D is a powerful method for investigating protein-surface interactions as it

allows for the quantitative *in-situ* monitoring of protein adsorption dynamics at organic and inorganic surfaces (Dixon 2008). Furthermore, QCM-D also yields information about the viscoelastic properties of the adsorbed film by assessing the change in dissipation upon adsorption (Hemmersam et al. 2005; Dixon 2008; Hemmersam et al. 2008). AFM, on the other hand allows for the assessment of adsorbate and aggregate morphology with nanometer resolution (Goldsbury et al. 1999; Adamcik et al. 2010; Adamcik and Mezzenga 2011; Keller et al. 2011a; Liu et al. 2012; Yu et al. 2012b; Jordens et al. 2014; Hajiraissi et al. 2017). By combining these techniques and applying them to molecularly defined SAMs, we investigate the effect of physicochemical surface properties on hIAPP assembly. In particular, we assess the role of molecular interactions beyond electrostatic and hydrophobic interactions, such as hydrogen bond formation between surface and peptide, which may cause significant fibrillization even in the presence of electrostatic repulsion.

5.2 Materials & Methods

5.2.1 Materials

hIAPP(1-37) and rIAPP(1-37) were purchased from BACHEM. 1,1,1,3,3,3-Hexafluoro-2-propanol (HFIP, ≥ 99 %) and dimethylsulfoxide (DMSO, ≥ 99.7 %) were purchased from Sigma-Aldrich. Phosphate buffered saline (PBS, 137 mM NaCl, 2.7 mM KCl, 10 mM Na_2HPO_4, pH 7.4) was purchased from VWR and prepared using HPLC-grade water (VWR). 1-Octadecanethiol, 11-Mercaptoundecanoic acid, 11-Mercapto-1-undecanol, 11-Amino-1-undecanethiol hydrochloride were purchased from Sigma-Aldrich.

5.2.2 Sample preparation

In order to prepare homogenous monomer solutions, one milligram of IAPP (human or rat) was carefully dissolved in 256 µl of HFIP for 1 h with occasional vortexing. The solution was then centrifuged at 15 000 rpm and 4˚C for 30 min, after which the top 80 % of the total volume was removed and divided into 10 µl aliquots. Aliquots were frozen in liquid nitrogen and lyophilized for 5 h. The lyophilized IAPP aliquots were stored at -20˚C. Right before the experiment, four IAPP aliquots were slowly brought to room temperature and dissolved in 10 µl of DMSO each. After incubation at room temperature for 10 min, all four aliquots were transferred into a single tube containing 3960 µl of PBS to reach a final concentration of 10 µM IAPP and 1 % DMSO, respectively. After vortexing for 15 s, the sample solution was injected into the QCM-D chamber.

5.2.3 SAM formation

1-Octadecanethiol, 11-Mercaptoundecanoic acid, 11-Mercapto-1-undecanol, and 11-Amino-1-undecanethiol hydrochloride were each dissolved in ethanol to a final concentration of 1 mM. Gold-coated quartz crystal sensors (Filtech Inc.) were cleaned in RCA1 (1:1:5 35 % H_2O_2, 25 % NH_3, and water) for 5 min at 75˚C and immersed in the respective solutions for 24 h to form SAM-terminated surfaces. Immediately prior to the experiment, the SAM-coated sensors were rinsed with ethanol and dried with nitrogen. Successful SAM formation was verified using contact angle measurements and X-ray photoelectron spectroscopy (Hajiraissi et al. 2018).

5.2.4 QCM-D

QCM-D measurements were performed using a Q-Sense E4 (Biolin Scientific) at 37˚C in dynamic mode. After stabilization of the QCM-D system with peptide-free PBS, IAPP-containing buffer was

injected into the cells at 10 µl/min. After 5.6 h, the QCM-D cells were flushed with peptide-free PBS for 120 min. All QCM-D experiments have been performed at least three times and similar trends have been observed. We have attempted to analyze the obtained frequency and dissipation shifts using the Voigt model (Voinova et al. 1999) which, however, failed to yield consistent and reproducible mass and viscosity data. This is in agreement with previous observations that standard viscoelastic models such as the Voigt model are unable to correctly treat fibril formation at the sensor surface (Hovgaard et al. 2007). Therefore, in this work, we evaluate only the frequency and dissipation shifts of the 7th overtone which, however, should be considered only rather crude measures of adsorbed mass and film viscosity, respectively. The other overtones measured are shown in the Supporting Information.

5.2.5 AFM

After the QCM-D measurements, the quartz sensors were removed from the cells, washed with MQ-water for 10 seconds and dried in a stream of ultrapure air for AFM imaging. While drying does not induce major changes in fibril morphology (Maurstad et al. 2009), washing with water instead of buffer may induce further desorption of adsorbates from the sensor surface. In order to minimize this effect, washing was performed as gentle as possible. *Ex-situ* AFM imaging was performed in intermittent contact mode in air using a JPK Nanowizard II and a JPK Nanowizard III AFM, and HQ:NSC18/Al BS cantilevers from MikroMasch with a nominal force constant and tip radius of 2.8 N/m and 8 nm, respectively. Heights of hIAPP fibrils were measured from line sections using Gwyddion open source software (Nečas and Klapetek 2012). At least 100 fibrils imaged at different positions on the sensor surfaces have been analyzed for each SAM.

5.3 Results & Discussion

Under physiological conditions, hIAPP features three positively charged amino acid residues (Lys1, Arg11, His18) in addition to its N-terminal charge, and 14 hydrophobic ones (see **figure 5-1**)(Cao et al. 2013). Therefore, its interaction with surfaces, *i.e.,* adsorption kinetics and conformation of adsorbed monomers, will be influenced both by hydrophobic and electrostatic interactions. Consequently, the interplay of these surface interactions may have pronounced and non-trivial effects also on aggregation dynamics and aggregate morphology (Keller et al. 2011a). In this work, we thus attempted to control these surface interactions of hIAPP by utilizing SAMs for the fabrication of molecularly defined hydrophobic, negatively charged, positively charged, and polar model surfaces. Non-amyloidogenic rIAPP is used as a control that shows monomer adsorption but no fibrillization.

5.3.1 Hydrophobic CH_3-terminated SAM

Figure 5-2 shows the shift of the resonance frequency Δ*F* of the quartz crystal sensor as a function of time for hIAPP and rIAPP in contact with the hydrophobic CH_3 SAM. In QCM-D, a decrease and increase in Δ*F* correlates with an increase and decrease of mass on the sensor surface, respectively (Dixon 2008). Upon peptide injection at $t = t_0$, a strong decrease in Δ*F* is observed for both peptides corresponding to rapid adsorption, and followed by a regime of slow saturation. At $t = t_1$, the QCM-D cells were flushed with peptide free buffer, resulting in the desorption of reversibly adsorbed species. Obviously, rIAPP adsorption leads to a stronger decrease in Δ*F*, indicating stronger monomer adsorption than for hIAPP. This might be due to the more hydrophobic

character of rIAPP caused by the substitutions of Ser28 and Ser29 by prolines (see **figure 5-1**). Desorption, on the other hand, leads to a rather similar increase in Δ*F* by about 4 – 5 Hz.

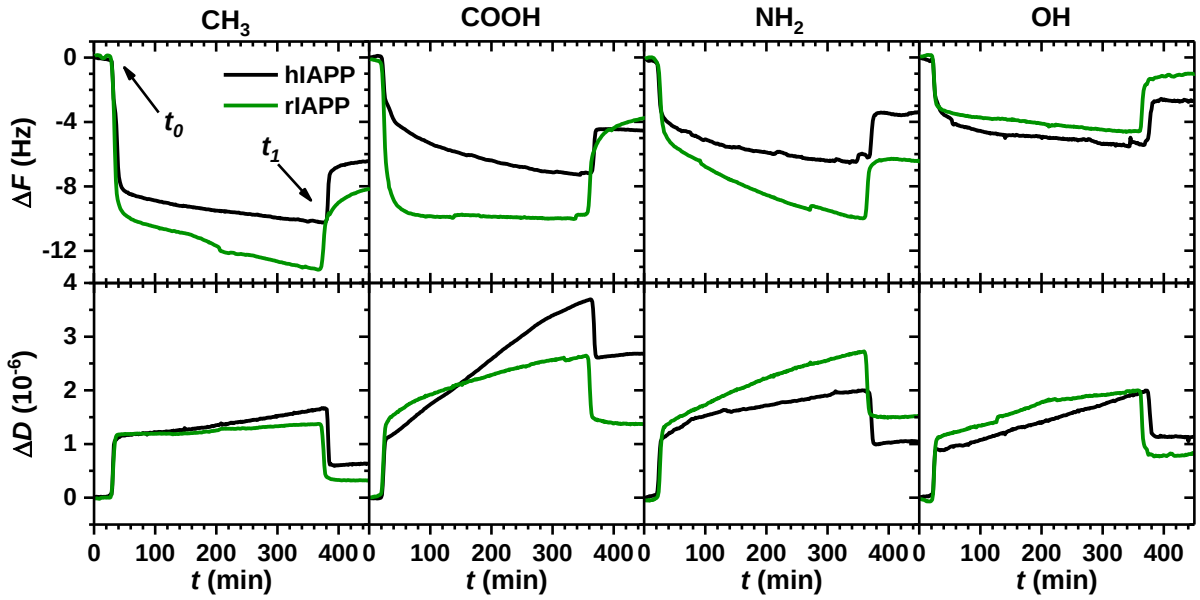

Figure 5-2. *QCM-D measurements (frequency shift ΔF and change in dissipation ΔD) of the adsorption of hIAPP and rIAPP at the different SAMs. The time points of peptide and buffer injection, t_0 and t_1, respectively, are indicated in the first ΔF plot.*

Changes in dissipation Δ*D* due to hIAPP and rIAPP adsorption and desorption at the CH_3 SAM are also shown in **Figure 5-2**. Adsorption results in a rather similar increase of Δ*D* for both peptides, corresponding to the formation of viscoelastic adsorbate films (Dixon 2008). In order to better compare the viscolelastic properties of the irreversibly adsorbed peptides, we have calculated the so-called loss factor -Δ*D*/Δ*F* for the stationary regime after flushing. This factor is a measure of the change in dissipation per unit frequency shift and thus mostly independent of adsorbed mass (Hemmersam et al. 2005; Hemmersam et al. 2008). For hIAPP and rIAPP, rather low loss factors of 0.10 x 10^{-6} Hz^{-1} and 0.04 x 10^{-6} Hz^{-1} are obtained, respectively (see **table 5-1**), indicating similar viscoelastic properties in both cases. In agreement with this observation, the AFM images shown

in **Figure 5-3** reveal few rather short fibrils in the case of hIAPP, while no rIAPP aggregates are observed at all.

Table 5-1: *ΔF, ΔD,* and *-ΔD/ΔF values of the different systems obtained at the end of the QCM-D measurements, i.e., after flushing with peptide-free buffer. All values have been determined for the 7th overtone.*

	CH_3		COOH		NH_2		OH	
	hIAPP	**rIAPP**	**hIAPP**	**rIAPP**	**hIAPP**	**rIAPP**	**hIAPP**	**rIAPP**
ΔF (Hz)	**-6.38**	**-8.03**	**-4.47**	**-3.70**	**-3.34**	**-6.80**	**-2.74**	**-1.04**
ΔD (10^{-6})	**0.64**	**0.32**	**2.73**	**1.37**	**1.06**	**1.54**	**1.13**	**0.84**
-ΔD/ΔF (10^{-6} Hz^{-1})	**0.10**	**0.04**	**0.61**	**0.37**	**0.32**	**0.23**	**0.41**	**0.81**

Our observations of strong monomer adsorption and low fibrillization at the hydrophobic CH_3 SAM are in accordance with previous studies. Jeworrek *et al.* observed much stronger adsorption of hIAPP on hydrophobic polymer surfaces than on charged ones (Jeworrek et al. 2009). For thin hydrocarbon films, it was furthermore observed that increasing the hydrophobicity continuously delayed hIAPP fibrillization, until at fully hydrophobic surfaces, fibrillization was completely suppressed (Keller et al. 2011a). Therefore, it can be concluded that hIAPP monomers have a high affinity for hydrophobic surfaces due to the strong interactions with their hydrophobic amino acid residues. Because of this strong hydrophobic interaction, however, it appears that the adsorbed monomers have a low surface mobility and therefore cannot assemble into fibrils. Furthermore,

the strong hydrophobic interactions appear to result in strong surface attachment of the few formed fibrils which is reflected in the comparatively low loss factor of 0.1 x 10^{-6} Hz^{-1}.

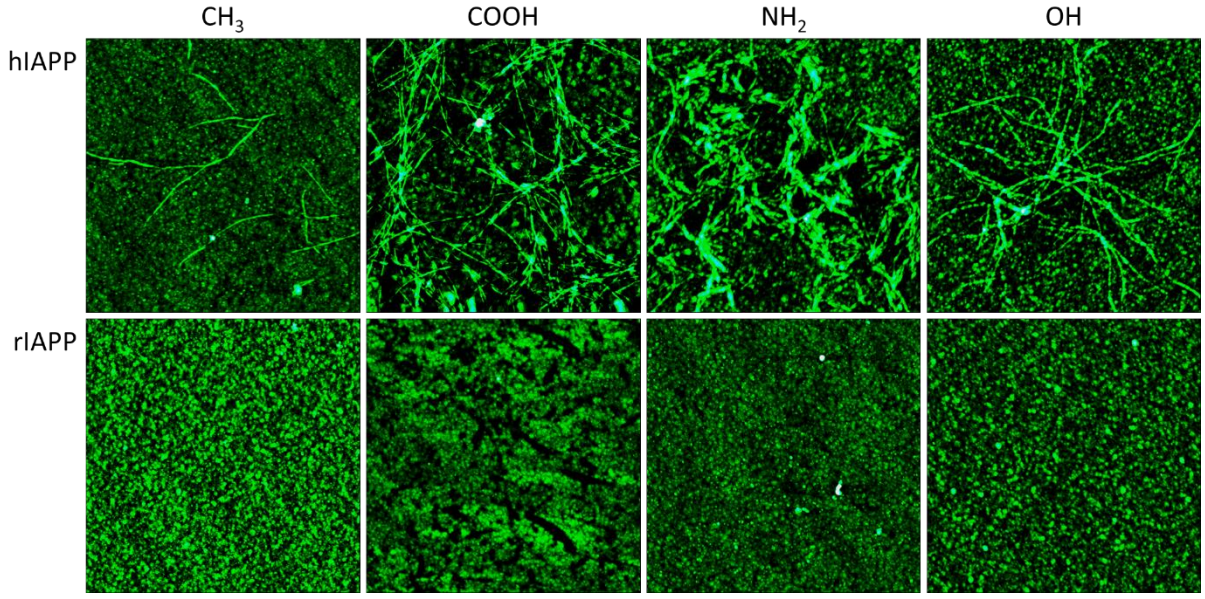

Figure 5-3. *AFM images of the sensor surfaces after peptide adsorption and flushing. AFM images have a size of 4 x 4 µm², height scales are 30 nm.*

5.3.2 Negatively charged COOH-terminated SAM

Under physiological conditions, the terminating groups of the COOH-terminated SAM will be deprotonated and thus carry a negative charge. The Δ*F* and Δ*D* curves for adsorption to the negatively charged COOH SAM shown in **Figure 5-2** reveal significantly different adsorption behaviors than in the case of the CH_3 SAM. In particular, adsorption leads to a significantly weaker decrease in Δ*F*, which is accompanied by a much stronger increase in Δ*D*. Therefore, it appears that IAPP adsorption to the negatively charged COOH SAM results in a rather viscoelastic adsorbate film, despite a lower adsorbed mass.

The adsorption and desorption behaviors of hIAPP and rIAPP at this SAM differ quite drastically. While hIAPP adsorption proceeds rather slowly, a strong initial adsorption with almost immediate saturation is observed for rIAPP. As for the CH_3 SAM, rIAPP adsorption leads to a larger frequency shift than hIAPP adsorption. After the sensor surfaces have been flushed with peptide-free buffer, however, both peptide-covered surfaces again show similar Δ*F* values, implying that a large fraction of the rIAPP monomers was adsorbed reversibly.

The Δ*D* curves in **Figure 5-2** show significant differences as well, with hIAPP adsorption resulting in larger changes in dissipation than rIAPP adsorption. Interestingly, for rIAPP, the Δ*D* curve is still increasing long after Δ*F* has reached a saturation value. This may indicate that the adsorbed rIAPP monomers undergo some slow reorganization in the adsorbate film, resulting for instance in conformational changes or trapping of water molecules. The observed differences in Δ*D* are still present after flushing. Different loss factors of 0.61×10^{-6} Hz^{-1} and 0.37×10^{-6} Hz^{-1} for hIAPP and rIAPP, respectively, indicate the formation of hIAPP fibrils dangling from the surface into solution while rIAPP forms a more rigid adsorbate film (see **table 5-1**). AFM confirms strong hIAPP fibrillization and the formation of a dense three-dimensional fibril network at the COOH SAM (see **figure 5-3**).

The effect that negatively charged surfaces promote fibrillization has previously been observed for hIAPP at phospholipid bilayers (Knight and Miranker 2004; Jayasinghe and Langen 2005; Caillon et al. 2013) and hIAPP(20-29) at mica surfaces (Hajiraissi et al. 2017). Our results furthermore suggest that the formed fibrils are comparatively loosely attached to the SAM and dangle or loop into solution, resulting in large dissipation values (see **figure 5-2**) and a large loss factor of 0.61×10^{-6} Hz^{-1}. This is in agreement with observations for hIAPP and hIAPP(20-29) assembly at

negatively charged liposomes (Knight and Miranker 2004) and mica surfaces (Hajiraissi et al. 2017), respectively. Similarly, the observed continuing increase of the Δ*D* curve after saturation of Δ*F* in the case of rIAPP and the strong desorption upon flushing suggest rather weak monomer attachment and thus high monomer mobility. In general, weak attractive interactions between the surface and the monomeric and aggregated peptide appear to be crucial for amyloid fibrillization at interfaces (Shen et al. 2012; Lin et al. 2014).

5.3.3 Positively charged NH_2-terminated SAM

As discussed above, hIAPP exhibits 3 positively charged amino acid residues plus one positive charge at the N terminus. Since hIAPP has a natively amidated C terminus, its electrostatic interaction with the protonated and thus positively charged NH_2 SAM will be purely repulsive. Nevertheless, the corresponding Δ*F* curve in **Figure 5-2** reveals significant adsorption of hIAPP on this SAM with a total frequency shift comparable to that observed for the COOH SAM. Although some desorption is observed due to flushing with peptide-free buffer, there is also a significant amount of irreversibly adsorbed material, indicating that electrostatic repulsion between peptide and surface does not play a dominant role. Rather, hIAPP adsorption to the NH_2 SAM may be attributed to the formation of hydrogen bonds between peptide and the terminating protonated NH_2 groups. Surprisingly, rIAPP shows an even stronger adsorption at the positively charged NH_2 SAM than hIAPP. This observation may be explained by the structural differences between hIAPP and rIAPP (Dupuis et al. 2009; Nanga et al. 2009) which might result in a more efficient screening of the positive charges in rIAPP. Although the Δ*D* curves in **Figure 5-2** reveal a lower change in

dissipation for hIAPP than for rIAPP, the obtained loss factors of 0.32 x 10^{-6} Hz^{-1} and 0.23 x 10^{-6} Hz^{-1}, respectively, indicate higher viscoelasticity of the adsorbed hIAPP (see **table 5-1**). This is in agreement with the strong hIAPP fibrillization observed by AFM (see **figure 5-3**).

The observation of significant hIAPP adsorption to the positively charged NH_2 SAM is in contrast to the results of Jeworrek *et al.,* who observed almost no adsorption of hIAPP on positively charged polyelectrolyte multilayers (Jeworrek et al. 2009). These different observations might be caused by different surface charge densities which will have a strong effect on adsorption due to the repulsive electrostatic interaction. According to the obtained loss factor of 0.32 x 10^{-6} Hz^{-1}, the hIAPP fibrils formed at the NH_2 SAM dissipate less energy than those at the COOH SAM, which can be attributed to the short length of the fibrils and the compact structure of the observed fibril bundles (see **figure 5-3**).

5.3.4 Polar OH-terminated SAM

For the polar OH-terminated SAM, rather similar Δ*F* curves are obtained for both peptides (see **figure 5-2**), with slightly stronger adsorption of hIAPP. The same holds also for the Δ*D* behavior, where after flushing, the adsorbed hIAPP has a slightly higher Δ*D*. These small differences, however, result in very different loss factors of 0.41 x 10^{-6} Hz^{-1} and 0.81 x 10^{-6} Hz^{-1} for hIAPP and rIAPP at the end of the experiment, respectively (see **Table 5-1**). These values are quite surprising, as they indicate that monomeric rIAPP adsorbed to the OH-terminated SAM has a drastically higher viscoelasticity than hIAPP. This counterintuitive behavior may be explained by the rIAPP monomer adopting a conformation in which it is bound to the surface alcohol group only with one

terminus while the rest of the molecule is dangling from the sensor surface. This would result in a brush-like adsorbate film that can trap large amounts of water, thereby drastically increasing the dissipation (Hemmersam et al. 2005). This upright conformation probably involves the ability of the terminal OH groups of the SAM to form hydrogen bonds with the native N terminus and the amidated C terminus of rIAPP. In case of hIAPP, however, adsorbed monomers are further assembled into fibrils that may dangle and loop from the surface and thereby increase the dissipation as well, but not as strongly as the brush-like rIAPP film.

On the OH-terminated SAM, we observe the lowest peptide adsorption for all SAMs. This may be explained by the rather specific hydrogen bonding between the terminating OH groups and the peptides' termini, compared to the more random hydrogen bonding between the terminating NH_2 groups and the peptide backbone and amino acid side chains. The obtained loss factor of 0.41 x 10^{-6} Hz^{-1} for hIAPP is in-between that of the COOH and NH_2 SAMs and may reflect differences in fibril density and arrangement: while the fibrils at the COOH SAM form an interwoven, three-dimensional network, the OH-terminated SAM rather shows smaller clusters of fibrils. In contrast, at the NH_2-terminated SAM, hIAPP fibrils are comparatively short and arranged in dense clusters, so that they cannot interact as strongly with the buffer medium.

5.3.5 Effect of physicochemical surface properties on hIAPP fibril morphology

It was previously shown for thin hydrocarbon films on mica surfaces that surface hydrophobicity not only affects hIAPP aggregation kinetics and aggregate density, but also aggregate and especially fibril morphology (Keller et al. 2011a). In particular, it was found that the diameter of

the formed fibrils decreases with increasing hydrophobicity until a transition from fibrils to oligomeric particles occurs. Such oligomeric particles of few nm heights cannot be identified in the AFM images shown in **Figure 5-3** due to the comparatively large roughness of the underlying gold electrodes. In order to assess fibril morphology more quantitatively, however, the heights of the formed fibrils have been determined from height histograms extracted from the AFM images (see **figure 5-4**) and are given in **Figure 5-5**.

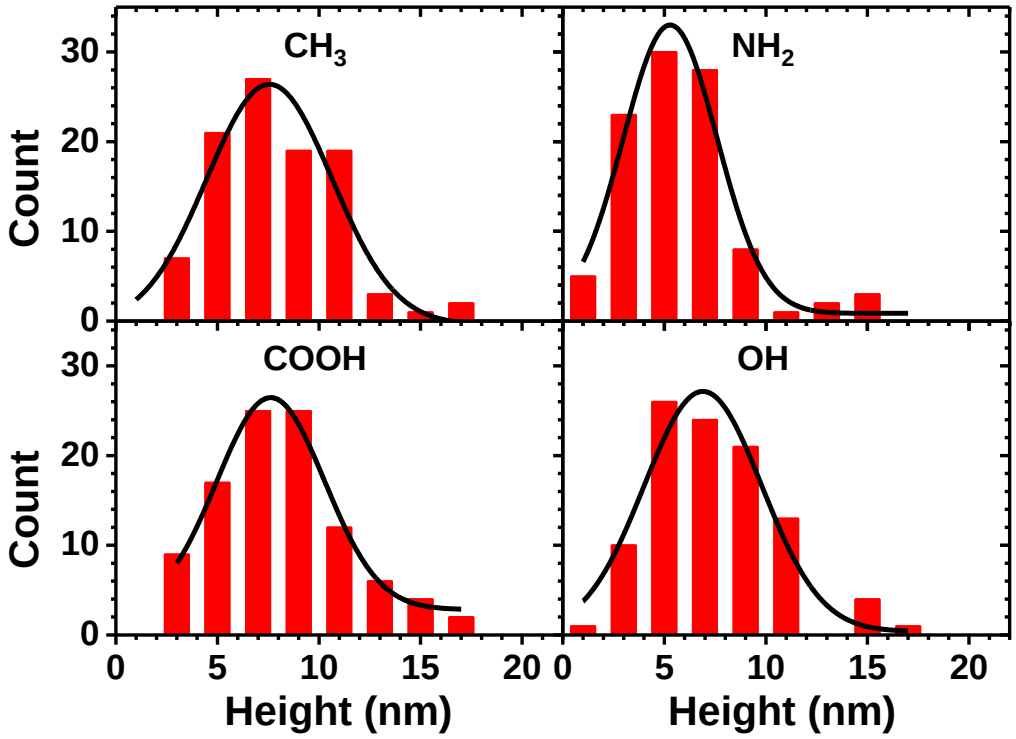

Figure 5-4. *Histograms of the heights of the hIAPP fibrils formed on the different SAMs. Solid lines represent Gaussian fits to the data.*

On the CH_3, COOH, and OH SAMs, the formed fibrils have almost identical mean heights of 7.0 to 7.5 nm, in agreement with previously reported heights of mature hIAPP fibrils formed in solution

(Goldsbury et al. 1999). On the positively charged NH_2 SAM, however, the mean fibril height is slightly reduced to 5.3 nm, which is in surprisingly good agreement with reported heights of mature hIAPP fibrils assembled at negatively charged, hydrophilic surfaces (Goldsbury et al. 1999; Keller et al. 2011a). However, in view of the comparably broad height distributions, this shift to lower heights may not be significant. The absence of any effect on fibril morphology due to increased hydrophobicity, on the other hand, may be due to the different surface chemistries and environmental conditions, most importantly buffer and temperature.

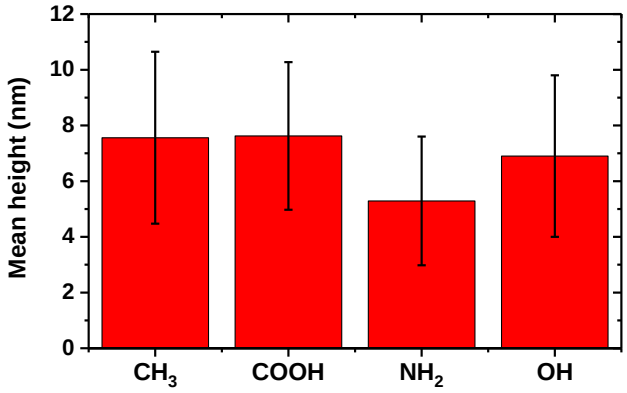

Figure 5-5. *Height values of formed hIAPP fibrils determined from Gaussian fits to the height histograms (see* ***figure 5-4)****. Error bars correspond to the FWHM of the height distributions.*

5.4 Conclusion

In this work, the effect of physicochemical surface properties on the adsorption and fibrillization of hIAPP was studied by a combination of QCM-D, and AFM using SAMs with different terminating groups as model surfaces and non-fibrillogenic rIAPP as a control. Our results are summarized in **Figure 5-6**.

At the hydrophobic CH_3-terminated SAM, strong monomer adsorption of hIAPP results only in few fibrils, which are furthermore firmly attached to the SAM, indicating that the fibrils grow along the surface. This behavior is attributed to dominant hydrophobic interactions between the terminal CH_3 groups and the hydrophobic amino acids of hIAPP, which cause the monomers to adopt a conformation that does not favor aggregation and restrict their surface mobility.

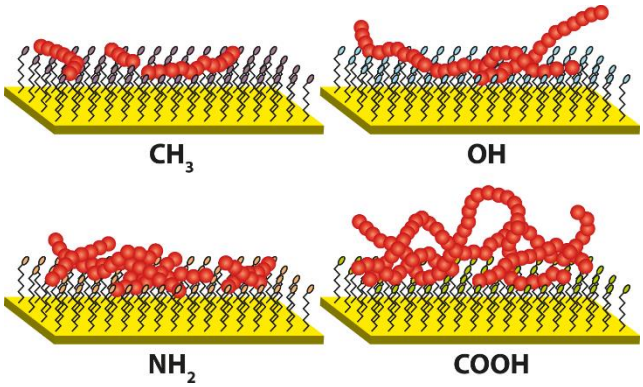

Figure 5-6. *Schematic representation of hIAPP fibrillization at the different SAMs.*

Stronger hIAPP fibrillization is observed for the hydrophilic OH SAM. Here, long and partially intertwined fibrils are formed which have a limited tendency to dangle into solution. Based on the comparison with non-fibrillogenic rIAPP, we assume that hydrogen bonding between the terminating OH groups and the peptide termini plays an important role in hIAPP assembly at this SAM.

At the positively charged NH_2-terminated SAM, many short fibrils are observed which further assemble into densely packed aggregates. The strong fibrillization at this surface is rather surprising since hIAPP carries only positive charges, so that the electrostatic interaction should be purely repulsive. Therefore, hIAPP adsorption to this SAM is probably dominated by hydrogen bonding with the terminating protonated NH_2 groups.

Strong hIAPP fibrillization is also observed at the negatively charged COOH SAM, which was found to be fully covered with a three-dimensional network of interwoven fibrils that dangle and loop from the surface into solution. In contrast to the CH_3 SAM where the fibrils appear to grow along the surface, this three-dimensional fibril network indicates that fibril growth proceeds via attachment of free monomers or oligomers from solution and does not require monomer adsorption to the SAM. This growth into solution in combination with their comparatively weak attachment to the surface suggests that fibrils formed at the negatively charged carboxylic acid interface have a high potential for promoting the formation of new fibrils in bulk solution via secondary assembly pathways, *i.e.*, fibril fragmentation and secondary nucleation (Cohen et al. 2013; Buell et al. 2014).

These results demonstrate the importance of physicochemical surface properties in interfacial amyloid assembly. By using molecularly defined model surfaces, we could furthermore show that molecular interactions beyond electrostatic and hydrophobic interactions may play a significant role, such as hydrogen bond formation between chemical groups of the surface and the peptide's termini, backbone, or amino acid side chains, resulting in significant adsorption and fibrillization even in the presence of electrostatic repulsion. The combination of QCM-D and AFM further allowed us to assess not only adsorption dynamics and aggregate morphology, but also gather information about the growth mode of the fibrils at the respective interfaces. This approach may provide fundamental insights into the molecular processes that govern amyloid assembly at cell membranes and thus contribute to understanding and ultimately controlling amyloid formation *in vivo*.

Chapter 6

Effect of Terminal Modifications on the Adsorption and Fibrillization of hIAPP(20-29) at SAMs

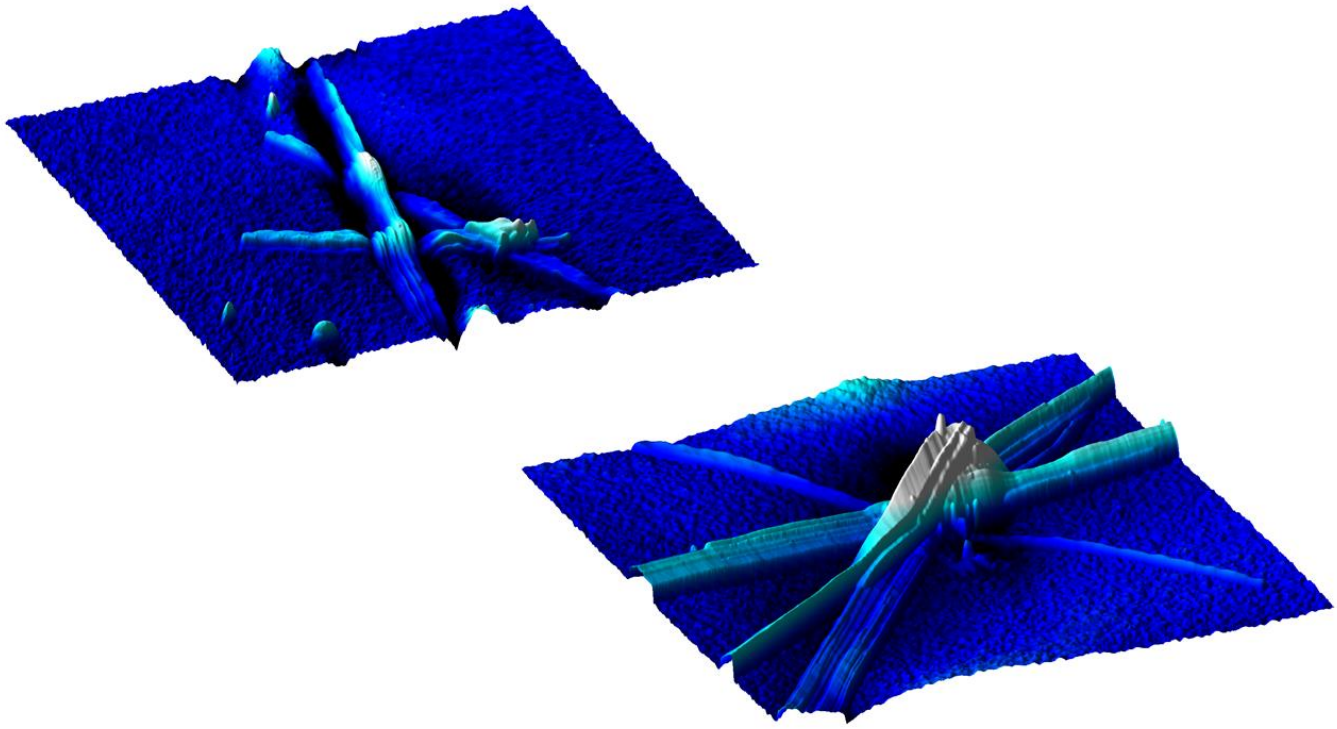

6.1 Introduction

Although self-assembly is considered as an advantage in naturally occurring systems (Huie 2003), fibrillization which is a longitudinal self-assembly is the hallmark of misfolding diseases such as Alzheimer, Parkinson, and Type 2 Diabetes Mellitus (T2DM). Amyloid fibrils are mainly composed of stacked β-strands positioned orthogonally along the fibril axis and stabilized by hydrogen bonds (Kajava et al. 2005). Although all amyloid fibrils share a common β-sheet structure, they show structural diversity (Kreplak and Aebi 2006).

In order to principally establish the controlling parameters contributing to polymorphism, many approaches have been investigated and it was reported that temperature (Sabaté et al. 2010), ionic strength (Marek et al. 2012), mutation (Goldsbury et al. 2000; Scrocchi et al. 2003; Abedini and Raleigh 2005), and surface hydrophobicity (Keller et al. 2011a; Hajiraissi et al. 2017) make the macromolecular peptide chain manifest various conformational states. Investigations regarding the IAPP which is involved in T2DM, showed that upon applying different amino acid regions of IAPP, the polymorphic structure of amyloid fibrils varies. Totally, in hIAPP three fibrillogenic regions have been ascribed as the fibrillogenic regions: *12-17*, *22-27*, and *31-37* (Pillay and Govender 2013). Among the aforementioned regions, the region *20-29* was ascribed as the core of fibrillization and many works have been reported to fully deconvolute the contribution of residue (20-29) to the amyloid aggregation (Griffiths et al. 1995; Madine et al. 2008; Jiang et al. 2009; Cabaleiro-Lago et al. 2010; Doran et al. 2012). Cabaleiro-Lago *et al.* analyzed the kinetics of fibrillization of this region *i.e.* hIAPP(20-29) in presence of polymeric nanoparticles with varying hydrophobicity (Cabaleiro-Lago et al. 2010). According to varying kinetics observed in the presence

of nanoparticles with varying hydrophobicity, they concluded that hydrogen bonding plays key role in amyloid aggregation as much as hydrophobic interaction. The contributions of hydrophobic and hydrogen interactions were further investigated by Sabaté *et al*. using hIAPP(1-37) (Sabaté et al. 2010). Interestingly, it was understood that amino acid distribution has a prominent influence on the amyloid aggregation and scattering of hydrophobic amino acids retards the initial nucleation process which was seen by increased lag phase (Sabaté et al. 2010). In agreement with Sabaté *et al*., Doran *et al.*, by using hIAPP(20-29) with varying hydrophobic amino acids, concluded that self-assembly is mainly driven by hydrophobic interactions and hydrogen bonds (Doran et al. 2012).

In biological environment, many biological surfaces exist and when the peptide/protein comes onto contact with the biological surfaces such as cell membranes, various states of conformational transitions happen which drive from the existent forces at the biointerface. By utilizing model surfaces such as lipid bilayers (Butterfield and Lashuel 2010), polymer surfaces (Cabaleiro-Lago et al. 2010), and mica surface (Goldsbury et al. 1999; Hajiraissi et al. 2017), it is possible to involve different residues by either hydrophobic interactions or electrostatic interactions in order to follow amyloid aggregation and fibrillization mechanism. Because of the presence of hydrophobic amino acids, in the presence of hydrophobic polymer surface the hIAPP(1-37) showed considerable adsorption. However, the amount of adsorption decreased at contact with negatively charged surfaces (Jeworrek et al. 2009). After incubation of hIAPP(20-29) on freshly cleaved mica surface which is negatively charged, it was turned out that the peptide mainly binds to the negative model surface by positive N-terminus and fibrillization proceeds via the hydrophobic amino acids which are resided in the region 20-29) (Hajiraissi et al. 2017; Hajiraissi et al. 2018). In

order to fortify the observed fibrillization of hIAPP(20-29), full length hIAPP(1-37) was used and the dynamics of adsorption was related to the fibrillization of the hIAPP(1-37) (Hajiraissi et al. 2018). In agreement with proposed fibrillization mechanism of hIAPP(20-29) at contact with negatively charged mica surface, hIAPP(1-37) showed that the full length hIAPP binds to the negatively functionalized SAM by positive N-terminus and positively charged amino acids which are in N-terminal region and thereafter, the fibrillization proceeds via C-terminal region in which the residue (20-29) plays key role in fibrillization (Hajiraissi et al. 2018).

From experimental point of view, many techniques are utilized to capture the formed morphology and to follow kinetics of fibrillization. Over the last decade AFM has proven itself as an efficient technique to observe the polymorphism of amyloid aggregates either formed in test tube or at contact with model surfaces (Goldsbury et al. 1997; Stolz et al. 2000; Kreplak and Aebi 2006). Combined with AFM, QCM-D has also been employed to follow the kinetics of amyloid aggregation in situ (Yu et al. 2012; Hajiraissi et al. 2018). This work is aimed at following the structural arrangement of hIAPP(20-29) at contact with molecularly defined self-assembled monolayers (SAM). In addition to employing different SAMs (hydrophobic, hydrophilic, negative, and positive charge surfaces), hIAPP(20-29) with various termini modified by acetylation and amidation which result in different charge states were used to extract the data regarding the self-assembly and adsorption trend of the peptides.

Figure 6-1 represents the amino acid sequences of hIAPP(20-29) modified with different functional groups. Consequently, based on various charged states, it is expected to observe different kinetics of ad/desorption and polymorphism.

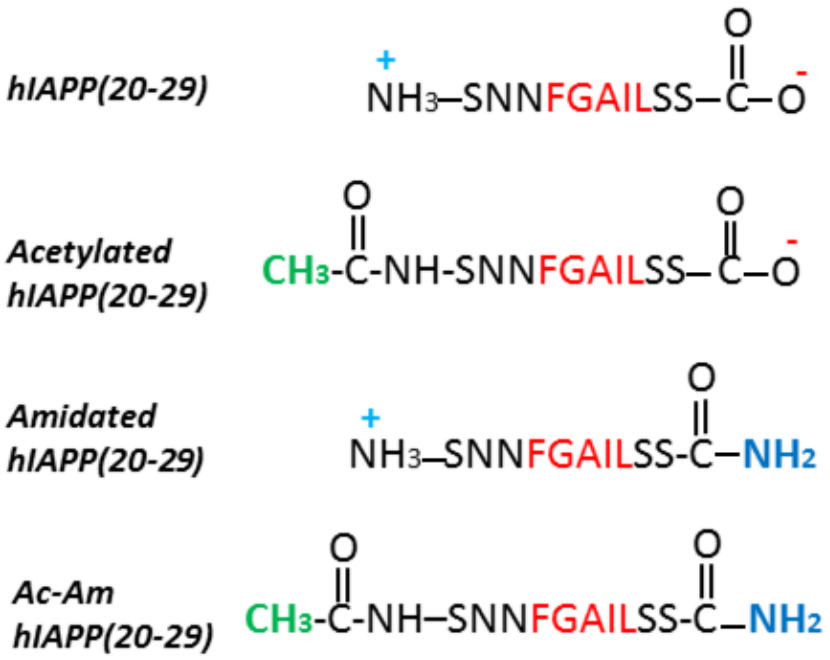

Figure 6-1 *Schematic structure of hIAPP(20-29) with various termini. The* ***native*** *hIAPP(20-29) has positive N-terminus and negative C-terminus. The* ***Ac****-hIAPP(20-29) has negative C-terminus and has net negative charge state. The* ***Am****-hIAPP(20-29) has positive N-terminus and positive net charge. The* ***Ac-Am****-hIAPP(20-29) has neutralized N- and C-termini and net charge of zero.*

6.2 Materials and Methods

6.2.1 Materials

hIAPP(20-29) with various termini were synthesized by Prof. Yixin Zhang (B CUBE- Center for Molecular Bioengineering, TU Dresden, Germany). The peptides were labeled as the following: **native** hIAPP(20-29)**,** Acetylated hIAPP(20-29): A**c**-hIAPP, Amidated hIAPP: **Am**-hIAPP, and Acetylated-Amidated-IAPP(20-29): **Ac-Am** hIAPP.

1,1,1,3,3,3 Hexafluoro-2-propanol (HFIP, ≥ 99 %) and dimethylsulfoxide (DMSO, ≥ 99.7 %) were purchased from Sigma-Aldrich. Phosphate buffered saline (PBS, 137 mM NaCl, 2.7 mM KCl, 10 mM Na_2HPO_4, pH 7.5) was purchased from VWR and prepared using HPLC-grade water (ROTH). 1-Octadecanethiol, 11-Mercaptoundecanoic acid, 11-Mercapto-1-undecanol, 11-Amino-1-undecanethiol hydrochloride were purchased from Sigma-Aldrich.

6.2.2 Sample preparation

In order to prepare homogenous monomer solutions, one milligram of hIAPP(20-29) was carefully dissolved in 100 µl of HFIP for 1 h with occasional vortexing. The solution was then centrifuged at 15 000 rpm and 4˚C for 30 min, after which the top 80 % of the total volume was removed and divided into 10 µl aliquots. Aliquots were frozen in liquid nitrogen and lyophilized for 5 h. The lyophilized hIAPP(20-29) aliquots were stored at -20˚C.

6.2.3 Thioflavin T (ThT) fluorescence analysis

Thioflavin T (ThT, Sigma-Aldrich) was freshly prepared before each experiment by dissolving 3 mg of ThT in 1 mL of HPLC-grade water (ROTH). The solution was then filtered through a 0.2 µm filter (VWR) and ThT concentration calculated from its absorbance in water at 412 nm measured on Implen Nanophotometer, using molar extinction coefficient of 36000 $M^{-1}cm^{-1}$.

Before the experiment, the concentration of the ThT solution which is prepared freshly, is calculated and ≈ 3 µl of the the stock solution was added to test tube to reach to final

concentration of 20 µM and then the the rest of the test tube is filled with required amount of the PBS to reach to 990 µl of PBS. Thereafter, the frozen hIAPP(20-29) is kept at room temperature to reach the room temperature and then 10 µl of DMSO is added to the aliquot to dissolve the peptide and after vortexing for 30 s, the dissolved DMSO-peptide is kept at room temperature for 10 min. At the final step, the dissolved DMSO-peptide solution is added to the test tube containing 990 µl of PBS and ThT to reach to final volume of 1 ml and to final concentration of 100 µM and finally the test tube is vortexed for 15 s and is distributed into wells of the micro plate (each well is filled with 200 µl of the solution).

To analyze the kinetics of bulk aggregation, ThT fluorescence measurement was conducted at 37˚C in PBS (pH 7.5) for 6 hr and the fluorescence intensities were recorded on a 96-well black microplate (TriStar^2 S LB 942-BERTHOLD TECHNOLOGY). ThT was excited at 440 nm and fluorescence emission monitored at 495 nm (Freire et al. 2014). The fluorescent measurement was repeated three times and the averaged curves were plotted (see **figure 6-2**)

6.2.4 SAM formation

1-Octadecanethiol, 11-Mercaptoundecanoic acid, 11-Mercapto-1-undecanol, and 11-Amino-1-undecanethiol hydrochloride were each dissolved in ethanol to a final concentration of 1 mM. Gold-coated quartz crystal sensors (Filtech Inc.) were cleaned in RCA1 (1:1:5 35 % H_2O_2, 25 % NH_3, and water) for 5 min at 75˚C and immersed in the respective solutions for 24 h to form SAM-terminated surfaces. Immediately prior to the

experiment, the SAM-coated sensors were rinsed with ethanol and dried with nitrogen. Successful SAM formation was verified using contact angle measurements and X-ray photoelectron spectroscopy (Hajiraissi et al. 2018).

6.2.5 QCM-D

Right before the experiment, eight hIAPP(20-29) aliquots were slowly brought to room temperature and dissolved in 10 µl of DMSO each. After incubation at room temperature for 10 min, all eight DMSO-peptide aliquots were transferred into a single tube containing 7920 µl of PBS to reach a final concentration of 100 µM hIAPP(20-29) and 1 % DMSO, respectively. After vortexing for 15 s, the sample solution was injected into the QCM-D chamber.

QCM-D measurements were performed using a Q-Sense E4 (Biolin Scientific) at 37˚C in dynamic mode. After stabilization of the QCM-D system with peptide-free PBS, IAPP-containing buffer was injected into the cells at 10 µl/min. After 13.5 h, the QCM-D cells were flushed with peptide-free PBS for 120 min. Frequency and dissipation shifts were evaluated for the 7th overtone. After 13.5 hr of injection, the cells were flushed with pure PBS for 2 hr and then the quartz sensors were removed from the cells, washed with MQ-water for 10 seconds and dried in a stream of ultra-pure air for AFM imaging.

6.2.6 AFM

Ex-situ AFM imaging was performed in intermittent contact mode in air using a JPK Nanowizard II and a JPK Nanowizard III AFM, and HQ:NSC18/Al BS cantilevers from MikroMasch with a nominal force constant and tip radius of 2.8 N/m and 8 nm, respectively.

Bulk morphology of various termini of hIAPP(20-29) was taken by depositing 40 µL of hIAPP(20-29) solution from the well of micro plate which experienced the plate reader measurement, on freshly cleaved mica surface. The solution on mica was kept for 10 min and then the mica surface was washed gently with MQ-water and then was dried with ultra-pure air stream.

6.3 Results & Discussion

6.3.1 Kinetics of hIAPP(20-29) in Bulk

To better follow the work, it would be useful to analyze the structures of peptides used in this work. At first step, the kinetics of amyloid aggregation was evaluated in bulk state using fluorimetry. The DMSO-dissolved IAPPs (**native, Ac-, Am-, and Ac-Am**) were then dissolved in PBS as medium at pH 7.5.

Kinetics of fibrillization is commonly followed by measuring the fluorescence intensity of thioflavin T (ThT) upon binding to the β-sheets (Freire et al. 2014). Releasing signals of various hIAPPs follow a sigmoidal shape whose intensity curves are divided into three regions: lag phase, exponential growth, and flat state. At pH 7.5 **native** hIAPP(20-29) and **Ac-Am**-hIAPP(20-29)s have the net charge of zero. On the other hand, **Ac**-hIAPP(20-29) and **Am**-hIAPP(20-29) possess negative and

positive charge states respectively. **Figure 6-2** shows the fluorescence curves of the hIAPP(20-29) with various termini. As is conspicuous, all four fragments show similar lag phases whose durations take about 600 s followed by exponential growth and plateau.

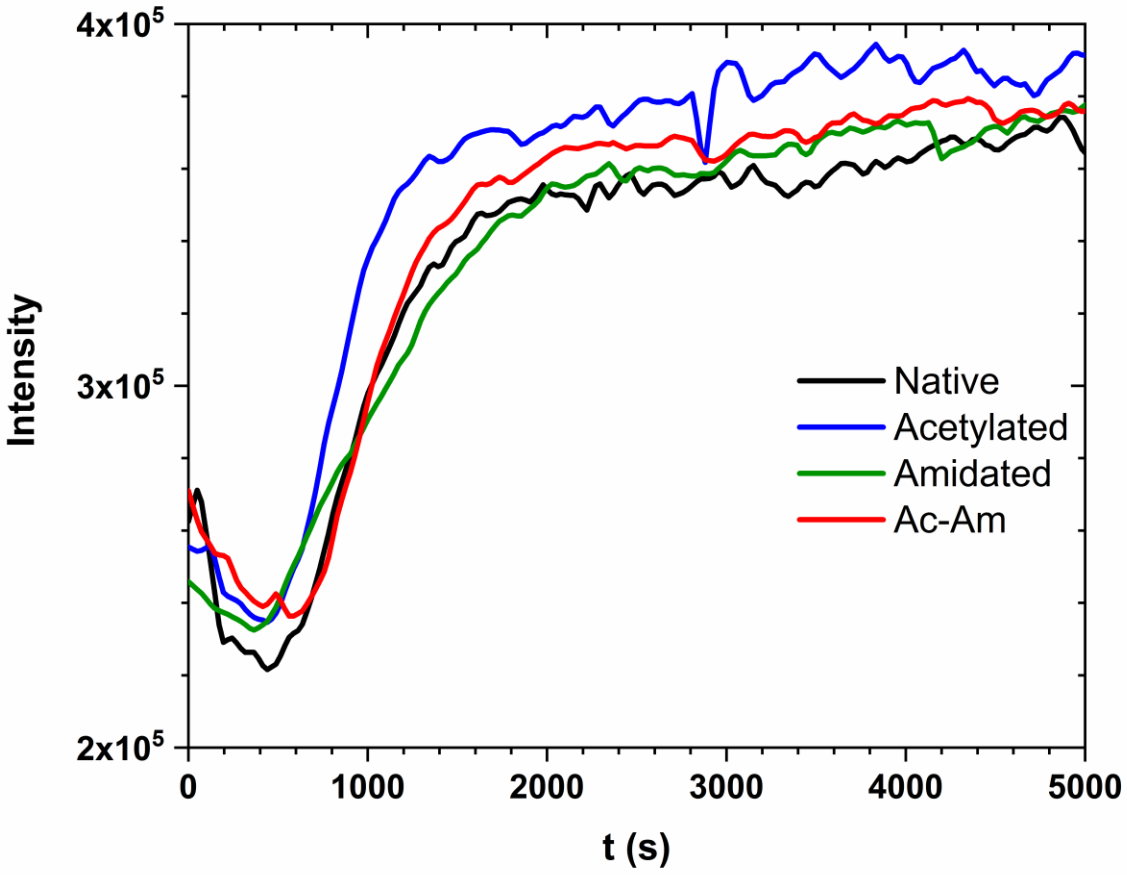

Figure 6-2 *ThT fluorescence intensity of hIAPP(20-29) with various termini. The experiment was performed at 37°C in PBS at pH 7.5.*

Figure 6-3 shows the AFM images of hIAPP(20-29) with various termini. As is conspicuous, any remarkable morphology is not observed.

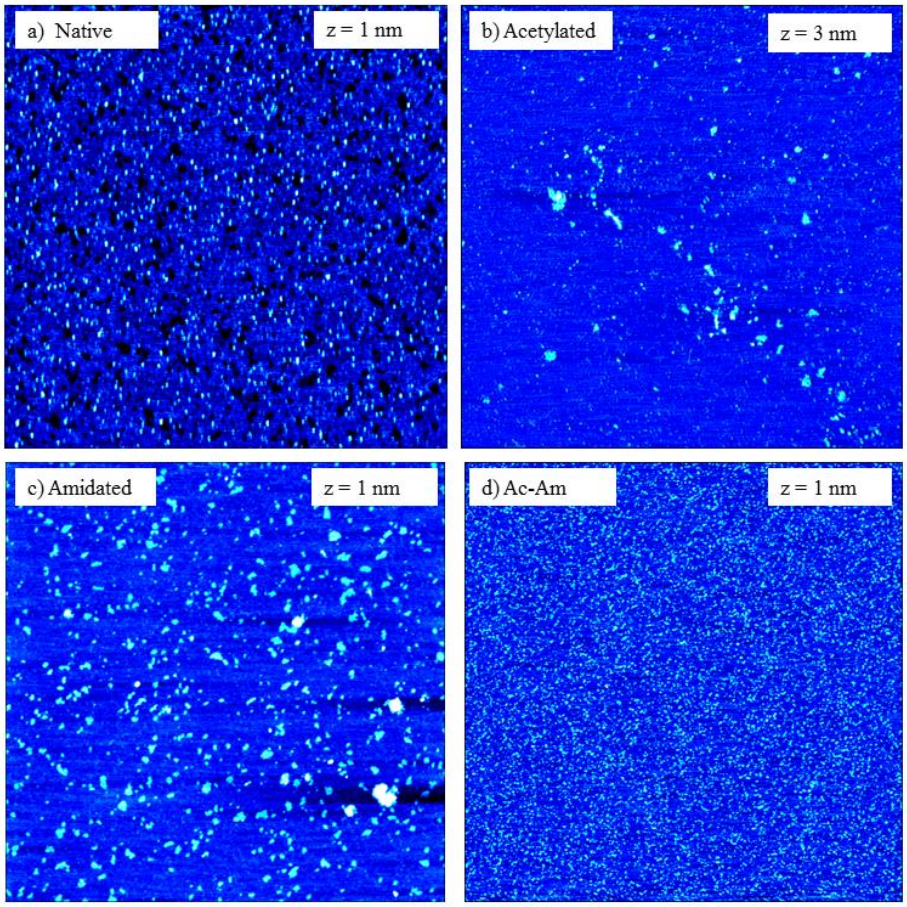

Figure 6-3 *AFM images of hIAPP with various termini experienced bulk measurement. The image size is 2× 2 µm.*

6.3.2 Effect of Molecularly Defined Self-assembled Monolayers on Aggregation

6.3.2.1 Effect of OH-terminated SAM

Figure 6-4 represents the extracted data from QCM-D and AFM images of QCM-D sensors after finishing the measurement. Combination of the ex situ AFM and QCM-D was previously reported and the formed structures of hIAPP(1-37) were properly correlated with dynamics of fibrillization

at contact with various charged SAMs (Hajiraissi et al. 2018). **Figure 6-4 a-b** represents the QCM-D curves of adsorption and dissipation of hIAPP(20-29) with various termini at contact with OH-terminated surface.

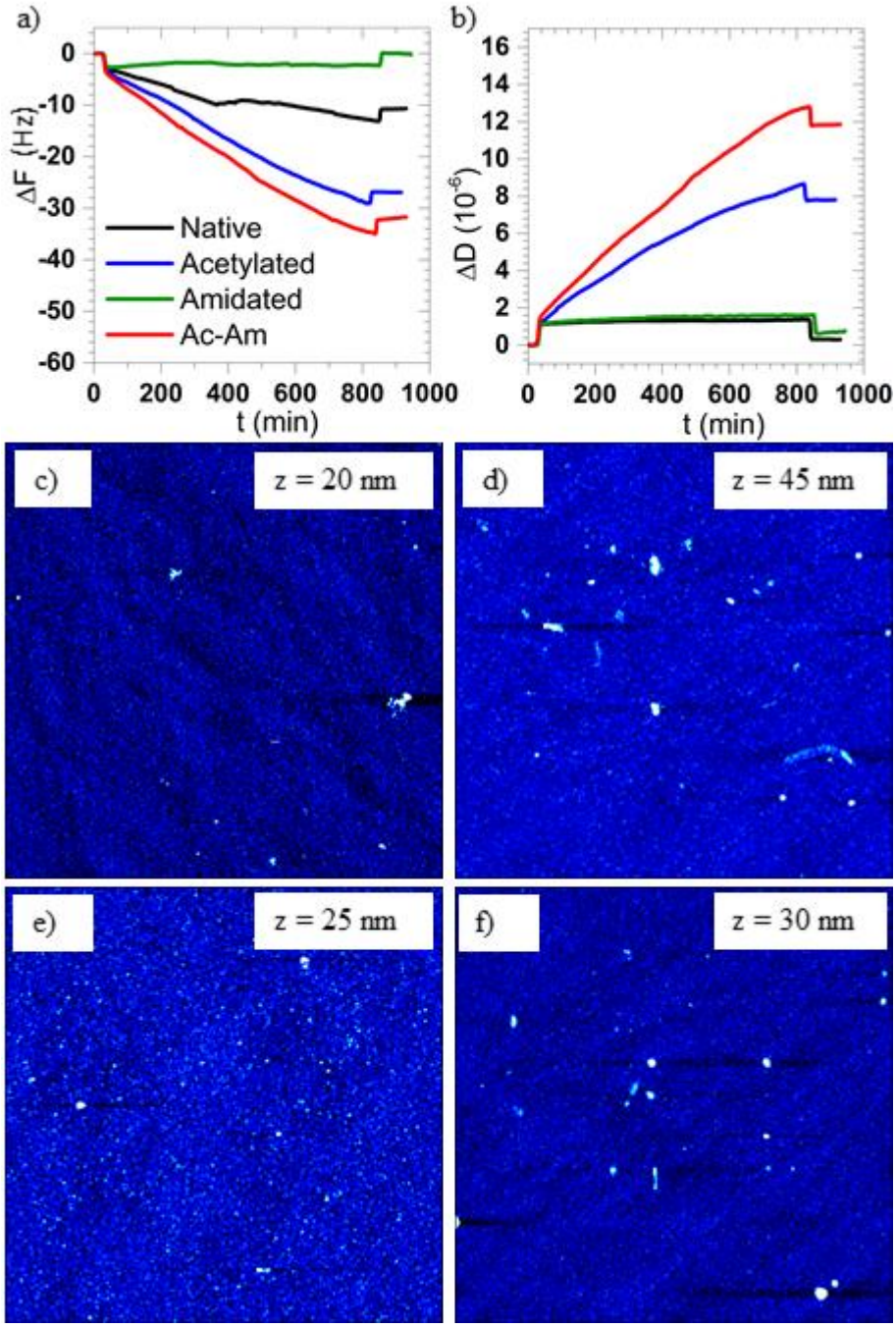

Figure 6-4. *Frequency shift, dissipation curves, and AFM images of various functionalized termini of hIAPP(20-29) after incubation at* ***OH****-terminated Surface: a) frequency shift ΔF, b) dissipation ΔD. c)* ***native*** *hIAPP(20-29), d)* ***Ac****-hIAPP(20-29), e)* ***Am****-hIAPP(20-29), f)* ***Ac-Am****-hIAPP(20-29). Images have a size of 10 × 10 µm². The ranges of the z scales are given in the individual images.*

Frequency dissipation shown in **Figure 6-4 a** represents the dynamics of peptide adsorptions. At the beginning of the experiment a steady state is observed which belongs to the injection of peptide-free PBS solution and upon injection of the dissolved-peptide PBS solution into the cells, a rapid decrease in frequency ΔF is observed at the beginning of the injection for all four peptides which is reflective of peptide deposition on the quartz crystals. During the time course of the peptide injection, the kinetics of **native**, **Ac**-, and **Ac-Am-**hIAPPs represent a gradual decrease of the frequency value which is representative of inclination of the peptide to bind to the surface, albeit with varying trends. Based on the ΔF values, **Ac**-**Am**-hIAPP shows the strongest adsorption tendency and at the second place lies **Ac**-hIAPP(20-29) (see **Table 6-1**). The **Am**-hIAPP(20-29) shows the lowest amount of adsorption and after a sudden decrease of ΔF, **Am**-IAPP reaches to a saturated state.

At the end of the experiment, the cells were washed with pure buffer. The frequency value of the adsorbed **native** hIAPP(20-29) which shows lower tendency to the OH-functionalized surface than **Ac**-hIAPP(20-29) and **Ac-Am**-hIAPP(20-29), after flushing with pure PBS, lies around -10.77 Hz. Also flushing the cell containing **Ac**-hIAPP(20-29) manifests high value of adsorption and at the end of the experiment the frequency value lies by about -26.81 Hz. By washing the cells, it is seen that **Am**-hIAPP(20-29) shows full reversibility, and **Ac-Am**-hIAPP(20-29) represents the strongest value of adsorption about -32.045 Hz (see **Table 6-1**).

Table 6-1 *ΔF, ΔD, and -ΔD/ΔF values of the hIAPP(20-29) with various termini at contact with OH-functionalized surface (the numbers were obtained at the end of the QCM-D measurements, i.e., after flushing with peptide-free buffer. All values have been determined for the 7th overtone. As for the case of* ***Am****-hIAPP(20-29) no adsorption was observed, the dissipation and loss factor were left blank.*

	Native hIAPP(20-29)	**Ac-hIAPP(20-29)**	**Am-hIAPP(20-29)**	**Ac-Am-hIAPP(20-29)**
ΔF (Hz)	**-10.77**	**-26.81**	**-0.04**	**-32.045**
ΔD (10^{-6})	**0.33**	**7.8**	**-**	**11.84**
-ΔD/ΔF (10^{-6} Hz^{-1})	**0.03**	**0.3**	**-**	**0.36**

Figure 6-4 b represents the dissipation values of formed peptide films. After steady state, a rapid increase of ΔD is observed which is indicative of peptide deposition and forming a peptide layer on the quartz sensors. After peptide deposition, the dissipation curves are followed in two trends: *i)* **native** hIAPP(20-29) and **Am**-hIAPP(20-29) show a plateau which shows that the formed layers have low viscoelasticity, *ii)* in accordance with significant adsorption of **Ac**-hIAPP(20-29) and **Ac-Am**-hIAPP(20-29), the dissipation curves of **Ac**-hIAPP(20-29) and **Ac-Am**-hIAPPs represent steep increase in dissipation which implies on forming layers with high viscoelastic characteristics. At the end of the experiment upon flushing the system with pure buffer, it is observed that dissipation decreases which is the consequence of removing the unbound monomers from the surface.

By introducing OH-terminated SAM, the potential of hydrogen bonding is involved and it would be possible to predict the efficiency of hydrogen bonding in aggregation and fibrillization.

The **native** hIAPP(20-29) shows the adsorption potential less than **Ac**-hIAPP(20-29) and **Ac-Am**-hIAPP(20-29). Interestingly, it is seen that upon amidation, the **Am**-hIAPP(20-29) shows no adsorption. Therefore, this would be proposed that the adsorption is conducted from *C-terminal region* whose amidation deteriorates the peptide adsorption. Consequently, it can be considered that the adsorption of the **native** hIAPP(20-29) proceeds via interaction between the peptide backbone/amino acids and the OH-terminated surface. According to the small dissipation of **native** hIAPP(20-29), it may be proposed that a film with low viscoelasticity forms on the surface. The loss factor of 0.03×10^{-6} Hz^{-1} of **native** hIAPP(20-29) is indicative of low ability of the peptidic monomer to dissipate the energy on the OH-terminated surface (Hemmersam et al. 2005; Dixon 2008; Hemmersam et al. 2008; Hajiraissi et al. 2018). In this regard, after attachment to the surface from *C-terminal region*, the peptide may come close to the surface by hydrogen bonding to the OH-terminated surface and lies down on the OH-terminated surface.

Ac-hIAPP(20-29) shows higher adsorption, higher dissipation and loss factor than **native** hIAPP(20-29). It is expected to consider the adsorption of **Ac**-hIAPP(20-29) via proceeding the hydrogen bonds between the *acetylated N-terminal* of the **Ac**-hIAPP(20-29) and the OH-terminated SAM. Interestingly, the high loss factor indicates that the peptide has high dissipation ability. In this case, it may be possible for the **Ac**-hIAPP(20-29) to take a dangling conformation.

In the presence of OH-terminated SAM, the outstanding result may belong to the **Ac-Am**-hIAPP(20-29) which has the highest frequency, dissipation, and loss factor. It is also possible to visualize the **Ac-Am**-hIAPP(20-29) as a horizontally attached monomer whose monomer backbone is attached to the OH-terminated SAM via hydrogen bonds, but due to high dissipation and loss factor which may be the results of trapped water molecules, this mechanism cannot be considered as the proposable mechanism (Hemmersam et al. 2005; Dixon 2008; Hemmersam et al. 2008; Hajiraissi et al. 2018), and it would be more conceivable to visualize a vertically attached **Ac-Am**-hIAPP(20-29) monomer which is able to represent a viscoelastic film with high dissipation potential. According to adsorption mechanism of the **Am**-hIAPP(20-29) since upon amidation the **native** hIAPP(20-29) lost its potential to bind to the surface, it can be predicted that the *acetylated N-terminus* leads mostly the adsorption in **Ac-Am**-hIAPP(20-29). The adapted conformation may be similar to the conformation proposed for **Ac-**hIAPP(20-29) at contact with OH-terminated SAM which a dangling monomer can easily dissipate the energy.

As is conspicuous from the AFM images (**figure 6-4 c-f**), after the time course of solution injection, any mentionable morphology is not observed.

6.3.2.2 Effect of NH_2-terminated SAM

Figure 6-5 shows the obtained results extracted from QCM-D and imaged surfaces of QCM-D sensors after finishing the measurement. In this measurement, the positively functionalized crystals with NH_2 end groups were used. In the presence of PBS at pH 7.5 the amine functional groups become protonated and function as positive functional groups (NH_3^+).

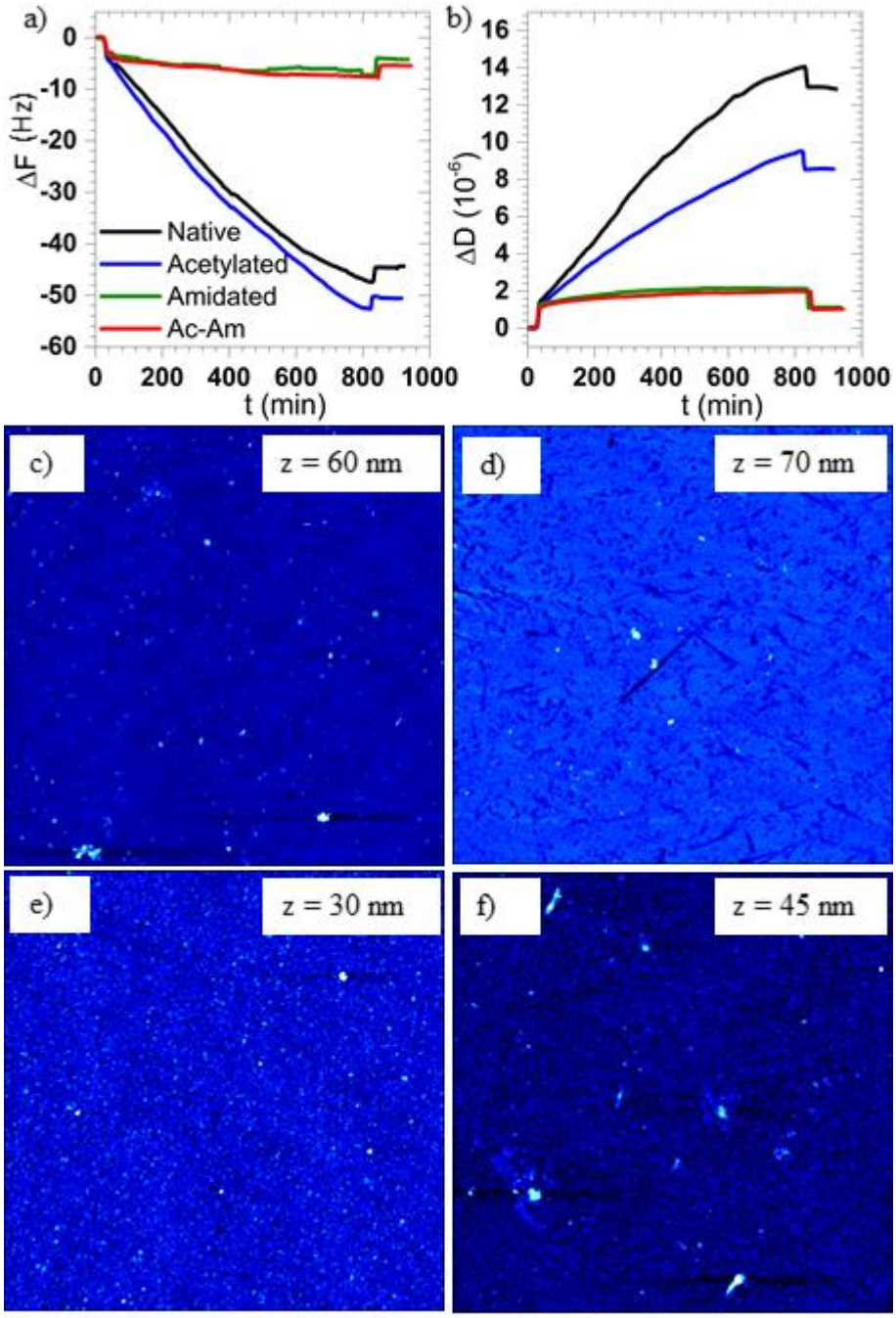

Figure 6-5. *Frequency shift, dissipation curves, and AFM images of various functionalized termini of hIAPP(20-29) after incubation at* ***NH_2****-terminated Surface: a) frequency shift ΔF, b) dissipation ΔD. c)* ***native*** *hIAPP(20-29), d)* ***Ac****-hIAPP(20-29), e)* ***Am****-hIAPP(20-29), f)* ***Ac-Am****-hIAPP(20-29). Images have a size of 10 × 10 μm^2. The ranges of the z scales are given in the individual images.*

Adsorption dynamics of four peptides are presented in **Figure 6-5 a**. The plateau at the beginning of the curve belongs to the injection of the pure buffer which shows the stability of the system. After reaching a stable condition, dissolved-peptide solutions are injected into the cells whose impacts are reflected by a sudden decrease in frequency value ΔF as indicator of mass deposition. From this point on and during the time course of the peptide injection, the frequency values decrease, albeit with varying trends. In the meantime, at which surface is accumulated with peptidic monomers, **native** and **Ac**-hIAPP(20-29) bind to the positively surface strongly which can be inferred from the steep decrease in ΔF values, whereas adsorption dynamics in systems containing **Am**-hIAPP(20-29) and **Ac-Am**-hIAPP(20-29) continue slowly. It is not far from expectation that **Ac**-hIAPP(20-29) with negative net charge shows the highest amount of adsorption because of the electrostatic attraction. On the other hand, electrostatic repulsion due to similar charge states between positively charged surface and **Am-**hIAPP(20-29) monomer leads to representing the least value of adsorption. **Native** and **Ac-Am**-hIAPP(20-29) possess neutral charge states, but the **native** hIAPP(20-29) has *negative C-terminus* (see **figure 6-1**) which makes the monomer susceptible to bind to the surface with opposite charge states. On the other hand, after modification of the monomer, the termini of the peptide become uncharged, and consequently, it is expected that a hydrophobic residue shows no inclination to the positively charged surface. At the end of the experiment, the cells were flushed with pure buffer which results in desorption of unbound monomers from the surface. It is seen that after flushing at the end of the experiment, the **native** and **Ac**-hIAPP(20-29) represent the strongest adsorption values, based on calculated ΔF (see **Table 6-2**) and compared with **Am**-hIAPP(20-29) and **Ac-Am**-hIAPP(20-29).

Table 6-2 *ΔF, ΔD, and -ΔD/ΔF values of the hIAPP(20-29) with various termini at contact with NH_2-functionalized surface (the numbers were obtained at the end of the QCM-D measurements, i.e., after flushing with peptide-free buffer. All values have been determined for the 7th overtone.*

	Native hIAPP(20-29)	**Ac-hIAPP(20-29)**	**Am-hIAPP(20-29)**	**Ac-Am-hIAPP(20-29)**
ΔF (Hz)	**-44.48**	**-50.38**	**-3.94**	**-5.28**
ΔD (10^{-6})	**13.06**	**8.52**	**1.08**	**1.03**
-ΔD/ΔF (10^{-6} Hz^{-1})	**0.3**	**0.17**	**0.27**	**0.2**

Figure 6-5 b shows the dissipation Δ*D* because of the deposition of peptides on the surfaces. At the beginning of the injection of the dissolved-peptide solutions, an increase in dissipation is observed which relates to the formation of a viscoelastic film (Dixon 2008). From the obtained dissipation curves which are indicative of viscoelasticity of the formed layers, it can be inferred that formed peptide layers of **native** hIAPP(20-29) and **Ac**-IAPP(20-29) have the highest viscoelasticity reflecting the capability of the formed peptide film to damp the inserted frequency more than the other systems containing **Am**-hIAPP(20-29) and **Ac-Am**-hIAPP(20-29) films.

To have better understanding about the viscoelastic properties of the formed peptidic films on the sensors the loss factor -Δ*D*/Δ*F* was calculated. In addition, by calculating the frequency, dissipation, and loss factor, it is possible to extract the data corresponding to viscoelasticity, and the *surface-induced conformation* of the attached monomer (see **Table 6-2**) (Hemmersam et al. 2005; Hemmersam et al. 2008).

Regarding the **native** hIAPP(20-29), the deposited film allocates considerable adsorbed mass, highest dissipation ΔD, and the highest value of the loss factor. At contact with positively charged SAM the **native** hIAPP(20-29) exposes its negative C-terminus to make electrostatic interaction. The loss factor of (0.3×10^{-6} Hz^{-1}) suggests a confirmation by which the monomer can easily dissipate the energy and therefore it would be plausible to consider a vertical conformation, while the positive N-terminus points to the medium above the substrate. However, electrostatic repulsion between positive N-termini of the **native** hIAPP(20-29) lessens the compact structure of the attached monomers. The loosely packed structures allow the water molecules to reside among the vertically attached monomers and consequently, dissipation increases. Therefore, it is reasonable to take a dangling monomer into consideration whose spatial conformation easily dissipates the energy.

The **Ac**-hIAPP(20-29) shows frequency about -50.38 (Hz) at the end of the experiment which implies the high amount of adsorbed mass (see **Table 6-2**). Interestingly, **Ac**-hIAPP which showed close value of adsorption to **native** hIAPP(20-29), possesses the least loss factor (0.17×10^{-6} Hz^{-1}). That is, the **Ac**-hIAPP(20-29) can dissipate less energy than the other peptidic monomers on the sensors and it may be visualized that **Ac**-hIAPP(20-29) monomer binds to the positively charged SAM by its *C-terminus*. In addition, lack of presence of positive *N-terminus* let the vertical monomers of the **Ac**-hIAPP(20-29) to tilt and get close to each other which causes a more compact structure to form which leads to decrease of amount of trapped water molecules and hereafter, the formed layer loses its ability to damp the inserted frequency.

It is seen that when the *C-terminus* of the hIAPP(20-29) becomes amidated, the electrostatic interactions are inhibited and the adsorption decreases dramatically, compared with **native**

hIAPP(20-29). The remaining adsorption may be the result of hydrogen bonds established between the peptide backbone or amino acids with positively charged SAM. According to loss factor which implies that the **Am**-hIAPP(20-29) has ability to dissipate the energy, a dangling conformation would be proposed, because, due to electrostatic repulsion between *N-terminus* and positively charged SAM, the **Am**-hIAPP(20-29) may bind to the surface via *C-terminal region*.

The **Ac-Am**-hIAPP(20-29) represents low amount of adsorption, and close values of low dissipation, and loss factor to the **Am**-hIAPP(20-29). Because of the net charge of zero and absence of any charged termini in **Ac-Am**-hIAPP(20-29), adsorption process may proceed via the hydrogen bonds established between the peptide backbone/amino acids and the positively charged SAM. According to the calculated dissipation, a thin film with low viscoelasticity can form. As **Am**-hIAPP(20-29) and **Ac-Am**-hIAPP(20-29) represent similar values of loss factors which are higher than **Ac**-hIAPP(20-29), it is also possible to consider that the **Ac-Am**-hIAPP(20-29) takes the dangling conformation in such way that it has ability to dissipate the energy.

Figure 6-5 c-d represents the AFM images of formed peptide films on the positively charged sensors. As is conspicuous, none of the peptides shows any considerable morphology.

6.3.2.3 Effect of COO^--terminated SAM

Adsorption dynamics of the hIAPP(20-29) with various termini at COO^--terminated SAM are represented in **Figure 6-6 a**. At the beginning of the injection of peptide solutions into the cells, a quick decrease in frequency value ΔF is observed indicating the mass deposition on the sensors. From this point on, frequency which is reflective of the affinity of the peptide to the negatively functionalized surface decreases. In the time course of injection, interestingly, the frequency value ΔF of the **Ac-**hIAPP(20-29) decreases gradually and shows more adsorption affinity than **Am-**hIAPP(20-29) which in spite of having positive charge state shows less adsorption affinity to the negatively functionalized SAM. **Native** and **Ac-Am**-hIAPP(20-29) represent strong adsorption trends which are reflected by remarkable decrease of frequency value (see **Table 6-3**).

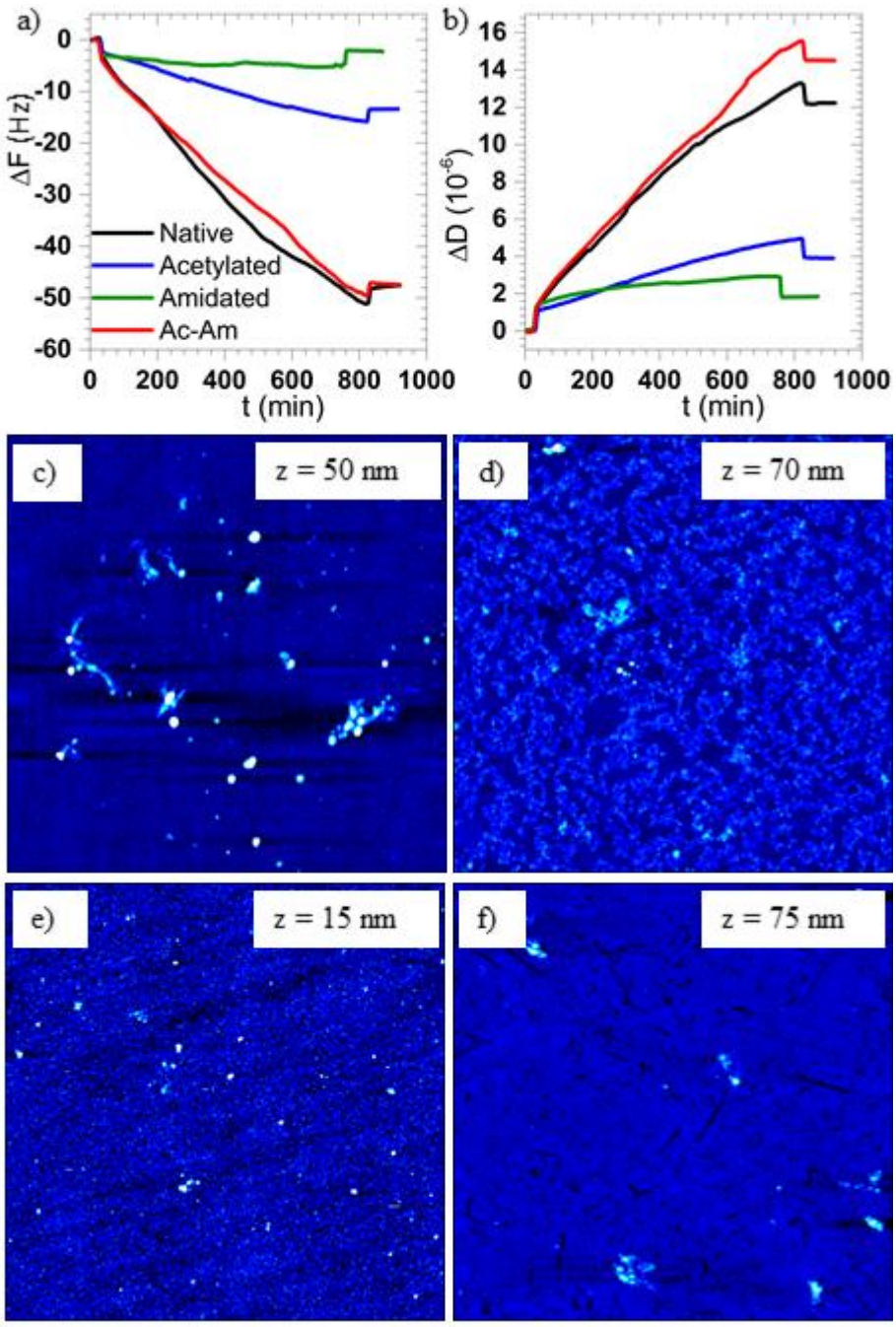

Figure 6-6. *Frequency shift, dissipation curves, and AFM images of various functionalized termini of hIAPP(20-29) after incubation at* ***COO***$^-$*-terminated Surface: a) frequency shift ΔF, b) dissipation ΔD. c)* ***native*** *hIAPP(20-29), d)* ***Ac****-hIAPP(20-29), e)* ***Am****-hIAPP(20-29), f)* ***Ac-Am****-hIAPP(20-29). Images have a size of 10 × 10 μm*^{2}*. The ranges of the z scales are given in the individual images.*

Table 6-3 *ΔF, ΔD, and -ΔD/ΔF values of the hIAPP(20-29) with various termini at contact with COO^--functionalized surface (the numbers were obtained at the end of the QCM-D measurements, i.e., after flushing with peptide-free buffer. All values have been determined for the 7th overtone.*

	Native hIAPP(20-29)	**Ac-hIAPP(20-29)**	**Am-hIAPP(20-29)**	**Ac-Am-hIAPP(20-29)**
ΔF (Hz)	**-47.95**	**-13.44**	**-2.28**	**-48.52**
ΔD (10^{-6})	**12.15**	**3.92**	**1.78**	**14.49**
-ΔD/ΔF (10^{-6} Hz^{-1})	**0.25**	**0.3**	**0.8**	**0.3**

As the N-terminus of the **native** hIAPP(20-29) has positive charge state (see **figure 6-1**), the driving force to bind to the negatively charged SAM may has electrostatic nature and electrostatic attraction between the *positive N-terminus* and COO^--functionalized SAM leads the adsorption.

Regarding the more tendency of **Ac**-hIAPP(20-29) than **Am**-hIAPP(20-29), another mechanism of adsorption can be proposed; instead of considering the electrostatically adsorbed peptidic monomers, it can be assumed that electrostatic interactions as a consequence of N- and C-terminus modification play negligible role in scenario of adsorption and aggregation. Since the adsorption of **Ac**-hIAPP(20-29) from its *negative C-terminus* is impossible (electrostatic repulsion), the proposed mechanism may lead via hydrogen bonding between the *acetylated N-terminal region* and COO^--terminated surface (in accordance with simulation surveys performed by Jiang *et al*. (Jiang et al. 2009) and Mo *et al*. (Mo et al. 2009)). Although the aforementioned mechanism

gives more importance to the hydrogen bonding than electrostatic interactions, the observed weak adsorption of **Am**-hIAPP(20-29) can possess electrostatic nature by which the adsorption proceeds on negatively charged SAM via electrostatic attraction between positive N-terminus and COO^--terminated SAM.

Here comes the question that why **Ac-Am**-hIAPP(20-29) with net charge of zero (**Ac-Am**) also represents the similar trend of adsorption as **native** hIAPP(20-29) has to the negatively charged SAM, despite not having any charged termini? As a matter of electrostatic interactions, it was expected to see considerable adsorption upon amidation, since the peptide gains the positive net charge (**Am**-hIAPP(20-29)), compared with **Ac**-hIAPP(20-29). On the other hand, when the both termini become modified by acetylation and amidation (**Ac-Am**-hIAPP(20-29)), it was expected to observe inconsiderable amount of adsorption. However, interestingly, the expectations were not the case and it seems that another mechanism leads the adsorption. Based on the observed adsorption dynamics on the OH-terminated SAM, on which the hydrogen bonding between *acetylated N-terminal region* of **Ac-Am**-hIAPP(20-29) was proposed (because when the C-terminus of the **native** hIAPP(20-29) became amidated (**Am**-hIAPP(20-29), no adsorption was observed) (see **6.3.2.1**), here, it may be the case where the **Ac-Am**-hIAPP(20-29) binds to the COO^--terminated SAM via *acetylated N-terminus*.

Dissipation behaviors of the different peptidic films are shown in **Figure 6-6 b**. At the beginning of the injection time, the dissipation increases which are the results of formation of a viscoelastic peptidic layer. In parallel with strong adsorption of **native** hIAPP(20-29) and **Ac-Am**-hIAPP(20-29)

to the negatively charged surface, significantly increased dissipations ΔD are observed (see **table 6-3**).

The high dissipation ΔD denotes the formation of highly viscoelastic peptidic layers through which the inserted frequency via oscillating quartz crystals gets frustrated. The remarkable enhancement in damping characteristics of the formed films can be the result of trapped water molecules which cause the peptide layer to possess higher damping characteristic (Hemmersam et al. 2005; Hemmersam et al. 2008). The calculated loss factor gives the ability to better analyze conformation of attached molecules on the surface.

The **native** hIAPP(20-29) represents high amount of adsorption, dissipation and loss factor. As it was proposed that the adsorption proceeds via attachment of the *positive N-terminus* of the hIAPP(20-29), according to high loss factor, it can be visualized that the **native** hIAPP(20-29) takes a vertical (dangling conformation) structure which can dissipate the energy.

Regarding the **Ac**-hIAPP(20-29), based on the aforementioned mechanism that hydrogen bonds lead the adsorption, high loss factor of **Ac**-hIAPP(20-29) could be reflective of forming a dangling conformation whose attachment is performed via *acetylated N-terminal region* and the C-terminus points to the medium.

In spite of the fact that **Am**-hIAPP(20-29) shows the least value of adsorption, the highest loss factor of which (0.8×10^{-6} Hz^{-1}) is reflective of forming a structure whose spatial conformation remarkably dissipates the energy. On the other hand, low amounts of adsorption and dissipation are reflective of forming a thin film with low viscoelasticity. To conclude, it is more plausible to visualize a low-density brush-like structure of **Am**-hIAPP(20-29) covering the negatively charged

surface whose attachment undergoes via electrostatic interaction between *positive N-terminus* and COO^--terminated SAM which leads to a vertically attached monomer.

The **Ac-Am**-hIAPP(20-29) represents high loss factor of 0.3 x 10^{-6} Hz^{-1}. Remembering the influence of OH-terminated SAM on adsorption of **Ac-Am**-hIAPP and considering the adsorption on COO^--terminated SAM from *acetylated N-terminsl region*, a dangling conformation on COO^--terminated SAM may be the most probable conformation for the **Ac-Am**-hIAPP(20-29).

Figure 6-6 c-f represents the AFM images of QCM-D after injection of various hIAPP(20-29)s onto negatively charged surfaces. From the AFM images (see **figure 6-6 c-f**) it can be observed that any mentionable morphology is not observed except for **native** IAPP which forms short protofibrils. As it was reported, hIAPP(20-29) is able to form mature fibrils upon incubation on freshly cleaved mica surface which is used as a negatively charged substrate (Hajiraissi et al. 2017). The proposed fibrillization mechanism was ascribed to the presence of positive N-terminus of the hIAPP(20-29) which based on electrostatic attraction between the positive N-terminus and negatively charged mica surface, the fibrillization proceeds (Hajiraissi et al. 2017). By employing hIAPP(1-37) and analyzing the dynamics of adsorption at contact with negatively charged SAM, it was revealed that amino acids whose charge states in PBS (pH 7.5) are positive and reside in N-terminal region can bind to negatively charged SAM and the C-terminal region which moves freely can establish β-sheets which lead to forming of mature fibrils (Hajiraissi et al. 2018). Therefore, the N-terminus in **native** hIAPP(20-29) would be able to bind to negatively charged SAM and consequently, short protofibrils form on the COO^--terminated SAM (see **figure 6-6 C**).

6.3.2.4 Effect of CH_3-terminated SAM

Figure 6-7 a-b represents the frequency values and dissipations curves of hIAPP(20-29) at contact with hydrophobic surface. As can be seen in **Figure 6-7 a**, during the injection of the peptides onto CH_3-terminated SAM, the frequency values decrease gradually. Frequency values of **native** hIAPP(20-29), **Ac**-hIAPP(20-29), and **Am**-hIAPP(20-29) follow close trends of adsorption, however, **Ac-Am**-hIAPP(20-29) shows more slowly trend. At the end of the experiment, when the cells were flushed with pure PBS, the all fragments show increase in frequency which is reflective of removing the unbound peptides from the surface. By calculated frequency changes (see **Table 6-4**), it is seen that **Ac-Am**-hIAPP(20-29) represents the least value of adsorption compared with **native** hIAPP(20-29), **Ac**-hIAPP(20-29), and **Am**-hIAPP(20-29).

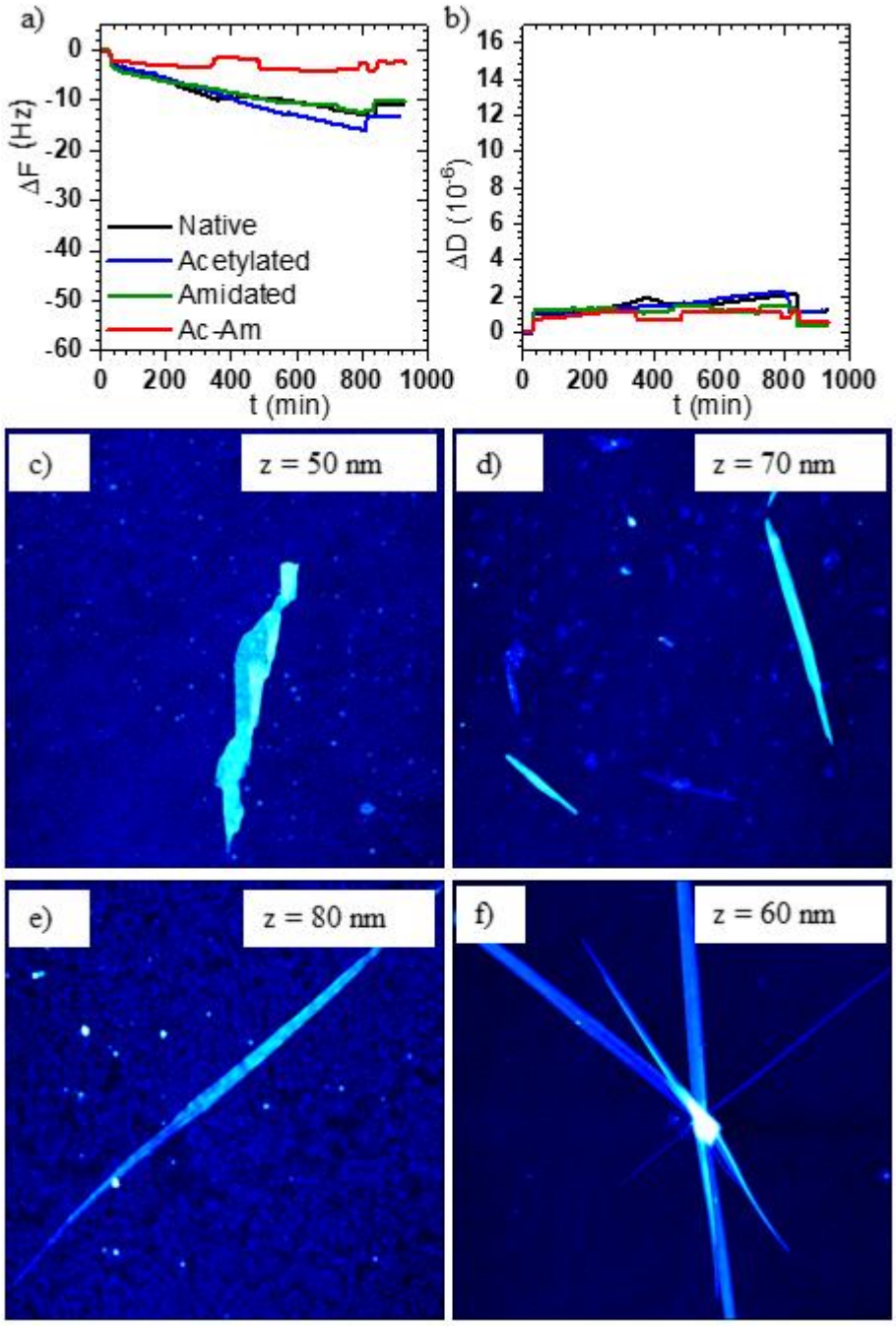

Figure 6-7. *Frequency shift, dissipation curves, and AFM images of various functionalized termini of hIAPP(20-29) after incubation at* ***CH_3****-terminated Surface: a) frequency shift ΔF, b) dissipation ΔD. c)* ***native*** *hIAPP(20-29), d)* ***Ac****-hIAPP(20-29), e)* ***Am****-hIAPP(20-29), f)* ***Ac-Am****-hIAPP(20-29). Images have a size of 10 × 10 μm^2. The ranges of the z scales are given in the individual images.*

Table 6-4 *ΔF, ΔD, and -ΔD/ΔF values of the hIAPP(20-29) with various termini at contact with CH_3-functionalized surface (the numbers were obtained at the end of the QCM-D measurements, i.e., after flushing with peptide-free buffer. All values have been determined for the 7th overtone.*

	Native hIAPP(20-29)	**Ac-hIAPP(20-29)**	**Am-hIAPP(20-29)**	**Ac-Am-hIAPP(20-29)**
ΔF (Hz)	**-10.68**	**-13.18**	**-9.97**	**-2.54**
ΔD (10^{-6})	**1.21**	**1.22**	**0.41**	**0.51**
-ΔD/ΔF (10^{-6} Hz^{-1})	**0.11**	**0.09**	**0.04**	**0.2**

Dissipation curves regarding the viscoelasticity of formed peptide films, were presented in **Figure 6-7 b**. At the beginning of the experiment a stable line is observed which is related to injection of peptide-free buffer. Upon injection of the peptide dissolved solution, the dissipation increases. At the end of the experiment, the cells are flushed with pure buffer solution and because of the flushing, the ΔD decreases which shows that unbounded monomers leave the surface of the sensors and the viscoelasticity decreases. Loss factors of different peptides show that the **Am**-hIAPP(20-29) on hydrophobic surface has the spatial conformation with lowest dissipation (0.04 x 10^{-6} Hz^{-1}) and the **Ac-Am**-hIAPP(20-29) has the highest value of dissipation (0.2 x 10^{-6} Hz^{-1}).

Figure 6-7 c-f represents the AFM images of four hIAPP(20-29) fragments at contact with CH_3-terminated quartz crystals. According to the images, two extends of aggregation can be observed. At one end lies **native** hIAPP(20-29) (**figure 6-7 c**) which represents a ribbon-like structure, and at the other end lies **Ac-Am**-hIAPP(20-29) (**figure 6-7 f**) with highly ordered and long ribbons

throughout the surface. In the middle, **Am-**hIAPP(20-29) peptide (**figure 6-7 e**) shows longer and more ordered ribbons than the **Ac-**hIAPP(20-29) (**figure 6-7 d**). Upon incubation on various surfaces, the hIAPP(20-29) showed different types of morphologies. The observed morphologies are of interest since at contact with negatively charged mica surface the monomer could self-assemble, while at contact with hydrophobic surface the monomer showed tendency to oligomeric structures with few short protofibrils (Hajiraissi et al. 2017).

By employing hIAPP(1-37) and injection onto CH_3-functionalized surface, the peptide showed the highest value of adsorption (Hajiraissi et al. 2018). According to Griffiths *et al.* and Mo *et al*. ,(Griffiths et al. 1995; Mo et al. 2009) it can be expected that hydrophobic interactions between *F, G, A, I, L* amino acids, whose positions are in the center of the native fragment, and surface give rise to peptide adsorption onto the surface. In the case of hIAPP(20-29), based on reported simulations, it was observed that hydrophobic amino acids in hIAPP(20-29) fragment represents parallel/antiparallel and in-register/out-of-register β-sheet structure (Griffiths et al. 1995; Mo et al. 2009). In accordance with Griffiths *et al.* (Griffiths et al. 1995) and , Mo *et al.* (Mo et al. 2009) it can be expected that hydrophobic interactions between hydrophobic amino acids, whose positions are in the center of the native fragment, and surface give rise to peptide adsorption onto the surface. Moreover, because of the position of the hydrophobic amino acids, monomers try to make a long structure which is the result of parallel/antiparallel, in-register/out-of-register β-sheet formation. However, due to possible hydrophobic interactions from various directions (Griffiths et al. 1995) and presence of positive N-terminus and negative C-terminus which may lead to electrical repulsion, a long ribbon-like structure forms (Griffiths et al. 1995; Mo et al. 2009). Upon modification of N- and C-termini of the native peptide by acetylation and amidation, the net

charge of the monomer becomes zero and it is not far from expectations that absence of electrical repulsion may facilitate the ordering and partitioning the **Ac-Am**-IAPP monomers leading to accumulation of monomers in which the presence of hydrophobic surface eases the aggregation of the monomers. In agreement with Jaikaran *et al.* (Jaikaran et al. 2001) it can be concluded that hydrophobic interactions are responsible to form aggregates and upon surface attachment, hydrogen bonds lead the β-sheet formation. The appearance of these aggregates is on the contrary to our previous results that IAPP(20-29) showed oligomeric and aggregated structures at hydrophobic supported mica surface (Hajiraissi et al. 2017) .

6.4 Conclusion

In this work, hIAPP(20-29) modified by *acetylation* and *amidation* was used to analyze both the effect of various charged SAMs and influence of N-, and C-Terminal modification on amyloid aggregation. Terminal modification of hIAPP(20-29) with various termini led to different charge states (negative, positive, and neutral). After extracting the data from fluorescence fluorimetry, all the fragments represent a sigmoidal curve and with similar trend and close intensities. It seems that presence of salt ion in solution lessens the amount of peptide-peptide interactions and based on AFM images, it seems that all fragments do not show any remarkable structure. At contact with hydrophobic surface, the native and modified IAPPs show potential to form fibrillar structures, with varying extents. It seems that upon acetylation, the acetylated monomers obtain potential to form short fibrils. Interestingly, after amidation and acetylation of N- and C-terminal, long self-assembled fibrils form. However, after exposure to hydrophilic, negative, and positive surfaces,

native, **Ac-**, and **Ac-Am-**IAPP monomers adsorb to the surfaces strongly and show high amount of adsorption. Interestingly, **Am-**IAPP represents the lowest amount of adsorption whose behavior is more surprising as this monomer with positive charge state shows the lowest amount of adsorption among the all types of peptides at contact with negatively charged surface.

Based on the observed AFM images and dynamics of the adsorption, it may be proposed that upon terminal modification, electrostatic interactions play minor role in adsorption and fibrillization. On the other hand, it seems that at contact with hydrophobic surface the hydrophobic interaction causes the hIAPP(20-29) to bind to the surface and hereafter the hydrogen bonding leads the fibrillization. It should be pointed out that by terminal modification the hIAPP(20-29) can vary its spatial conformation whose effect can be traced by different values of loss factor.

Chapter 7

Conclusion & Outlook

In this work IAPP as a fibrillogenic peptide was used to evaluate the aggregation and self-assembly of the peptide in both bulk and at contact with various model surfaces. As human variant of the IAPP is involved in T2DM and shows fibrillar self-assembly, it would be of interest to analyze the effects of various experimental conditions on the aggregation and fibrillization of the IAPP.

As in vivo the hIAPP experiences biological surfaces such as cell-membranes, the physicochemical surface properties have critical roles on the interactions undergoing at interface which lead to polymorphic structures of IAPP. As was mentioned earlier, the interactions at the interface are under control of not only bulk parameters (pH, temperature), but also surface properties such as hydrophobicity and hydrophilicity. The IAPP at pH 7.5 has net charge of +4 which is derived from protonation of Lys1, Arg11, His18 and N-terminal. The IAPP has also 14 hydrophobic amino acids which are responsible for hydrophobic interactions. It was found that the presence of various surfaces affects the aggregation and fibrillization of the IAPP as various interactions based on hydrophobic and electrostatic natures vary the structuring of the IAPP. By using QCM-D and fabricating various self-assembled monolayers, the hIAPP(1-37) showed the highest amount of adsorption when comes onto contact with hydrophobic SAM (CH_3-terninated). The significant adsorption is derived from the established hydrophobic interactions between the hydrophobic amino acids and hydrophobic SAM. Consequently, it seems that at contact with CH_3-terminated SAM, the hIAPP loses its ability to form amyloid fibrils and the fibrillization mechanism is retarded. On the other hand, COO^--functionalized SAM which serves as negatively charged surface, promoted the fibrillization and long fibrils are formed. In agreement with the previous works, it is assumed that positive amino acids of hIAPP which reside in N-terminal region are attracted to the

negatively charged surface by electrostatic interactions and amino acids in C-terminal region establish the β-sheet structures which lead to formation of long fibrils.

hIAPP(20-29) as the core fibrillogenic region of full length hIAPP was incubated on freshly cleaved mica in order to understand the effect of negatively charged surface. It was found that upon incubation on the mica surface for different time points, at the initial times of incubation the hIAPP(20-29) represents epitaxial growth which may be the consequence of interaction between positive N-terminus and negatively charged mica surface. At longer times of incubation, the hIAPP(20-29) represented various species of amyloid fibrils (straight, coiled, and ribbon-like). Interestingly, after incubation on hydrophobic hydrocarbon surface, the hIAPP(20-29) showed oligomeric structures and few short protofibrils.

In order to clarify the effect of charge states on the hIAPP(20-29), various terminal modifications were used to induce hIAPP(20-29) with net charges of neutral, negative, and positive and the aggregation and fibrillization of different peptides were investigated at contact with various self-assemble monolayers. On the contrary to the observed oligomeric structure along with significant adsorption on hydrophobic surface by hIAPP(20-29) and hIAPP(1-37), the all native, acetylated, amidated, and acetylated-amidated hIAPP(20-29) showed long ribbon-like morphologies and lesser amount of adsorption compared with adsorbed amounts on OH-, COO^--, and NH_2-terminated surfaces.

To sum up, physicochemical properties of the surface take the structuring and partitioning of the peptidic monomers of hIAPP under control and by changing the driving forces at the interface, various parts of the peptidic monomer are involved. As a complex structure, peptidic monomers

possess hydrophobic and hydrophilic characteristics and consequently, it is expected that upon exposure to the hydrophobic substrate, the IAPP exposes the residues with hydrophobic nature and upon exposure to the charged surfaces, the residues with opposite charge states align in front of the substrate at the interface.

In the context of hydrophobic surface, it was found that IAPP(1-37) has high propensity to adsorb which the adsorption originates mainly from hydrophobic interactions, while the rate of fibrillization is retarded. Interestingly, it was inferred that at contact with hydrophobic SAM in PBS (pH 7.5) and at temperature of 37°C, the hydrophobic residue (IAPP(20-29)) adsorbs and hydrogen bonds between the peptide backbones make the β-sheets which lead to formation of long ribbons.

In the context of electrostatic interactions, when the hIAPP(1-37) comes onto negatively charged SAM, fibrillization accelerates. Presence of positively charged surface which led to appearance of short fibrils may be the consequence of hydrogen bonding since according to positive charged states of the hIAPP(1-37) it was expected to see electrostatic repulsion between the monomer and positively charged SAM which was not the case. Intriguingly, by terminal modification of hIAPP(20-29), electrostatic interactions play minor roles in fibrillization of this hydrophobic residue and it seems that according to the nature of the surface (hydrophobic/hydrophilic) and peptide structure the potential of fibrillization varies.

In addition, by employing OH-terminated SAM it was seen that hIAPP(1-37) gains the ability to be fibrillizated which it may be the consequence of establishing the hydrogen bonds between the terminating OH groups and the peptide termini. On the other hand, when the N-terminus or both N- and C- termini of the hIAPP(20-29) become acetylated and amidated, instead of observing

fibrillar entities, remarkable adsorptions are seen which may originate from the hydrogen bonds between the peptidic monomer and the OH-terminated surface.

As the charge states of the peptidic monomer varies in different solutions, it would be of interest to used solutions with different pHs in order to analyze the influence of the charge state on not only aggregation, but also on fibrillization of the peptide in both bulk state and at contact with surfaces with varying hydrophobicity and hydrophilicity. As the type of the buffer solution with varying ionic strength changes deby length, it would be also interesting to investigate the aggregation and fibrillization of the peptide. In addition to the aforementioned parameters, temperature also plays a pivotal role whose variation can certainly change the thermodynamics of the system towards fibrillization. As the QCM-D has the ability to perform the experiment in dynamic and static modes, using different self-assembled monolayers can also give information about the dynamics of adsorption in different solutions and at different temperatures.

References

Abedini A, Raleigh DP (2005) The role of His-18 in amyloid formation by human islet amyloid polypeptide. Biochemistry 44:16284–16291. doi: 10.1021/bi051432v

Abedini A, Plesner A, Cao P, Ridgway Z, Zhang J, Tu L-H, Middleton CT, Chao B, Sartori DJ, Meng F, Wang H, Wong AG, Zanni MT, Verchere CB, Raleigh DP, Schmidt AM (2016) Time-resolved studies define the nature of toxic IAPP intermediates, providing insight for anti-amyloidosis therapeutics. Elife 5. doi: 10.7554/eLife.12977

Alberts B (2002) Molecular biology of the cell, 4. ed. Garland Science, New York, NY

Andrews MN, Winter R (2011) Comparing the structural properties of human and rat islet amyloid polypeptide by MD computer simulations. Biophysical Chemistry 156:43–50. doi: 10.1016/j.bpc.2010.12.007

Apostolidou M, Jayasinghe SA, Langen R (2008) Structure of alpha-helical membrane-bound human islet amyloid polypeptide and its implications for membrane-mediated misfolding. J Biol Chem 283:17205–17210. doi: 10.1074/jbc.M801383200

Arnau A, Sogorb T, Jiménez Y (2002) Circuit for continuous motional series resonant frequency and motional resistance monitoring of quartz crystal resonators by parallel capacitance compensation. Review of Scientific Instruments 73:2724–2737. doi: 10.1063/1.1484254

Arosio P, Knowles TPJ, Linse S (2015) On the lag phase in amyloid fibril formation. Phys Chem Chem Phys 17:7606–7618. doi: 10.1039/C4CP05563B

BACHEM Peptide Calculator. http://www.bachem.com/service-support/peptide-calculator/

Bhak G-B, Choe Y-J, Paik S-R (2009) Mechanism of amyloidogenesis: nucleation-dependent fibrillation versus double-concerted fibrillation. BMB Reports 42:541–551. doi: 10.5483/BMBRep.2009.42.9.541

Biancalana M, Koide S (2010) Molecular mechanism of Thioflavin-T binding to amyloid fibrils. Biochim Biophys Acta 1804:1405–1412. doi: 10.1016/j.bbapap.2010.04.001

Binnig, Quate, Gerber (1986) Atomic force microscope. Phys Rev Lett 56:930–933. doi: 10.1103/physrevlett.56.930

Blackstock JC (1989) Guide to Biochemistry, 1. Aufl. Elsevier Reference Monographs, s.l.

Bohinski RC (1987) Modern Concepts in biochemistry, 5. ed. Allyn and Bacon, Boston Mass

Bremer MGEG, Duval J, Norde W, Lyklema J (2004) Electrostatic interactions between immunoglobulin (IgG) molecules and a charged sorbent. Colloids and Surfaces A: Physicochemical and Engineering Aspects 250:29–42. doi: 10.1016/j.colsurfa.2004.05.026

Brockwell DJ, Radford SE (2007) Intermediates: ubiquitous species on folding energy landscapes? Curr Opin Struct Biol 17:30–37. doi: 10.1016/j.sbi.2007.01.003

Brunauer S, Emmett PH, Teller E (1938) Adsorption of Gases in Multimolecular Layers. J. Am. Chem. Soc. 60:309–319. doi: 10.1021/ja01269a023

Bryngelson JD, Onuchic JN, Socci ND, Wolynes PG (1995) Funnels, pathways, and the energy landscape of protein folding: a synthesis. Proteins 21:167–195. doi: 10.1002/prot.340210302

Buell AK, Galvagnion C, Gaspar R, Sparr E, Vendruscolo M, Knowles TPJ, Linse S, Dobson CM (2014) Solution conditions determine the relative importance of nucleation and growth processes in -synuclein aggregation. J Mol Biol 111:7671–7676. doi: 10.1073/pnas.1315346111

Butt H-J, Graf K, Kappl M (2003) Physics and Chemistry of Interfaces. Wiley-VCH Verlag GmbH & Co. KGaA, Weinheim, FRG

Butterfield SM, Lashuel HA (2010) Amyloidogenic protein-membrane interactions: mechanistic insight from model systems. Angew. Chem. Int. Ed. 49:5628–5654. doi: 10.1002/anie.200906670

Cabaleiro-Lago C, Lynch I, Dawson KA, Linse S (2010) Inhibition of IAPP and IAPP(20-29) fibrillation by polymeric nanoparticles. Langmuir 26:3453–3461. doi: 10.1021/la902980d

Caillon L, Lequin O, Khemtémourian L (2013) Evaluation of membrane models and their composition for islet amyloid polypeptide-membrane aggregation. Biochim Biophys Acta 1828:2091–2098. doi: 10.1016/j.bbamem.2013.05.014

Caillon L, Hoffmann ARF, Botz A, Khemtemourian L (2016) Molecular Structure, Membrane Interactions, and Toxicity of the Islet Amyloid Polypeptide in Type 2 Diabetes Mellitus. J Diabetes Res 2016:5639875. doi: 10.1155/2016/5639875

Cao P, Abedini A, Raleigh DP (2012) Aggregation of islet amyloid polypeptide: from physical chemistry to cell biology. Curr Opin Struct Biol 23:82–89. doi: 10.1016/j.sbi.2012.11.003

Cappella B, Dietler G (1999) Force-distance curves by atomic force microscopy. Surface Science Reports 34:1–104. doi: 10.1016/S0167-5729(99)00003-5

Chatelier RC, Minton AP (1996) Adsorption of globular proteins on locally planar surfaces: models for the effect of excluded surface area and aggregation of adsorbed protein on adsorption equilibria. Biophys J 71:2367–2374. doi: 10.1016/S0006-3495(96)79430-4

Chiti F, Dobson CM (2006) Protein misfolding, functional amyloid, and human disease. Annu Rev Biochem 75:333–366. doi: 10.1146/annurev.biochem.75.101304.123901

Cohen SIA, Linse S, Luheshi LM, Hellstrand E, White DA, Rajah L, Otzen DE, Vendruscolo M, Dobson CM, Knowles TPJ (2013) Proliferation of amyloid- 42 aggregates occurs through a secondary nucleation mechanism. European Journal of Biochemistry 110:9758–9763. doi: 10.1073/pnas.1218402110

Collins KD, Washabaugh MW (1985) The Hofmeister effect and the behaviour of water at interfaces. Quart. Rev. Biophys. 18:323. doi: 10.1017/S0033583500005369

Dąbrowski A (2001) Adsorption — from theory to practice. Adv Colloid Interface Sci 93:135–224. doi: 10.1016/S0001-8686(00)00082-8

Daly SM, Przybycien TM, Tilton RD (2003) Coverage-Dependent Orientation of Lysozyme Adsorbed on Silica. Langmuir 19:3848–3857. doi: 10.1021/la026690x

Demanèche S, Chapel J-P, Monrozier LJ, Quiquampoix H (2009) Dissimilar pH-dependent adsorption features of bovine serum albumin and alpha-chymotrypsin on mica probed by AFM. Colloids Surf B Biointerfaces 70:226–231. doi: 10.1016/j.colsurfb.2008.12.036

Dill KA, Chan HS (1997) From Levinthal to pathways to funnels. Nat Struct Mol Biol 4:10–19. doi: 10.1038/nsb0197-10

Dixon MC (2008) Quartz crystal microbalance with dissipation monitoring: enabling real-time characterization of biological materials and their interactions. J Biomol Tech 19:151–158

Dobson CM (2001) The structural basis of protein folding and its links with human disease. Philos Trans R Soc Lond , B, Biol Sci 356:133–145. doi: 10.1098/rstb.2000.0758

Domanov YA, Kinnunen PKJ (2008) Islet amyloid polypeptide forms rigid lipid-protein amyloid fibrils on supported phospholipid bilayers. J Mol Biol 376:42–54. doi: 10.1016/j.jmb.2007.11.077

Doran TM, Kamens AJ, Byrnes NK, Nilsson BL (2012) Role of amino acid hydrophobicity, aromaticity, and molecular volume on IAPP(20-29) amyloid self-assembly. Proteins 80:1053–1065. doi: 10.1002/prot.24007

Dupuis NF, Wu C, Shea J-E, Bowers MT (2009) Human islet amyloid polypeptide monomers form ordered beta-hairpins: a possible direct amyloidogenic precursor. J. Am. Chem. Soc. 131:18283–18292. doi: 10.1021/ja903814q

Engel MFM (2009) Membrane permeabilization by Islet Amyloid Polypeptide. Chem Phys Lipids 160:1–10. doi: 10.1016/j.chemphyslip.2009.03.008

Engel MFM, Khemtémourian L, Kleijer CC, Meeldijk HJD, Jacobs J, Verkleij AJ, Kruijff B de, Killian JA, Höppener JWM (2008) Membrane damage by human islet amyloid polypeptide through fibril growth at the membrane. Proc Natl Acad Sci U S A 105:6033–6038. doi: 10.1073/pnas.0708354105

Erbil HY (2006) Surface Chemistry. Blackwell Publishing Ltd, Oxford, UK

Fabian H, Naumann D (eds) (2012) Protein Folding and Misfolding: Shining Light by Infrared Spectroscopy. Biological and Medical Physics, Biomedical Engineering. Springer-Verlag Berlin Heidelberg, Berlin, Heidelberg

Flemming RG, Murphy CJ, Abrams GA, Goodman SL, Nealey PF (1999) Effects of synthetic micro- and nano-structured surfaces on cell behavior. Biomaterials 20:573–588. doi: 10.1016/S0142-9612(98)00209-9

Freire S, Araujo MH de, Al-Soufi W, Novo M (2014) Photophysical study of Thioflavin T as fluorescence marker of amyloid fibrils. Dyes and Pigments 110:97–105. doi: 10.1016/j.dyepig.2014.05.004

Gazit E (2002) A possible role for pi-stacking in the self-assembly of amyloid fibrils. FASEB J 16:77–83. doi: 10.1096/fj.01-0442hyp

Goldsbury C, Kistler J, Aebi U, Arvinte T, Cooper GJ (1999) Watching amyloid fibrils grow by time-lapse atomic force microscopy. J Mol Biol 285:33–39. doi: 10.1006/jmbi.1998.2299

Goldsbury C, Goldie K, Pellaud J, Seelig J, Frey P, Müller SA, Kistler J, Cooper GJ, Aebi U (2000) Amyloid fibril formation from full-length and fragments of amylin. J Struct Biol 130:352–362. doi: 10.1006/jsbi.2000.4268

Goldsbury C, Baxa U, Simon MN, Steven AC, Engel A, Wall JS, Aebi U, Müller SA (2011) Amyloid structure and assembly: insights from scanning transmission electron microscopy. J Struct Biol 173:1–13. doi: 10.1016/j.jsb.2010.09.018

Goldsbury CS, Cooper GJ, Goldie KN, Müller SA, Saafi EL, Gruijters WT, Misur MP, Engel A, Aebi U, Kistler J (1997) Polymorphic fibrillar assembly of human amylin. J Struct Biol 119:17–27. doi: 10.1006/jsbi.1997.3858

Green J, Goldsbury C, Mini T, Sunderji S, Frey P, Kistler J, Cooper G, Aebi U (2003) Full-length Rat Amylin Forms Fibrils Following Substitution of Single Residues from Human Amylin. J Mol Biol 326:1147–1156. doi: 10.1016/S0022-2836(02)01377-3

Green JD, Kreplak L, Goldsbury C, Li Blatter X, Stolz M, Cooper GS, Seelig A, Kistler J, Aebi U (2004) Atomic force microscopy reveals defects within mica supported lipid bilayers induced by the amyloidogenic human amylin peptide. J Mol Biol 342:877–887. doi: 10.1016/j.jmb.2004.07.052

Griffiths JM, Ashburn TT, Auger M, Costa PR, Griffin RG, Lansbury PT (1995) Rotational Resonance Solid-State NMR Elucidates a Structural Model of Pancreatic Amyloid. J. Am. Chem. Soc. 117:3539–3546. doi: 10.1021/ja00117a023

Gross L, Mohn F, Moll N, Liljeroth P, Meyer G (2009) The chemical structure of a molecule resolved by atomic force microscopy. Science 325:1110–1114. doi: 10.1126/science.1176210

Hajiraissi R, Giner I, Grundmeier G, Keller A (2017) Self-Assembly, Dynamics, and Polymorphism of hIAPP(20-29) Aggregates at Solid-Liquid Interfaces. Langmuir 33:372–381. doi: 10.1021/acs.langmuir.6b03288

Hajiraissi R, Hanke M, Yang Y, Duderija B, Gonzalez Orive A, Grundmeier G, Keller A (2018) Adsorption and Fibrillization of Islet Amyloid Polypeptide at Self-Assembled Monolayers Studied by QCM-D, AFM, and PM-IRRAS. Langmuir 34:3517–3524. doi: 10.1021/acs.langmuir.7b03626

Hans-Jürgen Butt (2003) Liquid Surfaces. In: Butt H-J, Graf K, Kappl M (eds) Physics and Chemistry of Interfaces. Wiley-VCH Verlag GmbH & Co. KGaA, Weinheim, FRG, pp 4–25

Hauser CAE, Maurer-Stroh S, Martins IC (2014) Amyloid-based nanosensors and nanodevices. Chem Soc Rev 43:5326–5345. doi: 10.1039/C4CS00082J

Hemmersam AG, Foss M, Chevallier J, Besenbacher F (2005) Adsorption of fibrinogen on tantalum oxide, titanium oxide and gold studied by the QCM-D technique. Colloids Surf B Biointerfaces 43:208–215. doi: 10.1016/j.colsurfb.2005.04.007

Hemmersam AG, Rechendorff K, Foss M, Sutherland DS, Besenbacher F (2008) Fibronectin adsorption on gold, Ti-, and Ta-oxide investigated by QCM-D and RSA modelling. J Colloid Interface Sci 320:110–116. doi: 10.1016/j.jcis.2007.11.047

Higham CE, Hull RL, Lawrie L, Shennan KIJ, Morris JF, Birch NP, Docherty K, Clark A (2000) Processing of synthetic pro-islet amyloid polypeptide (proIAPP) 'amylin' by recombinant prohormone convertase enzymes, PC2 and PC3, in vitro. European Journal of Biochemistry 267:4998–5004. doi: 10.1046/j.1432-1327.2000.01548.x

Hofmeister F (1888) Zur Lehre von der Wirkung der Salze. Archiv f. experiment. Pathol. u. Pharmakol 24:247–260. doi: 10.1007/BF01918191

Hook F, Rodahl M, Kasemo B, Brzezinski P (1998) Structural changes in hemoglobin during adsorption to solid surfaces: Effects of pH, ionic strength, and ligand binding. J Biol Chem 95:12271–12276. doi: 10.1073/pnas.95.21.12271

Huie JC (2003) Guided molecular self-assembly: a review of recent efforts. Smart Mater. Struct. 12:264–271. doi: 10.1088/0964-1726/12/2/315

Israelachvili JN (2011) Intermolecular and surface forces, 3. ed. Academic Press, Burlington, MA

Jahn TR, Radford SE (2005) The Yin and Yang of protein folding. FEBS Journal 272:5962–5970. doi: 10.1111/j.1742-4658.2005.05021.x

Jahn TR, Radford SE (2008) Folding versus aggregation: polypeptide conformations on competing pathways. Arch Biochem Biophys 469:100–117. doi: 10.1016/j.abb.2007.05.015

Jaikaran ETAS, Higham CE, Serpell LC, Zurdo J, Gross M, Clark A, Fraser PE (2001) Identification of a novel human islet amyloid polypeptide β-sheet domain and factors influencing fibrillogenesis. J Mol Biol 308:515–525. doi: 10.1006/jmbi.2001.4593

Janshoff A, Galla H-J, Steinem C (2000) Piezoelectric Mass-Sensing Devices as Biosensors—An Alternative to Optical Biosensors? Angew. Chem. Int. Ed. 39:4004–4032. doi: 10.1002/1521-3773(20001117)39:22<4004:AID-ANIE4004>3.0.CO;2-2

Jayasinghe SA, Langen R (2005) Lipid membranes modulate the structure of islet amyloid polypeptide. Biochemistry 44:12113–12119. doi: 10.1021/bi050840w

Jayasinghe SA, Langen R (2007) Membrane interaction of islet amyloid polypeptide. Biochim Biophys Acta 1768:2002–2009. doi: 10.1016/j.bbamem.2007.01.022

Jeworrek C, Hollmann O, Steitz R, Winter R, Czeslik C (2009) Interaction of IAPP and insulin with model interfaces studied using neutron reflectometry. Biophys J 96:1115–1123. doi: 10.1016/j.bpj.2008.11.006

Jiang P, Xu W, Mu Y (2009) Amyloidogenesis abolished by proline substitutions but enhanced by lipid binding. PLoS Comput Biol 5:e1000357. doi: 10.1371/journal.pcbi.1000357

JPK A practical guide to AFM force spectroscopy and data analysis. https://www.jpk.com/app-technotes-img/AFM/pdf/jpk-tech-force-spectroscopy.14-2.pdf

Kajava AV, Aebi U, Steven AC (2005) The parallel superpleated beta-structure as a model for amyloid fibrils of human amylin. J Mol Biol 348:247–252. doi: 10.1016/j.jmb.2005.02.029

Karlsson M, Carlsson U (2005) Protein adsorption orientation in the light of fluorescent probes: mapping of the interaction between site-directly labeled human carbonic anhydrase II and silica nanoparticles. Biophys J 88:3536–3544. doi: 10.1529/biophysj.104.054809

Kayed R, Sokolov Y, Edmonds B, McIntire TM, Milton SC, Hall JE, Glabe CG (2004) Permeabilization of lipid bilayers is a common conformation-dependent activity of soluble amyloid oligomers in protein misfolding diseases. J Biol Chem 279:46363–46366. doi: 10.1074/jbc.C400260200

Keller A, Fritzsche M, Yu Y-P, Liu Q, Li Y-M, Dong M, Besenbacher F (2011a) Influence of hydrophobicity on the surface-catalyzed assembly of the islet amyloid polypeptide. ACS Nano 5:2770–2778. doi: 10.1021/nn1031998

Keller A, Fritzsche M, Ogaki R, Bald I, Facsko S, Dong M, Kingshott P, Besenbacher F (2011b) Tuning the hydrophobicity of mica surfaces by hyperthermal Ar ion irradiation. The Journal of Chemical Physics 134:104705. doi: 10.1063/1.3561292

Knight JD, Miranker AD (2004) Phospholipid catalysis of diabetic amyloid assembly. J Mol Biol 341:1175–1187. doi: 10.1016/j.jmb.2004.06.086

Knight JD, Hebda JA, Miranker AD (2006) Conserved and cooperative assembly of membrane-bound alpha-helical states of islet amyloid polypeptide. Biochemistry 45:9496–9508. doi: 10.1021/bi060579z

Knowles TPJ, Mezzenga R (2016) Amyloid Fibrils as Building Blocks for Natural and Artificial Functional Materials. Adv Mater Weinheim 28:6546–6561. doi: 10.1002/adma.201505961

Kreplak L, Aebi U (2006) From the Polymorphism of Amyloid Fibrils to their Assembly Mechanism and Cytotoxicity. In: Fibrous Proteins: Amyloids, Prions and Beta Proteins, vol 73. Elsevier, pp 217–233

Kurrat R, Ramsden JJ, Prenosil JE (1994) Kinetic model for serum albumin adsorption : experimental verification. Faraday Trans. 90:587. doi: 10.1039/FT9949000587

Langmuir I (1918) THE ADSORPTION OF GASES ON PLANE SURFACES OF GLASS, MICA AND PLATINUM. J. Am. Chem. Soc. 40:1361–1403. doi: 10.1021/ja02242a004

Lee YS (ed) (2011) Self-Assembly and Nanotechnology Systems. John Wiley & Sons, Inc, Hoboken, NJ, USA

Li SC, Goto NK, Williams KA, Deber CM (1996) Alpha-helical, but not beta-sheet, propensity of proline is determined by peptide environment. Proceedings of the National Academy of Sciences 93:6676–6681. doi: 10.1073/pnas.93.13.6676

Lin Y-C, Petersson EJ, Fakhraai Z (2014) Surface Effects Mediate Self-Assembly of Amyloid-β Peptides. ACS Nano 8:10178–10186. doi: 10.1021/nn5031669

Lopes DHJ, Meister A, Gohlke A, Hauser A, Blume A, Winter R (2007) Mechanism of islet amyloid polypeptide fibrillation at lipid interfaces studied by infrared reflection absorption spectroscopy. Biophys J 93:3132–3141. doi: 10.1529/biophysj.107.110635

Lord MS, Foss M, Besenbacher F (2010) Influence of nanoscale surface topography on protein adsorption and cellular response. Nano Today 5:66–78. doi: 10.1016/j.nantod.2010.01.001

Love JC, Estroff LA, Kriebel JK, Nuzzo RG, Whitesides GM (2005) Self-assembled monolayers of thiolates on metals as a form of nanotechnology. Chem Rev 105:1103–1169. doi: 10.1021/cr0300789

Madine J, Jack E, Stockley PG, Radford SE, Serpell LC, Middleton DA (2008) Structural insights into the polymorphism of amyloid-like fibrils formed by region 20-29 of amylin revealed by solid-state NMR and X-ray fiber diffraction. J. Am. Chem. Soc. 130:14990–15001. doi: 10.1021/ja802483d

Marek PJ, Patsalo V, Green DF, Raleigh DP (2012) Ionic strength effects on amyloid formation by amylin are a complicated interplay among Debye screening, ion selectivity, and Hofmeister effects. Biochemistry 51:8478–8490. doi: 10.1021/bi300574r

Milanesi L, Sheynis T, Xue W-F, Orlova EV, Hellewell AL, Jelinek R, Hewitt EW, Radford SE, Saibil HR (2012) Direct three-dimensional visualization of membrane disruption by amyloid fibrils. Proceedings of the National Academy of Sciences 109:20455–20460. doi: 10.1073/pnas.1206325109

Minton AP (2000) Effects of excluded surface area and adsorbate clustering on surface adsorption of proteins. Biophysical Chemistry 86:239–247. doi: 10.1016/S0301-4622(00)00151-4

Minton AP (2001) Effects of Excluded Surface Area and Adsorbate Clustering on Surface Adsorption of Proteins. II. Kinetic Models. Biophys J 80:1641–1648. doi: 10.1016/S0006-3495(01)76136-X

Mitragotri S, Lahann J (2009) Physical approaches to biomaterial design. Nat Mater 8:15–23. doi: 10.1038/nmat2344

Mo Y, Lu Y, Wei G, Derreumaux P (2009) Structural diversity of the soluble trimers of the human amylin(20-29) peptide revealed by molecular dynamics simulations. The Journal of Chemical Physics 130:125101. doi: 10.1063/1.3097982

Moriarty DF, Raleigh DP (1999) Effects of sequential proline substitutions on amyloid formation by human amylin20-29. Biochemistry 38:1811–1818. doi: 10.1021/bi981658g

Mostaert AS, Higgins MJ, Fukuma T, Rindi F, Jarvis SP (2006) Nanoscale mechanical characterisation of amyloid fibrils discovered in a natural adhesive. J Biol Phys 32:393–401. doi: 10.1007/s10867-006-9023-y

Murphy RM (2007) Kinetics of amyloid formation and membrane interaction with amyloidogenic proteins. Biochim Biophys Acta 1768:1923–1934. doi: 10.1016/j.bbamem.2006.12.014

Nakanishi K, Sakiyama T, Imamura K (2001) On the adsorption of proteins on solid surfaces, a common but very complicated phenomenon. Journal of Bioscience and Bioengineering 91:233–244. doi: 10.1016/S1389-1723(01)80127-4

Nanga RPR, Brender JR, Xu J, Hartman K, Subramanian V, Ramamoorthy A (2009) Three-dimensional structure and orientation of rat islet amyloid polypeptide protein in a membrane environment by solution NMR spectroscopy. J. Am. Chem. Soc. 131:8252–8261. doi: 10.1021/ja9010095

Nanga RPR, Brender JR, Vivekanandan S, Ramamoorthy A (2011) Structure and membrane orientation of IAPP in its natively amidated form at physiological pH in a membrane environment. Biochim Biophys Acta 1808:2337–2342. doi: 10.1016/j.bbamem.2011.06.012

Noinville S, Bruston F, El Amri C, Baron D, Nicolas P (2003) Conformation, Orientation, and Adsorption Kinetics of Dermaseptin B2 onto Synthetic Supports at Aqueous/Solid Interface. Biophys J 85:1196–1206. doi: 10.1016/S0006-3495(03)74555-X

Norde W (1996) Driving forces for protein adsorption at solid surfaces. Macromol. Symp. 103:5–18. doi: 10.1002/masy.19961030104

Norde W (2008) My voyage of discovery to proteins in flatland …and beyond. Colloids Surf B Biointerfaces 61:1–9. doi: 10.1016/j.colsurfb.2007.09.029

O'Sullivan CK, Guilbault GG (1999) Commercial quartz crystal microbalances – theory and applications. Biosensors and Bioelectronics 14:663–670. doi: 10.1016/S0956-5663(99)00040-8

Ouberai MM, Xu K, Welland ME (2014) Effect of the interplay between protein and surface on the properties of adsorbed protein layers. Biomaterials 35:6157–6163. doi: 10.1016/j.biomaterials.2014.04.012

Pauling L, Corey RB, Branson HR (1951) The structure of proteins: Two hydrogen-bonded helical configurations of the polypeptide chain. Proceedings of the National Academy of Sciences 37:205–211. doi: 10.1073/pnas.37.4.205

Pillay K, Govender P (2013) Amylin uncovered: a review on the polypeptide responsible for type II diabetes. Biomed Res Int 2013:826706. doi: 10.1155/2013/826706

Rabe M, Verdes D, Rankl M, Artus GRJ, Seeger S (2007) A comprehensive study of concepts and phenomena of the nonspecific adsorption of beta-lactoglobulin. Chemphyschem 8:862–872. doi: 10.1002/cphc.200600710

Rabe M, Verdes D, Zimmermann J, Seeger S (2008) Surface organization and cooperativity during nonspecific protein adsorption events. J Phys Chem B 112:13971–13980. doi: 10.1021/jp804532v

Rabe M, Verdes D, Seeger S (2011) Understanding protein adsorption phenomena at solid surfaces. Adv Colloid Interface Sci 162:87–106. doi: 10.1016/j.cis.2010.12.007

Rechendorff K, Hovgaard MB, Foss M, Zhdanov VP, Besenbacher F (2006) Enhancement of protein adsorption induced by surface roughness. Langmuir 22:10885–10888. doi: 10.1021/la0621923

Reches M, Gazit E (2003) Casting metal nanowires within discrete self-assembled peptide nanotubes. Science 300:625–627. doi: 10.1126/science.1082387

Roiter Y, Minko S (2005) AFM single molecule experiments at the solid-liquid interface: in situ conformation of adsorbed flexible polyelectrolyte chains. J. Am. Chem. Soc. 127:15688–15689. doi: 10.1021/ja0558239

Rustenbeck I, Matthies A, Lenzen S (1994) Lipid composition of glucose-stimulated pancreatic islets and insulin-secreting tumor cells. Lipids 29:685–692. doi: 10.1007/BF02538912
Sabaté R, Espargaró A, Groot NS de, Valle-Delgado JJ, Fernàndez-Busquets X, Ventura S (2010) The role of protein sequence and amino acid composition in amyloid formation: scrambling and backward reading of IAPP amyloid fibrils. J Mol Biol 404:337–352. doi: 10.1016/j.jmb.2010.09.052
Sauerbrey G (1959) Verwendung von Schwingquarzen zur Wgung dnner Schichten und zur Mikrowgung. Z. Physik 155:206–222. doi: 10.1007/BF01337937
Saunders R, Deane CM (2010) Synonymous codon usage influences the local protein structure observed. Nucleic Acids Res 38:6719–6728. doi: 10.1093/nar/gkq495
Sawaya MR, Sambashivan S, Nelson R, Ivanova MI, Sievers SA, Apostol MI, Thompson MJ, Balbirnie M, Wiltzius JJW, McFarlane HT, Madsen AØ, Riekel C, Eisenberg D (2007) Atomic structures of amyloid cross-beta spines reveal varied steric zippers. Nature 447:453–457. doi: 10.1038/nature05695
Schaaf P, Talbot J (1989) Surface exclusion effects in adsorption processes. The Journal of Chemical Physics 91:4401–4409. doi: 10.1063/1.456768
Schaaf P, Voegel J-C, Senger B (2000) From Random Sequential Adsorption to Ballistic Deposition: A General View of Irreversible Deposition Processes. J Phys Chem B 104:2204–2214. doi: 10.1021/jp9933065
Scopelliti PE, Borgonovo A, Indrieri M, Giorgetti L, Bongiorno G, Carbone R, Podestà A, Milani P (2010) The effect of surface nanometre-scale morphology on protein adsorption. PLoS ONE 5:e11862. doi: 10.1371/journal.pone.0011862
Scrocchi LA, Ha K, Chen Y, Wu L, Wang F, Fraser PE (2003) Identification of minimal peptide sequences in the (8–20) domain of human islet amyloid polypeptide involved in fibrillogenesis. J Struct Biol 141:218–227. doi: 10.1016/S1047-8477(02)00630-5
Seidel A (ed) (2008) Characterization analysis of polymers. Wiley, Hoboken, NJ
Shen L, Adachi T, Vanden Bout D, Zhu X-Y (2012) A Mobile Precursor Determines Amyloid-β Peptide Fibril Formation at Interfaces. J. Am. Chem. Soc. 134:14172–14178. doi: 10.1021/ja305398f
Shezad K, Zhang K, Hussain M, Dong H, He C, Gong X, Xie X, Zhu J, Shen L (2016) Surface Roughness Modulates Diffusion and Fibrillation of Amyloid-β Peptide. Langmuir 32:8238–8244. doi: 10.1021/acs.langmuir.6b01756
Sittel K, Rouse PE, Bailey ED (1954) Method for Determining the Viscoelastic Properties of Dilute Polymer Solutions at Audio-Frequencies. Journal of Applied Physics 25:1312–1320. doi: 10.1063/1.1721552
Sparr E, Engel MFM, Sakharov DV, Sprong M, Jacobs J, Kruijff B de, Höppener JWM, Killian JA (2004) Islet amyloid polypeptide-induced membrane leakage involves uptake of lipids by forming amyloid fibers. FEBS Lett 577:117–120. doi: 10.1016/j.febslet.2004.09.075
Stefani M (2008) Protein folding and misfolding on surfaces. Int J Mol Sci 9:2515–2542. doi: 10.3390/ijms9122515
Stolz M, Stoffler D, Aebi U, Goldsbury C (2000) Monitoring biomolecular interactions by time-lapse atomic force microscopy. J Struct Biol 131:171–180. doi: 10.1006/jsbi.2000.4301
Tenidis K, Waldner M, Bernhagen J, Fischle W, Bergmann M, Weber M, Merkle ML, Voelter W, Brunner H, Kapurniotu A (2000) Identification of a penta- and hexapeptide of islet amyloid polypeptide

(IAPP) with amyloidogenic and cytotoxic properties. J Mol Biol 295:1055–1071. doi: 10.1006/jmbi.1999.3422
Tie Y, Calonder C, van Tassel PR (2003) Protein adsorption: Kinetics and history dependence. J Colloid Interface Sci 268:1–11. doi: 10.1016/S0021-9797(03)00516-2
Vendruscolo M, Dobson CM (2005) Towards complete descriptions of the free-energy landscapes of proteins. Philos Trans A Math Phys Eng Sci 363:433-50; discussion 450-2. doi: 10.1098/rsta.2004.1501
Vendruscolo M, Paci E, Karplus M, Dobson CM (2003) Structures and relative free energies of partially folded states of proteins. Proc Natl Acad Sci U S A 100:14817–14821. doi: 10.1073/pnas.2036516100
Vroman L, Adams AL, Klings M (1971) Interactions among human blood proteins at interfaces. Fed Proc 30:1494–1502
Vroman L, Adams AL, Fischer GC, Munoz PC (1980) Interaction of high molecular weight kininogen, factor XII, and fibrinogen in plasma at interfaces. Blood 55:156–159
WARD RV, JENNINGS KH, JEPRAS R, NEVILLE W, OWEN DE, HAWKINS J, CHRISTIE G, DAVIS JB, GEORGE A, KARRAN EH, HOWLETT DR (2000) Fractionation and characterization of oligomeric, protofibrillar and fibrillar forms of β-amyloid peptide. Biochem. J. 348:137. doi: 10.1042/0264-6021:3480137
Watters AL, Deka P, Corrent C, Callender D, Varani G, Sosnick T, Baker D (2007) The highly cooperative folding of small naturally occurring proteins is likely the result of natural selection. Cell 128:613–624. doi: 10.1016/j.cell.2006.12.042
Wertz CF, Santore MM (2001) Effect of Surface Hydrophobicity on Adsorption and Relaxation Kinetics of Albumin and Fibrinogen: Single-Species and Competitive Behavior. Langmuir 17:3006–3016. doi: 10.1021/la0017781
Wertz CF, Santore MM (2002) Adsorption and Reorientation Kinetics of Lysozyme on Hydrophobic Surfaces. Langmuir 18:1190–1199. doi: 10.1021/la0108813
Westermark P, Engström U, Johnson KH, Westermark GT, Betsholtz C (1990) Islet amyloid polypeptide: pinpointing amino acid residues linked to amyloid fibril formation. Proc Natl Acad Sci U S A 87:5036–5040
Westermark P, Benson MD, Buxbaum JN, Cohen AS, Frangione B, Ikeda S-I, Masters CL, Merlini G, Saraiva MJ, Sipe JD (2005) Amyloid: toward terminology clarification. Report from the Nomenclature Committee of the International Society of Amyloidosis. Amyloid 12:1–4. doi: 10.1080/13506120500032196
Westermark P, Andersson A, Westermark GT (2011) Islet amyloid polypeptide, islet amyloid, and diabetes mellitus. Physiol Rev 91:795–826. doi: 10.1152/physrev.00042.2009
Wetzel R (2006) Kinetics and thermodynamics of amyloid fibril assembly. Acc Chem Res 39:671–679. doi: 10.1021/ar050069h
Wiltzius JJW, Sievers SA, Sawaya MR, Cascio D, Popov D, Riekel C, Eisenberg D (2008) Atomic structure of the cross-beta spine of islet amyloid polypeptide (amylin). Protein Sci 17:1467–1474. doi: 10.1110/ps.036509.108
Wolynes P, Onuchic J, Thirumalai D (1995) Navigating the folding routes. Biochemistry 267:1619–1620. doi: 10.1126/science.7886447

Yu Y-P, Zhang S, Liu Q, Li Y-M, Wang C, Besenbacher F, Dong M (2012) 2D amyloid aggregation of human islet amyloid polypeptide at the solid–liquid interface. Soft Matter 8:1616–1622. doi: 10.1039/C1SM06599H

Zhong Q, Inniss D, Kjoller K, Elings VB (1993) Fractured polymer/silica fiber surface studied by tapping mode atomic force microscopy. Surface Science Letters 290:L688-L692. doi: 10.1016/0167-2584(93)90906-Y